

Static and Dynamic Behaviour of Geometrically Imperfect Sandwich Structures using Isogeometric Approach

THESIS

Submitted in partial fulfilment of the requirements for the degree of

DOCTOR OF PHILOSOPHY

By

VASUDEV SINGH SENGAR

ID No. 2019PHXF0046P

Under the Supervision of

Dr. Gaurav Watts



BITS Pilani
Pilani | Dubai | Goa | Hyderabad

**BIRLA INSTITUTE OF TECHNOLOGY AND SCIENCE, PILANI, PILANI CAMPUS
PILANI-333031, RAJASTHAN, INDIA
JULY 2024**

DEDICATION

I am grateful to my supervisor Dr Gaurav Watts, whose unwavering support has been essential in realising a dream I once thought impossible. His guidance and encouragement have been invaluable in my academic and personal growth, and I am forever thankful. Furthermore, I dedicate this work to my late grandfather, Raghunandan Singh, whose absence is keenly felt but whose memory and legacy continue to inspire me.

DECLARATION

I certify that.

1. The work contained in this thesis is original and has been done by me under the guidance of my supervisor.
2. The work has not been submitted to any other institute for any degree or diploma.
3. I have followed the guidelines provided by the institute in preparing the thesis.
4. I have confirmed the norms and guidelines given in the ethical code of conduct of the Institute.
5. Whenever I have quoted written materials from other sources, I have put them under quotation marks and given due credit to the sources by citing them and giving the required details in the references

Vasudev Singh Sengar



Birla Institute of Technology & Science, Pilani
Pilani Campus

CERTIFICATE

This is to certify that the thesis titled "**Static and Dynamic Behaviour of Geometrically Imperfect Sandwich Structures using Isogeometric Approach**", submitted by **Vasudev Singh Sengar** ID No **2019PHXF0046P** for an award of PhD of the Institute, embodies his original work under my supervision.

Signature of the Supervisor _____

Name in capital letters: Dr GAURAV WATTS

Designation: Assistant Professor

Date:

Acknowledgements

The more you read, the more things you will know, the more you learn, and the more places you'll go.

—**Dr Seuss**

This quote has always resonated with me, but as I approach the end of my PhD, its profound meaning has taken on new significance in my life.

I want to express my sincere gratitude to my supervisor, Dr Gaurav Watts. This work would never have been accomplished without his unwavering support and dedicated involvement. Dr Watts is an exceptional academician whose expertise and commitment to supporting early career researchers make him an actual role model in the often competitive realm of academia. His constant support, advice, and encouragement have been invaluable to me. From refining my research proposal to the final submission of my thesis, Dr Watts's wealth of wisdom has been instrumental in shaping my academic growth. Our biweekly meetings were crucial checkpoints that kept me on track and provided plenty of encouragement. I am deeply grateful for Dr Watts's immeasurable contributions to my development and daily life.

I am grateful to my doctoral advisory committee members, Prof. S.N Patel and Dr Rajesh Kumar, Department of Civil Engineering, for enriching my work with valuable feedback and thought-provoking discussions. I am grateful to the Mechanical Engineering Department for providing an educational environment that nurtured my passion for this field. I want to thank the Birla Institute of Technology and Science Pilani for financial assistance during my doctoral research at the Pilani campus.

I want to thank my research colleagues, including Aswanth VU, Mukesh, Rishi, Diplesh, Shekhar, Pradeep, and my dear friend Dhruv, who holds a special place in my heart. Additionally, I extend my heartfelt appreciation to Meghasyam Nynaru and the M.E scholars who provided unwavering support throughout my work, enabling it to take its current form.

I am deeply grateful to my family for their unwavering love, inspiration, support, and encouragement in helping me achieve greater heights. Words fail to convey the extent of my appreciation for their sacrifices, without which completing this research work would not have been possible.

Vasudev Singh Sengar

Abstract

Sandwich structures are commonly used in aerospace vehicles, ship hulls, road vehicles and civil engineering due to their high bending rigidity, low weight, excellent vibration isolation and fatigue properties. The introduction of nanofillers such as carbon nanotubes (CNTs) and graphene platelets (GPL) as reinforcements in facings causes considerable improvement in overall mechanical properties, which has led to an increase in the use of sandwich structures with functionally graded carbon nanotube reinforced composite (FGCNTRC) facings. Accurate analysis of slender members in aerospace structures are crucial to prevent failure due to instabilities under static and dynamic loads. Partial differential equations are used to represent the equilibrium of complex structures under different loading conditions. Numerical methods are employed to solve them, finite element methods (FEM) being the most common for analysing solid mechanics problems. In FEM, the meshing is time-consuming and may introduce errors when analysing structures. Researchers have made significant progress in improving the Finite Element Method (FEM) by developing various modified versions that effectively address its limitations. Isogeometric Analysis (IGA) is one of the modified versions of FEM, which uses non-uniform rational B-splines (NURBS) as basis functions to approximate geometry and unknown field variables. The present work attempts to investigate the effectiveness of IGA in obtaining solutions for linear/non-linear static and dynamic behaviours of initially imperfect sandwich panels under uniform/non-uniform mechanical loads with/without considering the effect of temperature-dependent properties. An in-house MATLAB code is developed to solve the linear and non-linear equilibrium algebraic equations for sandwich plates.

In the beginning, the efficacy of IGA with non-polynomial higher-order theory for stability behaviour of sandwich plates under nonuniform mechanical loads is examined by a series of convergence studies and a comparison of the present numerical results with available analytical or numerical solutions. Thereafter, the buckling, post-buckling, and post-buckled vibration behaviour of initially imperfect skew sandwich plates is investigated. The face sheets are FGCNTRC, and the core layer is made up of aluminium foam. The effects of three types of CNT distributions (UD, FGX and FGO) in the face sheets, two types (uniform, symmetric) of porosity distribution functions for the core layer and five types of in-plane compressive loads are examined. The pre-buckling stresses are calculated using static analysis to evaluate

accurate, critical loads. The post-buckling paths are traced using the modified Riks method. Subsequently, the influence of CNT distribution patterns, porosity functions, compressive loads, skew angle and the side-to-thickness ratio is studied on the non-linear stability and free vibration behaviour of the post-buckled skew sandwich plates.

Next, the stability characteristics of skew sandwich plates with functionally graded facings reinforced with carbon nanotubes having temperature-dependent properties and a re-entrant auxetic core with tunable material properties are presented. The continuous function for material properties of the CNTs is obtained by interpolating the parameters at different temperature values using the fourth-degree polynomial. The resultant properties for the facings are determined using the modified rule of mixtures with the efficiency parameters. The mechanical and thermal properties of the re-entrant auxetic core are based on modified Gibson's relations. The equations of equilibrium are derived using the Hamilton's principle. Several parametric studies are conducted to study the influence of type and magnitude of initial geometric imperfection, CNT distribution pattern in facings, cell angle of the auxetic core, rib length to thickness ratio, skew angle, and boundary conditions on linear and non-linear thermal post-buckling characteristics of the sandwich plate. New findings on the influence of geometric imperfection and auxetic core parameters on the thermal post-buckling behaviour of sandwich plates are presented for the first time, which may contribute towards a better understanding of the stability behaviour of lightweight structures.

Finally, the non-linear vibration response for sandwich plates under thermal loading conditions is studied. Sandwich plates with functionally graded facings reinforced with carbon nanotubes having temperature-dependent properties, and a re-entrant auxetic core with tunable material properties are selected for investigation. The material properties of FGCNTRC face sheets are assumed to be graded in the direction of thickness. A detailed parametric study is conducted on the effects of CNTs volume fraction and distribution pattern, core-to-face sheet thickness ratio, skew angle, side-to-thickness ratio, the effect of cell wall angle and cell wall thickness to rib length ratio and in-plane boundary conditions on the non-linear vibration characteristics of the sandwich plates.

Table of Contents

Dedication	i
Declaration	ii
Certificate	iii
Acknowledgements	v
Abstract	vi
List of Figures	xii
List of Tables	xvi
List of Symbols	xviii
Acronyms	xx
1 Introduction	1
1.1 Introduction.....	1
1.2 The structure of the thesis	4
2 Literature Review	7
2.1 Introduction.....	7
2.2 Overview of Plate Theories.....	7
2.3 History of Isogeometric Analysis (IGA).....	9
2.4 Buckling and Post-buckling Analysis of Plate Subjected to Mechanical Load.....	11
2.5 Buckling and Post-buckling Analysis under Thermal Load	16
2.6 Dynamic Instability Analysis and Non-linear Vibration.....	18
2.7 Summary	21
3 Scope and Objectives	23
3.1 Introduction.....	23
4 Mathematical Formulation	25

4.1	Introduction.....	25
4.2	Isogeometric Analysis (IGA).....	25
4.3	Structural Modelling.....	27
4.3.1	Isotropic Material.....	28
4.3.2	Orthotropic Material.....	28
4.4	Transformed Constitutive Relations.....	28
4.5	Strain-Displacement Relations.....	29
4.6	Influence of Mode of Imperfections.....	32
4.7	Governing Equations.....	36
4.8	Stability Behaviour Under Non Uniform Mechanical Load.....	37
4.9	Stability Behaviour of Plate Under Thermal Environment.....	39
4.10	Non-Linear Vibration.....	41
4.11	Solution Procedure for the Non-Linear Algebraic Equations.....	42
4.11.1	Newton–Raphson Method.....	43
4.11.2	Force Control Method.....	44
4.11.3	Displacement Control Method.....	45
4.11.4	Arc Length Method.....	46
4.12	Mapping Technique in IGA.....	47
4.13	Oblique Boundary Transformation for Skew Plate.....	50
4.14	Boundary Conditions.....	52
4.15	Summary.....	52
5	Stability Analysis of Sandwich Plates Under Non-Uniform Loading	53
5.1	Introduction.....	53
5.2	Geometry and Material Properties.....	53
5.2.1	Boundary Conditions.....	57
5.3	Linear Buckling Analysis.....	57

5.3.1	Isotropic Plates.....	58
5.3.2	Sandwich Plate with Various Support Conditions	60
5.4	Non-linear Post-buckling Analysis	63
5.4.1	Isotropic Plates.....	63
5.4.2	Skew Sandwich Plate.....	65
5.5	Displacement Through Thickness.....	67
5.6	Summary.....	70
6	Stability Analysis of Sandwich Plates in Thermal Environment	71
6.1	Introduction.....	71
6.2	Geometrical and Material Variables of Sandwich Plate	71
6.2.1	Boundary Conditions	76
6.3	Linear Thermal Buckling Analysis	76
6.3.1	Linear Stability Analysis for Isotropic, Laminated, and Sandwich Plate	76
6.4	Thermal Post-Buckling Analysis	84
6.4.1	Validation Study.....	84
6.4.2	Thermal Post-Buckling of Square Sandwich Plate.....	85
6.4.3	Thermal Post-Buckling of Skew Sandwich Plate	88
6.5	Summary.....	92
7	Non-Linear Vibration Analysis of Sandwich Plate in Thermal Environment	95
7.1	Introduction.....	95
7.1.1	Boundary Conditions	95
7.2	Linear Vibration Analysis	97
7.3	Non-Linear Vibration Analysis	104
7.3.1	Non-Linear Vibration Analysis of Isotropic Plate	104
7.3.2	Non-Linear Vibration Analysis of Laminated Composite Plate	105
7.3.3	Non-Linear Vibration Analysis of FGCNTRC Plate	106

7.3.4	Non-Linear Vibration Analysis of Skew Sandwich Plate	109
7.4	Summary	113
8	Conclusions.....	115
8.1	General.....	115
8.2	Performance of the Present Numerical Method.....	115
8.3	Stability Analysis of Plates Under Non-Uniform Mechanical Loadings.....	116
8.4	Stability Behaviour of Plates Under Thermal Loadings	117
8.5	Non-Linear Vibration Analysis of Sandwich Plate	118
8.6	Recommendations for Future Work.....	119
	Appendices	121
	Modified Riks Technique	122
	References	127
	Publications from Present Work	141
	Biography of the Supervisor	143
	Biography of the Author	144

List of Figures

Figure 1.1: Sandwich Structures (a) with honeycomb core (b) with auxetic re-entrant core	1
Figure 1.2: Local buckling in airplane fuselage.....	2
Figure 1.3: Buckling on the ship hull Structure.....	2
Figure 1.4: Engineering structures are becoming increasingly complex and large, resulting in longer manufacturing times and more expensive analysis.	4
Figure 2.1: Illustration of how CPT, FSDT and HSDT differ regarding in-plane displacements.....	8
Figure 2.2: General Concepts Involving Isogeometric Analysis.....	10
Figure 2.3: Bar subjected to axial force and the unstable linear path and stable post-buckling path.....	12
Figure 2.4: Stable post-buckling path.....	12
Figure 2.5: Unstable post-buckling path.....	13
Figure 4.1: Sandwich plate.....	29
Figure 4.2: Description of various modes of initial Imperfections.....	33
Figure 4.3: Flowchart of the non-linear analysis method.....	42
Figure 4.4: Conventional Newton-Raphson Method.....	44
Figure 4.5: Force control method.....	45
Figure 4.6: Displacement Control Method.....	46
Figure 4.7: Arc length method.....	47
Figure 4.8: Mapping technique in isogeometric analysis.....	47
Figure 4.9: The coordinate system and displacement field variables of the skew sandwich plate.....	51
Figure 5.1: Geometrical parameters for the sandwich skew plate.....	56
Figure 5.2: Various types of CNT pattern distributions in the top and bottom face sheets.....	56
Figure 5.3. Types of porosity function through the thickness of the core.....	56
Figure 5.4: Functions for arbitrary compressive loads ($b_1 = b \cos \psi$).....	57
Figure 5.5: Post-buckling behaviour of an initially imperfect SSSS square isotropic plate under uniform compression.....	63
Figure 5.6: Post buckling and free vibration behaviour about the post-buckled configuration of a skew isotropic plate with different values of initial imperfections subjected to uniaxial uniform edge load.....	64

Figure 5.7: Influence of CNT distribution in the facings on post-buckling behaviour of a skew sandwich plate subjected to uniform compression	65
Figure 5.8: Influence of porosity functions in the core of a skew sandwich plate on post-buckling behaviour subjected to uniaxial uniform edge load.	66
Figure 5.9: Influence of edge load distribution on post-buckling behaviour of a skew sandwich plate.....	66
Figure 5.10: influence of skew angle on post-buckling paths and post-buckled vibration behaviour of a skew sandwich plate	67
Figure 5.11: In-plane and Transverse Displacement through-thickness for pre-buckled vibration behaviour about the equilibrium position $\lambda/\lambda_{cr}^* = 0.5$ of a square sandwich plate subjected to uniform compression	68
Figure 5.12: In-plane and Transverse Displacement through-thickness for post-buckled vibration behaviour about the equilibrium position $\lambda/\lambda_{cr}^* = 1.5$ of a square sandwich plate subjected to uniform compression	68
Figure 5.13: In-plane and Transverse Displacement through-thickness for pre-buckled vibration behaviour about the equilibrium position $\lambda/\lambda_{cr}^* = 0.5$ of a square sandwich plate subjected to uniform compression	69
Figure 5.14: In-plane and Transverse Displacement through-thickness for post-buckled vibration behaviour about the equilibrium position $\lambda/\lambda_{cr}^* = 1.5$ of a square sandwich plate subjected to uniform compression	69
Figure 6.1: Shapes and geometrical parameters of the sandwich skew plate	75
Figure 6.2: Different CNT patterns in facings and the re-entrant auxetic core.	75
Figure 6.3: Poisson's ratio Vs. cell angle with various cell aspect ratio	79
Figure 6.4: Critical buckling temperature Vs. Imperfection size μ for isotropic imperfect ceramic plate	80
Figure 6.5: A comparison of thermal post-buckling equilibrium path of CCCC isotropic square plate.	84
Figure 6.6: A comparison of the post-buckling behavior of a $[0/90^\circ]_s$ laminated plates.	84
Figure 6.7: Influence of width-to-plate thickness ratio of a sandwich plate on post-buckling behaviour subjected to uniform temperature rise.....	85
Figure 6.8: Influence of core to a plate thickness of a square sandwich plate on post-buckling behaviour subjected to uniform temperature rise	85

Figure 6.9: Influence of CNT distribution in the face sheets of a square sandwich plate on post-buckling behaviour subjected to uniform temperature rise.....	86
Figure 6.10: Influence of core auxecity on a square sandwich plate consists of isotropic face sheets on post-buckling behaviour subjected to thermal load	86
Figure 6.11: Influence of types of imperfections of a sandwich plate on post-buckling behaviour subjected to uniform temperature rise.....	87
Figure 6.12: Influence of boundary conditions of the skew sandwich plate on post-buckling behaviour subjected to thermal load	87
Figure 6.13: Influence of skew angle on the post-buckling path of a sandwich skew plate under uniform temperature rise	88
Figure 6.14: Influence of sine type and L2 type imperfections on post-buckling paths of a skew sandwich plate	89
Figure 6.15: The effect of CNT distribution in the face sheets of a skew sandwich plate on post-buckling behaviour subjected to uniform temperature rise.....	89
Figure 6.16: Effect of core-to-plate thickness ratio of a skew sandwich plate on post-buckling behaviour subjected to uniform temperature rise	90
Figure 6.17: Influence of width to a plate thickness of a skew sandwich plate on post-buckling behaviour subjected to uniform temperate rise	90
Figure 6.18: Influence of core auxeticity on a skew sandwich plate on post-buckling behaviour subjected to thermal	91
Figure 6.19: Influence of boundary conditions of the skew sandwich plate on post-buckling behaviour subjected to uniform temperature	91
Figure 7.1: Geometrical parameters of the sandwich plate.....	96
Figure 7.2: CNT distribution pattern.....	96
Figure 7.3: A comparison of non-linear to linear frequency ratio of isotropic plate	105
Figure 7.4: A validation study on composite laminated plates'(angle ply) non-linear to linear frequency ratio results in two boundary conditions.....	106
Figure 7.5: A validation study on composite laminated plates'(cross-ply) non-linear to linear frequency ratio results in two boundary conditions.....	106
Figure 7.6: Influence of side-to-thickness ratio on the non-linear frequency parameter of a FGCNTRC plate	107
Figure 7.7: Influence of non-linear frequency parameters on FGCNTRC plates with UD patterns, different CNTs volume fractions and different boundary conditions	107

Figure 7.8: Non-linear frequency parameter in FGCNTRC plates with FGX patterns, different CNT volume fractions and different boundary conditions	108
Figure 7.9: Non-linear frequency parameter in FGCNTRC plates with FGO patterns, different CNT volume fractions and different boundary conditions	108
Figure 7.10: Influence of skew angle on the non-linear to linear frequency ratio of a sandwich plate at room temperature	110
Figure 7.11: Influence of side-to-thickness ratio on the non-linear to linear frequency ratio of a skew sandwich plate at room temperature	110
Figure 7.12: Influence of side-to-thickness ratio on the non-linear to linear frequency ratio of a skew sandwich plate at room temperature	111
Figure 7.13: The effect of CNT distribution in the face sheets of a skew sandwich plate on non-linear to linear frequency ratio at room temperature	111
Figure 7.14: Influence of core auxeticity on a skew sandwich plate on non-linear to linear frequency ratio at room temperature	112
Figure 7.15: Influence of boundary conditions of the skew sandwich plate on non-linear to linear frequency ratio at room temperature.....	112

List of Tables

Table 4.1: Gauss points and weights in the Gauss-Legendre numerical integration	50
Table 5.1: Material properties for the various cases considered in the present study.	54
Table 5.2: Volume fraction function of CNTs for different distributions.....	54
Table 5.3: Efficiency parameters for the FGCNTRC	55
Table 5.4: Porosity distribution functions	55
Table 5.5: Convergence study of linear buckling load parameters for SSSS thin ($a/h = 1000$) isotropic skew plate subjected to uniform compression	58
Table 5.6: Linear buckling loads for single-layered porous aluminium skew plate subjected to uniform edge loads.....	59
Table 5.7: Linear buckling loads for FGCNTRC plate subjected to uniaxial edge loads.....	60
Table 5.8: Effect of edge compression on non-dimensional critical load parameter for the sandwich skew plate	61
Table 5.9: Effect of CNT distribution in facings on linear buckling loads for sandwich skew plate subjected to uniform compression	62
Table 5.10: Effect of porosity functions in the core on linear buckling loads for the sandwich skew plate under uniform compression $P_{cra2Ech3}$, $V_{CN} = 0.17$, UD, $ah = 100$	62
Table 6.1: P_i coefficients for various thermomechanical characteristics associated with fourth-order interpolation.....	73
Table 6.2: CNTs' volume fraction function for various distributions.....	73
Table 6.3: FGCNTRC efficiency parameters	73
Table 6.4: Convergence of critical buckling temperature parameter (T_{cr}) for simply supported (SSSS) FGCNTRC plates established on a temperature-dependent analysis. ($a/b = 1$).....	77
Table 6.5: Thermal buckling parameter $\lambda_{cr} = 100\alpha_{22}\Delta T_{cr}$ of $[0/90^\circ]_s$ laminated skew plates with numerous skew angles and BC.	78
Table 6.6: Non-dimensional frequency parameters of the auxetic core sandwich plate for various θ_{hc} and h_2/h	79
Table 6.7: Critical temperature ΔT_{cr} of the isotropic imperfect ceramic plate for different imperfection modes under uniform temperature rise	81
Table 6.8: Critical buckling temperature $(\Delta T)_{cr}$ of the simply supported square sandwich plate with auxetic core for two different imperfection modes under a uniform temperature rise	81

Table 6.9: Critical temperature (ΔT_{cr}) of the skew sandwich plate for two imperfection modes under a uniform temperature rise	82
Table 6.10: The effect of CNT distribution pattern in facings on critical temperature parameter (ΔT_{cr}) for the skew sandwich plate for uniform temperature rise	82
Table 6.11: Influence of cell angle and skew angle on critical temperature parameter for uniform temperature rise.....	83
Table 6.12: Influence of type of core to plate thickness on critical temperature parameter for skew sandwich plate	83
Table 7.1: Temperature-dependent material properties for SWCNT.....	96
Table 7.2: Convergence study of the influence of width-to-thickness ratio and CNT volume fraction on the non-dimensional natural frequency parameter for simply supported FGCNTRC square plates.	97
Table 7.3: First six non-dimensional natural frequency parameters of simply supported functionally graded reinforced composite plates with CNT volume fraction.....	98
Table 7.4: First six dimensionless natural frequency parameters of simply supported functionally graded reinforced composite plates with CNT volume fraction.....	99
Table 7.5: First six dimensionless natural frequency parameters of simply supported functionally graded reinforced composite plates with CNT volume fraction.....	100
Table 7.6: Non-dimensional natural frequency parameter for simply supported various types of FGCNTRC plates in different temperature environments.....	100
Table 7.7: Comparison of the non-dimensional natural frequency parameter for sandwich plates with CNT-reinforced face sheets in a thermal environment with various core-to-face sheet thicknesses and CNT volume fractions. The CNTs are assumed to be functionally graded, i.e., FGX.....	101
Table 7.8: Influence of type of CNT distribution in face sheets on non-dimensional natural frequency parameter for the sandwich plate at room temperature.....	102
Table 7.9: Influence of cell angle and skew angle on non-dimensional natural frequency parameter for a sandwich plate at room temperature.	103
Table 7.10: Influence of thickness of core to face sheets thickness on non-dimensional natural frequency parameter	104

List of Symbols

Greek symbols

α	The coefficient of thermal expansion
ψ	Skew angle
θ_{hc}	Inclined cell angle
θ_x	Rotation of mid-plane about y-axis
θ_y	Rotation of mid-plane about x -axis
ξ, η	Parametric coordinates
Γ_P	Surface Area of the Structure
Δ	Geometric imperfection
μ	Amplitude of imperfection
ν	Poisson's ratio
ρ	Mass density
Ξ	Set of knot vectors
ω	Natural frequency
ε	In-plane strain field
ε_L	Linear strain field
ε_{NL}	Non-linear strain field
ε_γ	Shear strain vector
σ	Stress field in the structure

Other Symbols

B	Strain matrix
F	Force vector
J	Jacobian matrix
K	Global stiffness matrix
K_G	Geometric stiffness matrix

\mathbf{K}_0	Initial stiffness matrix
\mathbf{K}_L	Linear stiffness matrix
\mathbf{K}_{NL}	Non-linear stiffness matrix
\mathbf{K}_T	Tangent stiffness matrix
\mathbf{M}	Global mass matrix
P	Control point coordinate
q	unknown variable vector
E	Young modulus of the structure
G	Shear modulus of the structure
h	Thickness of the structure
k	Thermal conductivity
n	Number of control points
p, q	Order of basis function
t	Time
T	Temperature
u_0	In-plane displacement of a point at midplane in x direction
v_0	In-plane displacement of a point at midplane in y direction
w_0	Transverse displacement of a point at midplane
N_i	B-spline basis function
φ_i	NURBS basis function
x,y,z	Orthogonal coordinate system of the structure

Acronyms

CAD	Computer-aided design
CCCC	Fully clamped support
CNT	Carbon nanotube
CPT	Classical plate theories
DOF	Degree of freedom
DQM	Differential quadrature method
ELS	Equivalent single layer
FEA	Finite element analysis
FEM	Finite element method
FG	Functionally graded
FGM	Functionally graded material
FGP	Functionally graded plate
FGCNTRC	Functionally graded carbon nanotube reinforced composite
FSDT	First-order shear deformation theory
FSM	Finite strip method
GSDT	Generalised shear deformation theory
HSDT	Higher-order shear deformation theory
IGA	Isogeometric analysis
LWT	Layer wise theory
NPR	Negative poisons ratio
NURBS	Non-uniform rational B-splines
PMMA	Poly methyl methacrylate
PmPV	Poly meta phenylene vinylene
SSSS	Fully simply support
SSL	Sinusoidal Load
UDL	Uniform distributed load

Chapter 1

1.1 Introduction

The introduction of sandwich plate structures [Figure 1.1](#) has been a remarkable development in the field of structural engineering, aerospace engineering, and marine engineering. These innovative configurations, which feature a core material sandwiched between two faceplates, offer a balance of strength and weight efficiency that has proven vital in modern engineering applications. To effectively utilise sandwich plates, it is imperative to have a comprehensive understanding of their deformable characteristics, stress distribution, natural frequencies, dynamic behaviour, and instability under thermal and mechanical loads.

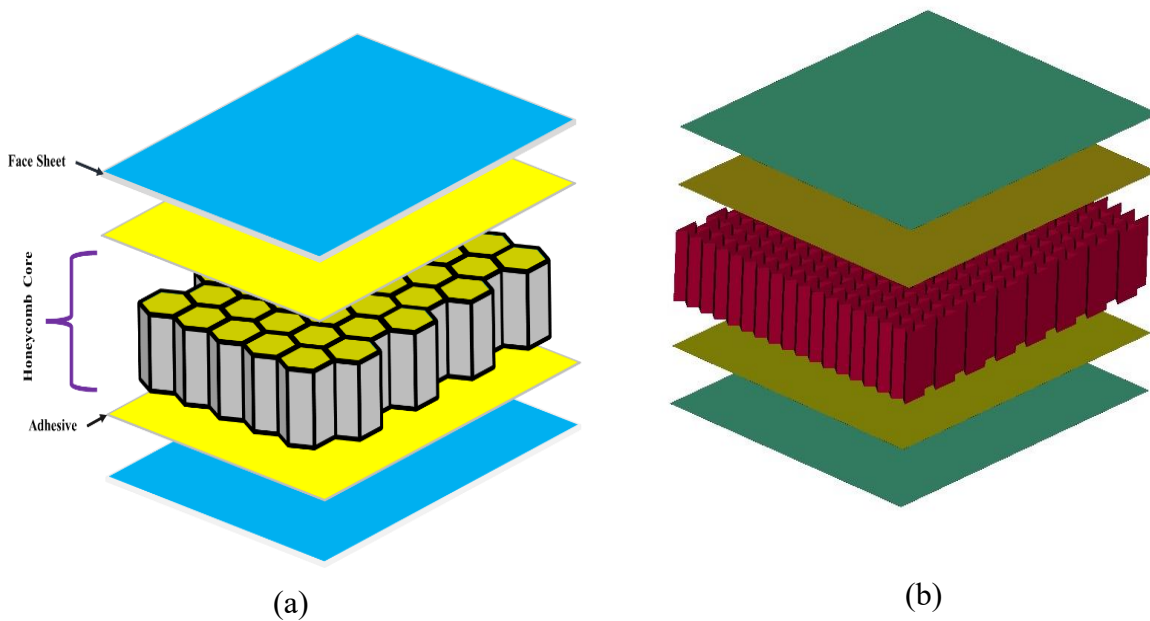


Figure 1.1: Sandwich Structures (a) with honeycomb core (b) with auxetic re-entrant core

The failure mode of sandwich structures can be classified into two categories: static failure, which includes bending and buckling, and dynamic failure, which includes vibration and dynamic instability. [Figure 1.2](#) illustrates the buckling of the aeroplane fuselage caused by excessive compression loading. [Figure 1.3](#) shows an example of buckling due to wave impact loads in an aluminium ship structure.

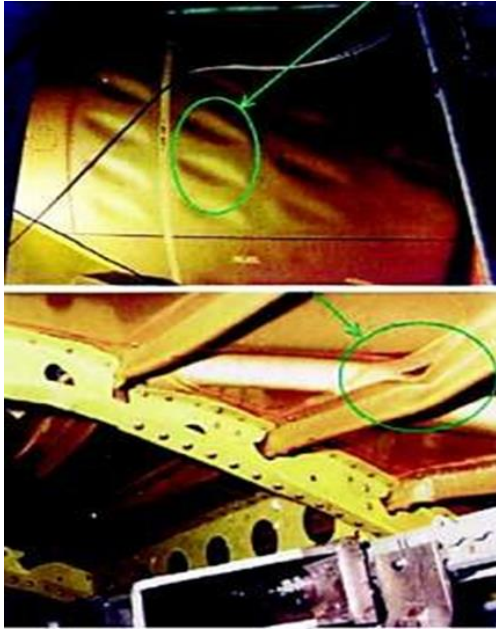


Figure 1.2: Local buckling in airplane fuselage (Imran et al., 2018)



Figure 1.3: Buckling on the ship hull Structure (Lavroff et al., 2013)

By making small displacement and strain assumptions, the plate formulation can be simplified into a linear problem that can be easily solved with low computational cost. However, it is important to note that linear solutions may deviate from the actual responses of structures. In some cases, nonlinearity is the only viable option for an analyst, such as when dealing with post-buckling phenomena. Since the safety of such structures is of paramount concern, non-linear analysis must be considered. It is evident from the literature that the stability analyses and non-linear behaviour of plates and the related approximation/discretisation technique of the non-linear governing equations for the general problem domain are the subject of ongoing research. Thus, this thesis investigates the linear and non-linear behaviour of sandwich structures to investigate plate behaviour in the large deformation regime thoroughly. This study addresses some of the less explored problems concerning sandwich plates, specifically in non-uniform mechanical loading and response of structures in a thermal environment.

The design and analysis of plates and shells under static and dynamic loads are critical in the structure's overall design. The static/dynamic equilibrium of complicated structures under general loading conditions is mathematically represented using complex partial differential equations. Closed-form solutions of higher-order partial differential equations are available only for specific loading and boundary conditions cases. Numerical methods offer an alternative approach by transforming these equations into algebraic ones that can be solved

easily with the help of computers. The finite element method (FEM) is the most commonly used approach, and there are numerous commercial software options available, including ANSYS, ABAQUS, COMSOL, and LS DYNA. When it comes to computer-aided design for engineering structures, non-uniform rational B-spline (NURBS) curves are currently used for geometric modelling, while FEM is used for analysis. However, frequent changes in the structure's design necessitate regular remeshing of the model, which can take up a significant amount of time and computational resources. A recent study by Ted Blacker, manager of simulation sciences at Sandia National Laboratories, focused on time consumption during modelling and analysis. The results showed that a significant portion - approximately 80% - of the simulation time is spent on creating suitable geometry, input data, and meshes for conducting large-scale finite element analysis. As illustrated in [Figure 1.4](#), automobiles comprise roughly 3,000 parts alone, while the Boeing 777 boasts over 100,000 parts, and nuclear-powered, ballistic missile-carrying submarines feature more than 1,000,000 parts ([Bazilevs et al., 2010](#)). Engineering design and analysis are deeply interconnected, and complex designs require expertise in various fields, including structural mechanics, fluid mechanics, acoustics, heat transfer, electromagnetics, and more. Establishing a strong integration between modelling and analysis procedures is essential to address this issue. To address these problems, [Hughes et al. \(2005\)](#) proposed a method called isogeometric analysis (IGA), which attempts to bridge the gap between the original CAD geometry and the FEM mesh. It is a computational technique whose main objective is to create one model by integrating finite element analysis (FEA) into computer-aided design (CAD). In FEM, Lagrange interpolation functions are used for geometry and solution approximation. As the name suggests, the functions are interpolating and will pass through all the nodes during geometry approximation, but in IGA, the non-uniform rational B-splines (NURBS) basis functions are used to approximate both the geometry and unknown variables of the problem.

The classical plate theory, which requires C^1 -continuity elements, often yields satisfactory results for thin plates. However, the first-order shear deformation (FSDT) theory is more appropriate for moderately thick plates. Unfortunately, standard FSDT-based finite elements can become overly rigid, leading to shear locking during thin plate analysis. Additionally, the results rely heavily on the shear correction factor, which is problematic across multiple problems. This thesis uses a non-polynomial higher-order theory incorporating higher-order terms in the displacement field to describe the shear energy component more accurately without needing a shear correction factor. This study aims to investigate the effectiveness of

isogeometric analysis using non-polynomial higher-order theory to analyse sandwich plates' linear and non-linear behaviour.

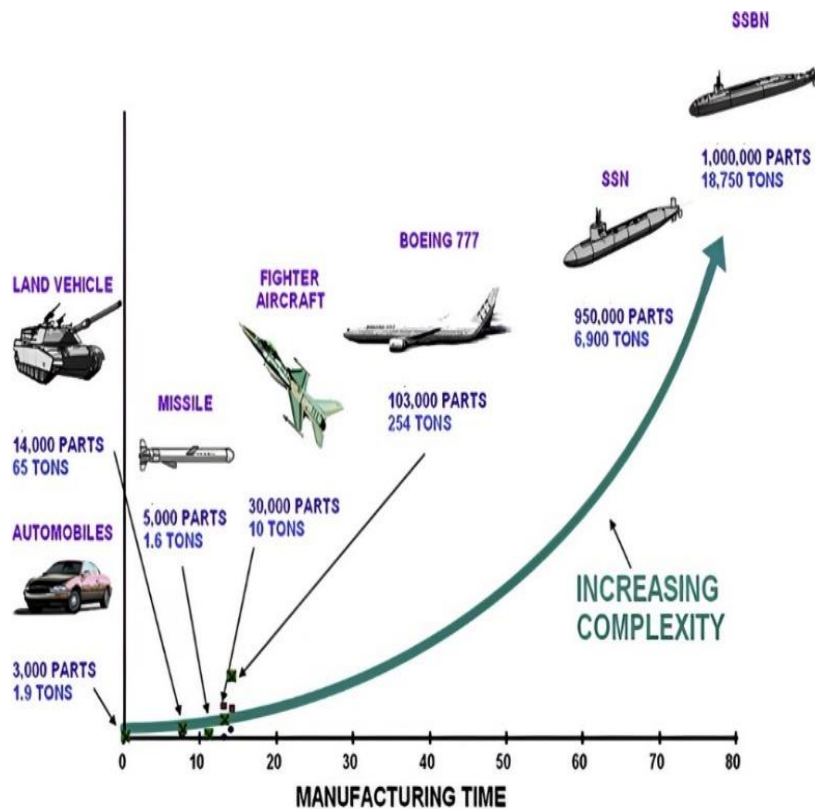


Figure 1.4: Engineering structures are becoming increasingly complex and large, resulting in longer manufacturing times and more expensive analysis. (Bazilevs et al., 2010)

1.2 The Structure of the Thesis

This thesis consists of eight chapters that examine the structural behaviour of sandwich plates. The first chapter introduces the research problem and emphasises on its importance. The second chapter presents a detailed review of existing literature on the subject, which helps outline the investigation's scope in the third chapter. The fourth chapter documents the mathematical formulation of the isogeometric analysis approach, which employs non-polynomial higher-order theory to describe the field variables of the plates. Chapter five focuses on the solution strategies for various problems of sandwich plates, including buckling, post-buckling, and post-buckled vibration behaviour of initial imperfect sandwich plates under non-uniform mechanical loadings. In chapter six, the buckling and post-buckling behaviours of initially imperfect sandwich plates in a thermal environment are examined. Chapter seven investigates the non-linear vibration behaviour of sandwich plates. Finally, chapter eight

summarises the important conclusions of the study and mentions the scope for future research on the problems considered. The thesis also includes references and archival publications from the present work.

Chapter 2

Literature Review

2.1 Introduction

This chapter comprehensively reviews isogeometric analysis development and its applications in buckling, post-buckling, post-buckled vibration behaviours, and non-linear vibration behaviours of plates in different loading conditions. As discussed in Chapter 1, the accuracy of numerical solutions depends on the selection of the discretization technique or approximation scheme. While the finite element method may have limitations, this thesis explores the isogeometric analysis (IGA) as an alternative approach. Section 2.2 presents an overview of various plate theories. Section 2.3 briefly overviews the IGA method, including its developments and applications, and reviews the published works on using isogeometric analysis in various fields. The previous research on the linear buckling and non-linear post-buckling phenomenon of sandwich plates under mechanical loading is discussed in Section 2.4. Furthermore, Section 2.5 presents the plate's thermal buckling and post-buckling behaviour under a thermal environment. The review of dynamic instability and non-linear vibration behaviours of sandwich plates is covered in Section 2.6. Finally, in Section 2.7, a summary of the critical review of existing literature and the corresponding research gap is provided to conclude this chapter.

2.2 Overview of Plate Theories

As technology advances, many industries - such as aerospace, civil engineering, and automotive - are exploring composite and functionally graded materials. Plates play an important role in the construction of structures, and it's essential to understand their structural behaviour - including bending, displacements, stress formation, and buckling - before incorporating them into the structure. Various plate theories have been proposed to describe these behaviours, as shown in [Figure 2.1](#). [Love and Kirchoff \(1888\)](#) presented the first theory of plates based on displacement assumptions. Based on the assumption in this theory, transverse shear deformation is not considered. Due to this, it gives reliable results only in the case of thin plates, and it does not provide accurate results in the case of moderately thick plates. Shear deformation plate theories have been developed for transverse shear strains. In

order to avoid the inaccuracy of classical plate theory, [Reissner-Mindlin \(1945&1951\)](#) presents a new theory, also known as first-order shear deformation theory, taking the shear effect into account.

However, due to the assumption, i.e. linear in-plane displacement, the shear stress, given by this theory, is inaccurate. For accurate results, the shear correction factor is required. However, it is very tedious to calculate the shear correction factor for every problem. Various higher-order shear deformation theories were given to overcome these issues, including proper distribution of shear stress, higher-order shear deformation theory, third-order shear deformation theory ([Reddy, 1984](#)) and fifth-order shear deformation theory (FiSDT). All theories use a single-layer model, which has the same degree of freedom of all the layers. The problem arises because the core and face sheet strength is very high due to these bending behaviours, and the dynamic response is inaccurate ([Reddy, 1987](#)). For more accuracy, a new concept is proposed, i.e. layer-wise theory. The layer-wise idea is the most popular among all the layer-wise theory theories. The above-emphasised shows that the CPT, FSDT, HSDT, and layer-wise approaches described are 2D models. The multi-layered plates can also use the 3D model based on an elastic 3D continuum. However, the practical application of the 3D model is limited due to the increased number of unknowns of the problem.

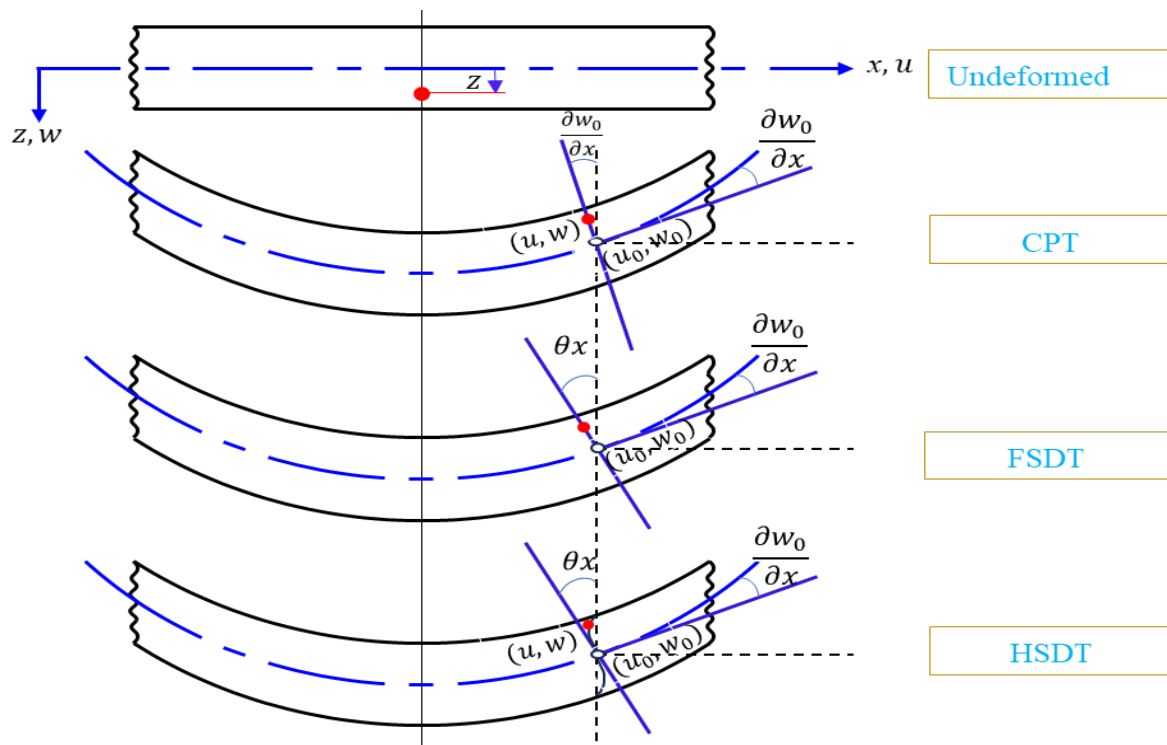


Figure 2.1: Illustration of how CPT, FSDT and HSDT differ regarding in-plane displacements [Wang et al.\(2000\)](#)

Various authors reviewed the plate theories and presented conclusions. For example, [Reddy & Bobbins \(1994\)](#) reviewed theories and computational models for the laminated composite plate. [Liu & Li \(1996\)](#) developed an overall view of laminate theories based on the displacement hypothesis. A review of shear deformation plate and shell theories was presented by [Reddy & Arciniega \(2004\)](#). [Aydogdu \(2006\)](#) compared various higher-order shear deformation theories (HSDTs) with available three-dimensional analysis. The researchers found that the exponential shear deformation theory provides the most accurate predictions for transverse displacement and stresses. However, the parabolic and hyperbolic shear deformation theories yield more precise predictions for natural frequencies and buckling loads. [Zhang & Yang \(2009\)](#) comprehensively analysed the finite element models constructed using different laminated plate theories. [Kreja \(2011\)](#) provided a detailed analysis and summary of the existing computational models that are used for laminated composite and sandwich panels in the literature review.

2.3 History of Isogeometric Analysis (IGA)

Partial differential equations are a mathematical representation of the static and dynamic balance of complex structures under various loading conditions. However, closed-form solutions for higher-order equations are only available for specific boundary conditions and load cases. The advent of computer technology has made the process of engineering analysis and design much more straightforward. Numerical methods such as the finite element method (FEM), finite difference method, meshless method, and differential quadrature method are utilised for the approximate solution of partial differential equations. FEM is the most commonly used technique for solid mechanics problems and was developed in 1950 for aerospace engineering. By the late 1960s, commercial computer programs like ASKA, NASTRAN, and Stardyne were available for analysis. Today, most industries related to automotive, aerospace, shipbuilding, and architectural design use computer-aided design (CAD) software for engineering design. The B-spline modelling technique, introduced by [R. Reisenfeld](#) in his doctoral thesis, has also significantly contributed to computer-aided design. ([Reisenfeld, 1975](#)). He produced line basis functions using recursive formulas, which were separately developed by [Cox \(1972\)](#) and [De Boor \(1972\)](#). Non-uniform Rational B-splines (NURBS) is a mathematical technique for creating curves and surfaces with exceptional precision and flexibility. With NURBS, it is possible to accurately represent an array of basic shapes, including cylinders, conical sections, and circles, among many others. Moreover, this

technique can accurately model complex shapes while providing straightforward continuity control. The non-uniform rational B-spline (NURBS) system has two elements - the patch and the knot span. A patch is a subdomain created by knot vectors and is referred to as the parametric space. Patch used as a single model unless encounter geometric complexities that require local meshing. Each patch has two spaces to express its geometry - the physical space and the parent space, which is helpful for numerical evaluation. The knot span is the decomposition of the patch and is defined by the intervals of knots. Knots are points, lines, and surfaces in one-, two-, and three-dimensional topology, respectively. In order to generate meshes for two or three-dimensional models, NURBS surfaces or volumes are utilised. These surfaces are defined by a control polygon with constituent points P_i , which is crucial in deducing and visualising the surface within a physical space. As Figure 2.2 demonstrates this changes from the parameter space governed by parameters ξ and η .

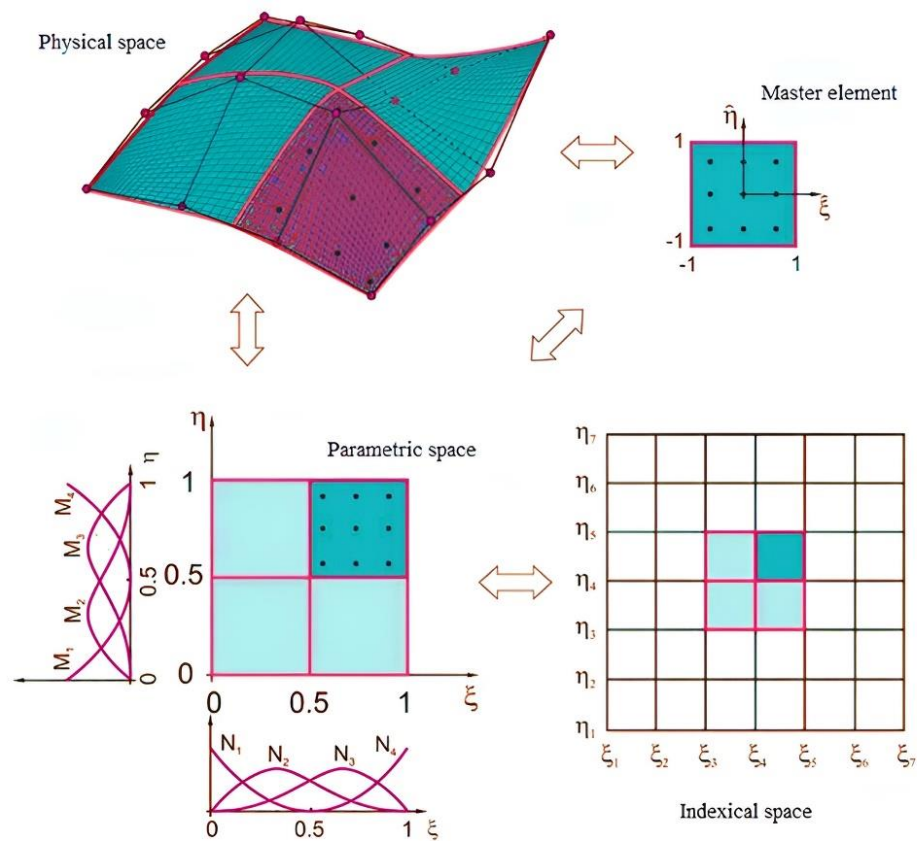


Figure 2.2: General Concepts Involving Isogeometric Analysis (Ćojbašić et al., 2023)

IGA is gaining popularity for accurately representing and analysing complex geometries. Here are some examples of isogeometric analysis applications in structural analysis. Cottrell et al. (2006) provided an overview of isogeometric analysis for structural vibrations, including solving vibration models for rods, beams, plates, and 3D solids. Various researchers solved the

fluid mechanics and solid-fluid interaction problems using Isogeometric analysis. [Akkerman et al. \(2011\)](#) presented an isogeometric analysis of free-surface flow for the first time. [Nielsen et al. \(2011\)](#) presented an isogeometric analysis of the 2-dimensional, steady state, incompressible Navier–Stokes flow subjected to Dirichlet boundary conditions with a detailed description of the numerical method used to solve the boundary value problem. [Bazilevs et al. \(2012\)](#) developed a framework for fluid–structure interaction (FSI) modelling and simulation with an emphasis on isogeometric analysis (IGA) and non-matching fluid–structure interface discretisations. In 2017, C. Wang and colleagues ([Wang et al., 2017](#)) conducted a comprehensive fluid-structure interaction (FSI) analysis in a full-scale hydraulic arresting gear. Recently, [Bazilevs et al. \(2023\)](#) proposed the effective use of isogeometric analysis in computational aerodynamics. Some researchers solved optimisation problems using isogeometric analysis. [Wall et al. \(2008\)](#) presented a structural shape optimisation framework based on isogeometric analysis. [Hassani et al. \(2011\)](#) utilised the isogeometric analysis method in the three-dimensional shape optimisation of structures as an alternative to finite elements. [Dedè et al. \(2012\)](#) employed isogeometric analysis in topology optimisation.

Few researchers have worked on non-linear contact analysis problems using isogeometric analysis. [Gutiérrez et al. \(2020\)](#) presented the utilisation of isogeometric analysis and the boundary integral element method for solving non-linear contact problems.

2.4 Buckling and Post-buckling Analysis of Plate Subjected to Mechanical Load

When an elastic structure is under quasi-static external load, mechanical or thermal, it deforms proportionally until the load reaches a limiting value where it behaves nonproportional and becomes unstable. This condition is known as buckling ([Eslami, 2018](#)).

There are three types of buckling and instability that a structure may experience. The first one is classical buckling or bifurcation buckling, which has been studied the most. In this type of instability, a linear elastic structure follows the primary deformation path before buckling. The deformation is linear up to the bifurcation point, where the loading path splits into the unstable and stable post-buckling paths as shown in [Figure 2.3](#).

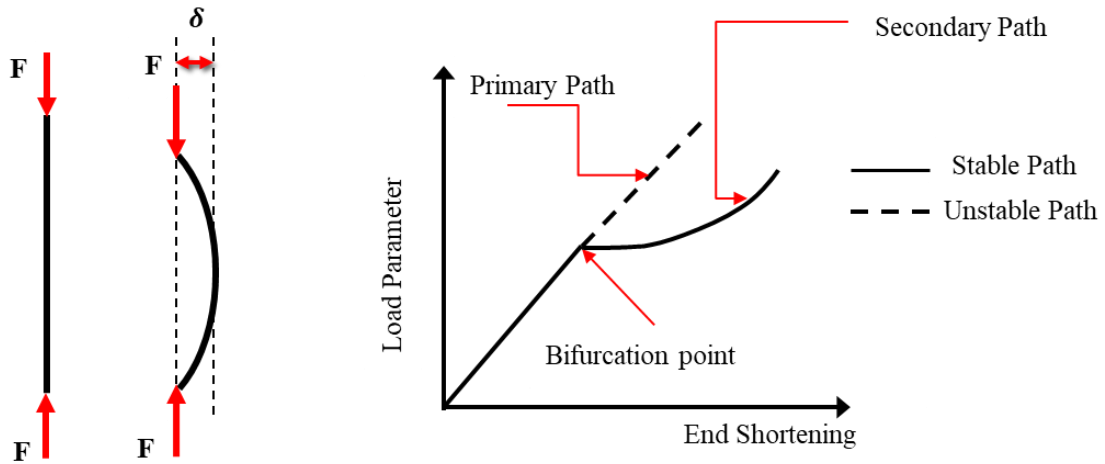


Figure 2.3: Bar subjected to axial force and the unstable linear path and stable post-buckling path (Eslami, 2018).

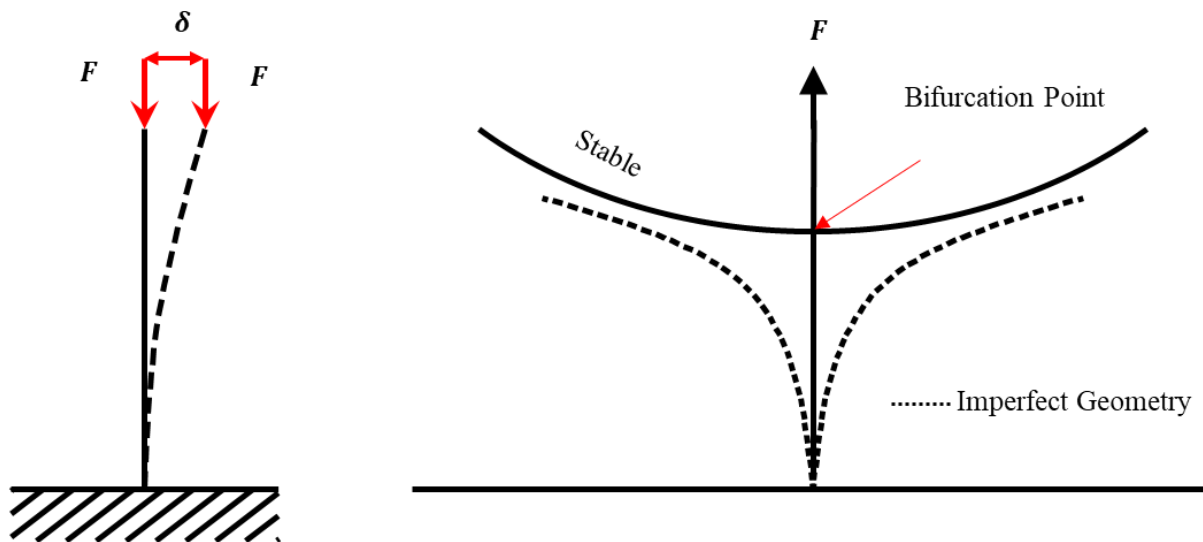


Figure 2.4: Stable post-buckling path (Eslami, 2018)

The second type of instability is finite disturbance buckling, as shown in Figure 2.4. It occurs when a point reaches the bifurcation point and experiences a sharp drop in the applied load before reaching a stable post-buckling path. This type of instability is common in shells. The structure shows an elastic response after the bifurcation point, and the loss of stability is so significant that it requires returning to an earlier loading level to maintain stability.

The third type of instability is snap-through buckling, as shown in Figure 2.5. This type of instability is characterised by a sudden jump from one equilibrium path to another, where the displacements are more significant than the first non-adjacent equilibrium state. Snap-through is a dynamic phenomenon because the static equilibrium path is interrupted by an unstable region. The system must dynamically jump past the unstable region and onto a stable region

capable of bearing loads above the snap-through load as the load increases. Unlike column buckling, there is no stable branch the system can continuously follow along the equilibrium path.

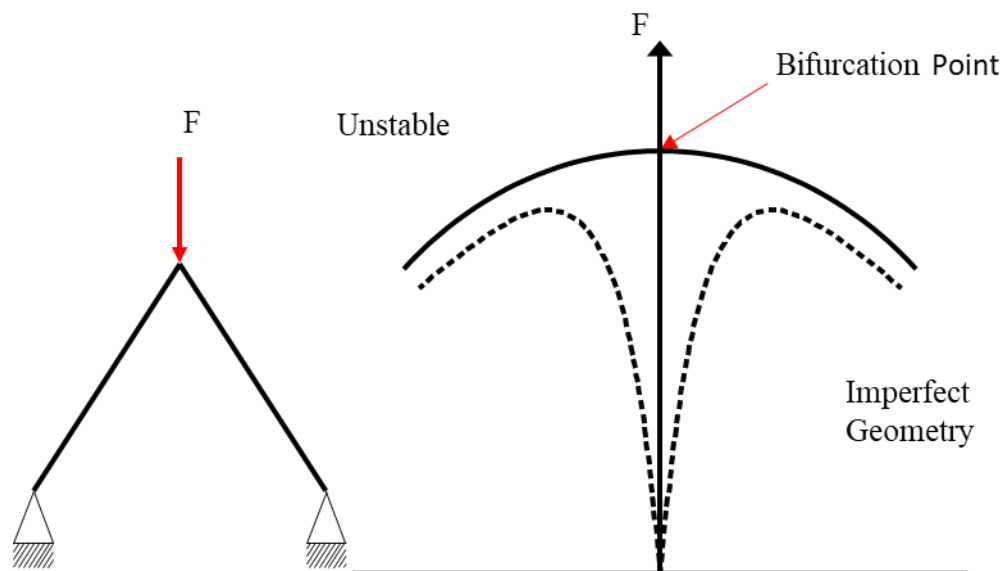


Figure 2.5: Unstable post-buckling path (Eslami, 2018)

Durvasula (1970) carried out the buckling analysis of the isotropic skew plate using the Galerkin method under the influence of mechanical load. Brunelle (1971) worked on the transversely isotropic Mindlin plate under initial stress and displacement. Sherbourne & Pandey (1991) presented solutions for uniaxial buckling of the isotropic plate using the differential quadrature method (DQM). In their 2003 study, X. Wang and colleagues Wang et al. (2003) employed the differential quadrature method (DQM) to investigate the buckling loads of thin anisotropic rectangular plates as well as isotropic skew plates. The study's findings offer a valuable contribution to understanding the buckling behaviour of these types of plates under various loading conditions. Using the DQM, the authors could accurately predict the buckling loads of these plates, which is crucial information for designing structures that can withstand buckling. Eisenberger & Alexandrov (2003) calculated accurate solutions for bifurcation buckling loads of isotropic plates with thickness that varies in the directions parallel to the two sides. The plates are subjected to biaxial compression. Wu et al. (2010) proposed a

mesh-free least squares-based finite difference (LSFD) method for solving free vibration and buckling analysis of highly skewed plates. [Ferreira et al. \(2011\)](#) used Reddy's third-order shear deformation theory and collocation method with radial basis functions to predict elastic plate buckling loads. [Bourada et al. \(2016\)](#) studied a buckling analysis of isotropic and orthotropic plates using a new four-variable refined plate theory subjected to axial load. [Moslemi et al. \(2017\)](#) presented an analytical solution for the buckling of thick rectangular transversely isotropic plates subjected to in-plane loads. [Wang & Yuan \(2018\)](#) introduced a buckling analysis of skew plates under axial loadings using the modified differential quadrature method (DQM). [Ullah et al. \(2019\)](#) utilised a finite integral transform method to obtain an analytical solution for buckling of the thin rectangular plate problem.

The use of composite materials is necessary due to the limitations of isotropic plates. As composite materials are artificial materials, properties can be adjusted accordingly. [Ungbhakorn & Singhatanadgid \(2006\)](#) employed an extended Kantorovich method to investigate the buckling of rectangular laminated composite plates with various edge supports. [Komur et al. \(2010\)](#) studied a buckling analysis of a woven-glass-polyester laminated composite plate with a circular/elliptical hole using the finite element method (FEM). [Arani et al. \(2011\)](#) presented the buckling analysis of laminated composite plates reinforced by single-walled carbon nanotubes (SWCNTs). The analytical approach, in combination with the finite element method, is used to perform the analysis. [Rouhi & Ansari \(2012\)](#) applied finite element analysis to create an atomistic model to study the buckling and vibration properties of single-layered graphene sheets. [Naderi & Saidi \(2013\)](#) have presented an approach to accurately obtain critical buckling stress for thick orthotropic plates by considering the pre-buckling deformations that have not been considered in the previously published literature. [Upadhyay & Shukla \(2013\)](#) investigated the buckling and post-buckling behaviour of laminated composite and sandwich skew plates. In the problem formulation, higher-order shear deformation theory and von-Karman's non-linearity are considered in the problem formulation. [Malekzadeh & Shojaee \(2013\)](#) examined quadrilateral laminated composites' buckling behaviour reinforced with CNTs for uniform and functionally graded distributions. They also derived an analytical solution for the composite with FG symmetric distribution subjected to simply supported boundary conditions, with higher-order shear deformation theory and a meshless technique. [Lei et al. \(2013\)](#) presented the buckling analysis of functionally graded carbon nanotube-reinforced composite (FGCNTRC) plates under various in-plane mechanical loads using the element-free kp-Ritz method. [Asadi \(2014\)](#) studied the buckling analysis of annular composite plates reinforced by carbon nanotubes (CNTs) subjected to compressive and

torsional loads. [Adim et al. \(2016\)](#) used a refined higher-order exponential shear deformation theory to examine the buckling analysis of anti-symmetric cross-ply laminated composite plates under different boundary conditions. [Singh & Singh \(2016\)](#) analysed the buckling of composite plates subjected to uniaxial loading. [Yu et al. \(2016\)](#) investigated free, forced vibration, and buckling analysis of laminated composite plates with complicated cutouts using IGA-based first-order shear deformation theory. [Zhang et al. \(2017\)](#) utilised IGA and Reddy's HSDT to study the influence of CNT orientation on the buckling behaviour of CNTRC skew plates. [Thang et al. \(2017\)](#) presented an analytical approach to analyse the buckling of imperfect FGCNTRC plates subjected to axial compression. In a study conducted by Zghal and colleagues (2018) ([Zghal et al., 2018](#)), the mechanical buckling behaviour of composite plates and curved panels reinforced with carbon nanotubes and functionally graded materials was examined. A double director's finite element shell model was utilized to establish the governing equations, resulting in a high-order displacement field distribution and accounting for the impact of transverse shear deformations. [Geng et al. \(2021\)](#) carried out the buckling analysis of functionally graded graphene platelets-reinforced composite (GPL-RC) rectangular plates with a circular hole using the finite-element (FE) method. [Jahanpour \(2023\)](#) studied the buckling of functionally graded (FG) plates under in-plane compressive loadings. Various researchers worked on the plates' linear buckling and post-buckling behaviour, which is described below. This section analyses the plate's post-buckling and post-buckled vibration behaviour.

The buckling and post-buckling behaviours of thick functionally graded plates resting on elastic foundations were investigated by [Duc & Van Tung \(2011\)](#) and subjected to in-plane compressive, thermal, and thermomechanical loads using higher-order shear deformation theory. [Ovesy et al. \(2012\)](#) employed higher-order shear deformation theory to examine the post-buckling analysis of composite plates with embedded delamination's of any shape. The formulation relies on the Rayleigh-Ritz approximation technique. They applied higher-order shear deformation theory and Green-Lagrange non-linear strain-displacement relationships. [Dash & Singh \(2012\)](#) carried out laminated composite plates' buckling and post-buckling behaviour. [Le-Manh & Lee \(2014\)](#) explored the post-buckling behaviour of laminated composite plates using NURBS-based isogeometric analysis (IGA). They used a green strain tensor with minor rotations. The proposed strain tensor and the von Karman strain tensor are both formulated. Governing equations are derived from the first-order shear deformation theory (FSDT) framework. [Praciano et al. \(2019\)](#) used the isogeometric approach to carry out buckling and post-buckling analyses of laminated plates and shells. They studied the effects of various

factors on critical load and post-buckled behaviour. [Yang et al. \(2020\)](#) applied the IGA and Finite Cell Method (FCM) to the post-buckling behaviour of multi-directional perforated FGM plates.

Since metal foam-based sandwich structures can be manufactured without adhesive bonding, they are being used in automotive and aerospace applications ([Betts, 2012](#)). *There are limited investigations on the flexural behaviour of sandwich structures with metal foam cores.* [Magnucka-Blandzi & Magnucki \(2007\)](#) investigated the elastic buckling behaviour of a sandwich beam with a metal foam core. [Styles et al. \(2007\)](#) explored the effect of core thickness on the deformation mechanism of a sandwich structure with an aluminium foam core and a thermoplastic composite facing. *Furthermore, the literature on the non-linear stability behaviour of non-rectangular sandwich plates with nanocomposite facings and porous and auxetic cores is scarce.*

2.5 Buckling and Post-buckling Analysis under Thermal Load

Conducting a thermal buckling analysis is crucial to structural engineering and design. Thermal buckling and post-buckling are critical in aerospace, civil engineering, and mechanical engineering, as they involve examining how structures handle thermal loads and assessing the likelihood of buckling or failure occurring in such conditions. This section presented a literature review on the buckling and post-buckling of plates in a thermal environment.

Using the finite element method, [Chen et al. \(1991\)](#) studied the thermal buckling behaviour of composite laminated plates subjected to uniform and non-uniform temperature fields. In their study published in 2001, [Shukla & Nath \(2001\)](#) explored the buckling and post-buckling analysis of moderately thick angle-ply laminated composite rectangular plates. The plates were subjected to combined in-plane mechanical load and temperature gradient across the thickness. The problem was formulated using geometric non-linearity in the von Karman sense and first-order shear deformation theory. [Thankam et al. \(2003\)](#) studied the post-buckling behaviour of rectangular laminated plates subjected to thermal loads using the finite element method. [Matsunaga \(2005\)](#) proposed a two-dimensional global higher-order deformation theory for cross-ply laminated composite and sandwich plates for thermal buckling. [Shariyat \(2007\)](#) conducted a thermal buckling analysis of rectangular composite multi-layered plates subjected to uniform temperature rise using a layer-wise plate theory. The von Karman strain-displacement equations were utilised to account for large deflection occurrences. [Wu et al. \(2007\)](#) investigated the post-buckling response of a functionally graded materials plate

subjected to thermal and mechanical loads using rapidly converging double Chebyshev polynomials. [Kumar & Singh \(2009\)](#) presented a non-linear FEM analysis of laminated composite plates with SMA fibres subjected to uniform temperature to study buckling and post-buckling behaviour. In 2013, Gunda ([Gunda, 2013](#)) explored the thermal post-buckling paths of square plate configurations that are homogeneous, isotropic, and resting on an elastic foundation of the Winkler type. The plates were subjected to biaxial compressive thermal loads, and the results were expressed as simple closed-form solutions using the Rayleigh-Ritz method. The analysis accounted for the geometric non-linearity of the von Karman type. The study conducted by [Sreehari & Maiti \(2016\)](#) focuses on the creation of a finite element formulation that can effectively handle the analysis of bending, buckling, and post-buckling behaviours of composite laminated structures that have experienced damage. To achieve this, the researchers applied the inverse hyperbolic shear deformation theory in the creation of the finite element formulation.

Thermal buckling and post-buckling were studied by various researchers using a first-order shear deformation theory in conjunction with NURBS-based isogeometric analysis.

Isogeometric finite element analysis (IGA) was ([Nguyen-Xuan et al., 2014](#)) applied to study static, free vibration, and buckling analysis of functionally graded material plates using a refined plate theory. [Tran et al. \(2016\)](#) developed equilibrium and stability equations for plates of functionally graded material in a thermal environment using isogeometric analysis in conjunction with higher-order shear deformation theory.

[Kiani \(2018a\)](#) and [Kiani \(2020\)](#) investigated the thermal buckling and post-buckling behaviour of composite laminated skew plates reinforced by graphene platelets. The formulation uses the first-order shear deformation theory, Reddy's third-order shear deformation plate theory, and isogeometric analysis. [Kiani \(2018b\)](#) studied the post-buckling behaviour of a sandwich plate with FGCNTRC facings and Ti-6Al-4V core using a formulation based on FSDT.

[Farzam & Hassani \(2018\)](#) used isogeometric analysis (IGA) based on the modified couple stress theory to examine the thermal and mechanical buckling analysis of functionally graded carbon nanotube-reinforced composite plate. [Do & Lee \(2019\)](#) and [Fang et al. \(2021\)](#) explored the thermal buckling analysis of the functionally graded plate using 3D quasi-isogeometric analysis. [Do & Lee \(2021\)](#) examined the buckling and post-buckling behaviour of laminated composite plates containing functionally dispersed graphene platelets (GPLs) under various thermal loadings using deformable shear theory and isogeometric analysis. *Most of the existing studies have provided analytical solutions or used FEM with simplified imperfection models.*

However, the thermal stability characteristics of sandwich plates with a re-entrant core and initial geometric imperfection have not been explored.

2.6 Dynamic Instability Analysis and Non-linear Vibration

Dynamic instability occurs when a structure loses stability and experiences uncontrolled vibrations or deformations due to dynamic loading, temperature changes, material properties, or geometric configurations in sandwich plates. Various studies have thoroughly examined the dynamic instability of composite sandwich plates, focusing on the effects of CNTs. Researchers have explored several factors that influence this instability, such as the volume fraction of carbon nanotubes, thickness ratio between the core and face sheet, overall plate thickness, aspect ratio, damping, and temperature. (Sankar et al.(2016); Kamarian & Song (2023); Fu et al. (2016). Numerous authors have studied the dynamic instability of plates in various configurations. They studied the dynamic stability of plates, demonstrating the practical application of finite element and finite difference methods. Their research focused on analysing the behaviour of plates under varying conditions, using advanced mathematical techniques to model and predict dynamic stability. (R. Kumar et al. (2017);(Sahoo & Singh (2018); Lei et al. (2014); J. P. Singh & Dey (1992); Nguyen & Ostiguy (1989).Nguyen et al. (1989) conducted a comprehensive investigation into the dynamic instability and non-linear response of isotropic plates under the influence of different boundary conditions. The researchers conducted a comprehensive study that incorporated theoretical predictions and experimental analyses to gain valuable insights into the behaviour of sandwich plates in varying conditions. The study was mainly focused on evaluating the stability of the plates in thermal environments, which is a critical factor for ensuring their safe and reliable operation. It is important to thoroughly understand and effectively manage the dynamic instability of these structures. The thermal environment poses additional complexities and challenges, as temperature changes can induce thermal stresses and strains within the structure. This can cause variations in facings and core material properties, significantly altering sandwich plates' dynamic behaviour and stability. Properly accounting for these temperature-induced effects in the design and analysis processes is essential to avoid catastrophic consequences.

Recent studies have examined how temperature variation affects structural dynamic instability (Alijani & Amabili (2013); Wu et al. (2017); Fu et al. (2021); Chen et al. (2017). Plates can have imperfections that come in different forms, such as geometric deviations, surface

roughness, residual stresses, material inhomogeneities, and manufacturing defects. These deviations can negatively affect the mechanical properties of plates, leading to a decrease in their load-carrying capacity stiffness and an increase in stress concentrations. They can even cause premature failure. [Rafiee et al.\(2014\)](#) conducted a study on the non-linear dynamic instability of piezoelectric functionally graded carbon nanotube-reinforced composite plates under thermal and mechanical loads, considering initial geometric imperfection using the Galerkin approach. [Gu et al. \(2019\)](#) investigated the dynamic instability of a rotating cantilever cross-ply laminate thin-walled twisted plate with an exponential function type initial geometric imperfection using the Rayleigh-Ritz method and shallow shell theory. In their study [\(Li et al., 2023\)](#) investigated the dynamic buckling behaviour of an imperfect sandwich plate with an architected cellular core. They utilised the first-order shear deformation plate theory with the Von Karman non-linearity to construct the governing equation system, which was then solved using the Galerkin and fourth order Runge-Kutta methods.

An isogeometric method was used to investigate the dynamic stability of anisotropic composite plates with generic forms, as described by [Shafei et al. \(2019\)](#). [Nguyen et al. \(2020\)](#) used the isogeometric analysis to investigate the mechanical behaviour of FG graphene platelets reinforced porous plates, including buckling, vibration, and dynamic instability. [Mohammadi et al.\(2022\)](#) used IGA and higher-order shear deformation theory to analyse uniform in-plane loaded folded plates strengthened by carbon nanotubes (CNTs). This work is motivated by the importance of addressing dynamic instability in sandwich plates in thermal environments. The investigation will involve numerical analyses to explain the effects of temperature changes, material properties, and geometric configurations on the dynamic stability of sandwich plates.

This section delves into a detailed analysis of the non-linear vibration of both perfect and imperfect shear deformable plates, considering the application of thermo-electro-mechanical preload.

Using a semi-analytical approach, [Kitipornchai et al. \(2004\)](#) analysed non-linear vibration on laminated plates made of functionally graded material face sheets and homogeneous cores. [Chen et al. \(2006\)](#) performed a non-linear vibration analysis of an imperfect functionally graded material plate. They utilised the perturbation technique, which allowed them to investigate the plate's vibrational behaviour under various conditions. [Chen & Tan \(2007\)](#) conducted a study on the non-linear vibration behaviour of FGM plates that were initially stressed and had geometric imperfections. They utilised Galerkin's method to analyse the behaviour of an imperfect FGM plate and the Runge-Kutta method to solve the problem under

harmonic axial loading conditions. [Del Prado et al. \(2009\)](#) investigated a cylindrical shell's stability and non-linear vibration analysis with an initial geometric imperfection. In their 2011 study, Jagtap and colleagues [Jagtap et al. \(2011\)](#) explored the stochastic non-linear free vibration response of functionally graded materials plates, which were elastically supported and rested on a two-parameter Pasternak foundation with Winkler cubic non-linearity. In their research study, the researchers delved into the impact of uniform and non-uniform temperature fluctuations on various system properties, such as temperature-independent (TID) and temperature-dependent (TD) material properties. They employed a higher-order shear deformation theory, added by the finite element method and a first-order perturbation technique to conduct the analysis. Overall, aimed to gain a deeper understanding of how the system properties are affected by temperature changes, and the findings may have significant implications for related fields of study. [Belalia & Houmat \(2012\)](#) utilised a curved triangular p-element to investigate the non-linear free vibration properties of functionally graded shear deformable sector plates. The study employed the p-version of the finite element method to analyse non-linear free vibration in functionally graded sector plates, utilising a curved triangular p-element. Von Karman's assumptions were integrated with Mindlin's first-order shear deformation theory to account for geometric non-linearity. The shape functions were generated using shifted Legendre orthogonal polynomials. In a study conducted by [Gulshan Taj et al. \(2014\)](#), the vibration behaviour of FGM skew plates in a thermal environment was examined. The kinematics equations relied on Reddy's theory, and a 9-noded isoparametric Lagrangian element was utilised to mesh the plate shape. To determine the temperature profile of the plate along the thickness direction, a one-dimensional Fourier heat conduction equation was employed. [Gupta et al. \(2016\)](#) presented vibration characteristics of shear deformable functionally graded material plates using the C^0 isoparametric finite element method. [Parida & Mohanty \(2018\)](#) presented a free vibration analysis of skew FGM plate in thermal loading conditions using the finite element method in conjunction with higher-order shear deformation theory. [Kim et al. \(2019\)](#) proposed a semi-analytical method to study the non-linear dynamic response and vibration of a stiffened functionally graded plate resting on an elastic foundation that is eccentrically oblique. [Yang et al. \(2020\)](#) studied large amplitude non-linear vibration of carbon nanotube-reinforced composite (CNTRC) laminated plates with negative Poisson's ratios in thermal environments using the Reddy theory and the two-step perturbation technique. [Singh et al. \(2021\)](#) presented a study on the non-linear vibration and instability of carbon nanotube fibre-reinforced composite plates under different types of non-uniform in-plane periodic loadings. *Studies on the non-linear vibration behaviour of sandwich plates made up*

of FGCNTRC facings and re-entrant auxetic core materials in thermal environments are not readily available in the literature.

2.7 Summary

After a detailed review of the literature, the following gaps in the literature have been identified:

1. The efficiency of isogeometric analysis (IGA) with non-polynomial higher-order theory has not been explored in detail for the linear buckling and non-linear post-buckling and post-buckled vibration behaviour of sandwich plates made up of FGCNTRC facings and re-entrant auxetic core materials.
2. The literature on the non-linear stability behaviour of skew sandwich plates subjected to non-uniform mechanical loadings is limited.
3. The literature on the non-linear stability behaviour of skew sandwich plates with re-entrant auxetic cores subjected to thermal loading is scarce.
4. Studies on the non-linear vibration behaviour of sandwich plates made up of FGCNTRC facings and re-entrant auxetic core materials in thermal environments are not readily available in the literature.

Scope and Objectives

3.1 Introduction

The preceding chapter offers a comprehensive overview of the literature on buckling, post-buckling, and vibration attributes of isotropic, laminated, composite, and sandwich plates. It is worth noting that most research in this field has focused on the stability characteristics of isotropic, laminated plates and sandwich structures with honeycomb cores. Through an extensive review of the literature, it was discovered that there are no existing investigations on the post-buckling and free vibration of post-buckled skew sandwich plates with functionally graded carbon nanotube reinforced composite (FGCNTRC) facings and metal foam core subject to arbitrary edge loading conditions. Moreover, there are no studies available on the stability behaviour of sandwich structures with tunable auxetic cores having a negative Poisson ratio in a thermal environment. The non-linear vibration behaviour of the auxetic core-based sandwich plate in a thermal environment is also available in the literature, possibly due to the inherent complexities of the non-linear modelling of the sandwich plate. This study examines distinctive features of linear and non-linear plate behaviours, specifically on skew sandwich plates. As such, the objectives of the current investigation are outlined herein.

1. To develop an in-house MATLAB code to explore the efficiency of isogeometric analysis (IGA) with non-polynomial higher-order theory for stability and vibration characteristics of sandwich plates in mechanical or thermal environments.
2. To study the buckling, post-buckling and post-buckled vibration behaviour of initial imperfect sandwich plates with metal foam core (square, skew) under various mechanical loading (uniform, parabolic, sinusoidal, triangular and concentrated) and boundary conditions (simply supported and clamped).
3. To study the buckling and post-buckling behaviour of initial imperfect sandwich plates (square and skew) with an auxetic core having tunable material properties under thermal loading and different boundary conditions.
4. To investigate linear and non-linear vibration characteristics of auxetic core-based sandwich plates in the thermal environment.

Mathematical Formulation

4.1 Introduction

This thesis utilises the non-polynomial higher-order theory of plates for both linear and linear analyses of sandwich plates. Section 4.2 introduces a non-uniform rational B-spline (NURBS) based isogeometric analysis (IGA), followed by structural modelling and constitutive relations for isotropic and composite plates in Section 4.3. The transformed constitutive relation is presented in Section 4.4, while Section 4.5 covers the strain displacement relationship for the plate using non-polynomial higher-order theory. Section 4.6 delves into the effect of the mode of imperfection in the plate, and Section 4.7 presents the governing equation for problem formulation. Section 4.8 outlines the procedure for modelling the stability behaviour of the plate under non-uniform mechanical loading, while Section 4.9 covers thermal buckling and post-buckling analysis. Section 4.10 explores the non-linear vibration behaviours of the plate under thermal loading conditions. Section 4.11 presents the Newton-Raphson, force control displacement control, and arc length methods for solving non-linear equations. Finally, Section 4.12, Section 4.13 and section 4.14 discuss the procedure for numerical integration, imposing boundary conditions for various problems. Finally section 4.15 summarises the important contributions of this chapter.

4.2 Isogeometric Analysis (IGA)

IGA, an engineering analysis methodology based on using the exact representation of geometry, was proposed by [Hughes et al. \(2005\)](#). In IGA, NURBS basis functions approximate geometry and field variables. NURBS are weighted rational B-spline curves. The B-Spline basis functions are obtained using the Cox-de-Boor recursion formula. ([Cox \(1972\)](#); [de Boor \(1972\)](#))

$$N_{i,0}(\xi) = \begin{cases} 1 & \xi_i \leq \xi < \xi_{i+1} \\ 0 & \text{otherwise} \end{cases} \quad (4.1)$$

$$N_{i,p}(\xi) = \frac{\xi - \xi_i}{\xi_{i+p} - \xi_i} N_{i,p-1}(\xi) + \frac{\xi_{i+p+1} - \xi}{\xi_{i+p+1} - \xi_{i+1}} N_{i+1,p-1}(\xi) \quad (4.2)$$

Here ξ is the knot value in the knot vector, $\mathcal{E} = \{\xi_1, \xi_2, \dots, \xi_{n+p+1}\}$, p is the degree of the B-spline curve, and n is the number of control points in the physical space.

Let $N_{i,p}(\xi)$ be p -th order B-spline function defined by the knot vector $\Xi = [\xi_1, \dots, \xi_{n+p+1}]$

The derivative of the B-spline function $\frac{d}{d\xi} N_{i,p}(\xi)$ is calculated recursively as

$$\frac{d}{d\xi} N_{i,p}(\xi) = \frac{p}{\xi_{i+p} - \xi_i} N_{i,p-1}(\xi) - \frac{p}{\xi_{i+p+1} - \xi_{i+1}} N_{i+1,p-1}(\xi) \quad (4.3)$$

This can be proven by mathematical induction. The k^{th} derivative of the B-spline function, denoted by $N_{i,p}^{(k)}$ also can be computed by

$$N_{i,p}^{(k)} = p \left(\frac{N_{i,p-1}^{(k-1)}}{\xi_{i+p} - \xi_i} - \frac{N_{i+1,p-1}^{(k-1)}}{\xi_{i+p+1} - \xi_{i+1}} \right) \quad (4.4)$$

Alternatively, the k^{th} derivative may be computed in terms of B-spline functions such that

$$N_{i,p}^{(k)} = \frac{p!}{(p-k)!} \sum_{j=0}^k a_{k,j} N_{i+j,p-k}(\xi) \quad (4.5)$$

Where

$$\begin{aligned} a_{0,0} &= 1 \\ a_{k,0} &= \frac{a_{k-1,0}}{\xi_{i+p-k+1} - \xi_i} \\ a_{k,j} &= \frac{a_{k-1,j} - a_{k-1,j-1}}{\xi_{i+p+j-k+1} - \xi_{i+j}} \quad j = 1, 2, \dots, k-1 \\ a_{k,k} &= \frac{-a_{k-1,k-1}}{\xi_{i+p+1} - \xi_{i+k}}. \end{aligned} \quad (4.6)$$

For the given knot vector p -th order NURBS basis function is given by

$$\varphi_i^p(\xi) = \frac{N_{i,p}(\xi)\omega_i}{\sum_{i=1}^n N_{i,p}(\xi)\omega_i} \quad (4.7)$$

Where ω_i are the weights and $N_{i,p}(\xi)$ is the B-spline basis function.

Applying corresponding control points P_i to the NURBS function, the NURBS curve can be derived as

$$\mathbf{C}(\xi) = \sum_{i=1}^n \varphi_i^p(\xi) P_i \quad (4.8)$$

A two-dimensional NURBS basis function is defined as follows:

$$\varphi_{i,j}^{p,q}(\xi, \eta) = \frac{N_{i,p}(\xi)M_{j,q}(\eta)\omega_{i,j}}{\sum_{i=1}^n \sum_{j=1}^m N_{i,p}(\xi)M_{j,q}(\eta)\omega_{i,j}} \quad (4.9)$$

Where $N_{i,p}$ and $M_{j,q}$ are the B-Spline basis functions with orders p, q respectively in two different directions, defined by the knot vectors

The derivative of the NURBS function is given by

$$\frac{d}{d\xi} \varphi_i^p(\xi) = \omega_i \frac{W(\xi)N'_{i,p}(\xi) - W'(\xi)N_{i,p}(\xi)}{(W(\xi))^2} \quad (4.10)$$

$$\text{where } N'_{i,p} = \frac{d}{d\xi} N_{i,p}(\xi) \text{ and } W'(\xi) = \sum_{i=1}^n N'_{i,p}(\xi)\omega_i$$

$\Xi_1 = \{\xi_1, \xi_2, \dots, \xi_{n+p+1}\}$, $\Xi_2 = \{\eta_1, \eta_2, \dots, \eta_{m+p+1}\}$ in the parametric, space with n, m is the number of control points in the respective directions coordinates. The solution variables are approximated as a linear combination of basis functions, and the values of the variable at control points are as follows:

$$S(\xi, \eta) = \sum_{i=1}^n \sum_{j=1}^m \varphi_{i,j}^{p,q} P_{i,j} \quad (4.11)$$

Where $P_{i,j}$ represents the corresponding values at the control points. A detailed derivation of NURBS-based approximation can be found in [Hughes et al. \(2005\)](#)

4.3 Structural Modelling

Structures analysed in the present investigation are assumed to consist of elastic and homogenous material. Both isotropic and orthotropic materials are considered in the present work. The stress-strain (constitutive) relations are given in the following section ([Watts et al., 2017](#)).

$$\begin{Bmatrix} \sigma_1 \\ \sigma_2 \\ \tau_{12} \end{Bmatrix} = \begin{bmatrix} Q_{11} & Q_{12} & 0 \\ Q_{12} & Q_{11} & 0 \\ 0 & 0 & Q_{66} \end{bmatrix} \begin{bmatrix} \varepsilon_1 \\ \varepsilon_2 \\ \gamma_{12} \end{bmatrix} \quad (4.12)$$

$$\begin{Bmatrix} \tau_{23} \\ \tau_{13} \end{Bmatrix} = \begin{bmatrix} Q_{23} & 0 \\ 0 & Q_{13} \end{bmatrix} \begin{bmatrix} \gamma_{23} \\ \gamma_{13} \end{bmatrix} \quad (4.13)$$

Where '1' represents the direction along the fibers of the lamina. '2' and '3' are directions perpendicular to the fiber. Q_{ij} re plane-stress reduced stiffness coefficients which are related to engineering constants as follows (Watts et al., 2017)

4.3.1 Isotropic Material

$$Q_{11} = \frac{E}{(1-\nu^2)}, Q_{12} = \frac{\nu E}{(1-\nu^2)}, Q_{66} = G, Q_{23} = Q_{13} = G \quad (4.14)$$

4.3.2 Orthotropic Material

$$\begin{aligned} Q_{11} &= \frac{E_1}{(1-\nu_{12}\nu_{21})}, Q_{22} = \frac{E_2}{(1-\nu_{12}\nu_{21})}; Q_{12} = \frac{\nu_{12}E_2}{(1-\nu_{12}\nu_{21})} = \frac{\nu_{21}E_1}{(1-\nu_{12}\nu_{21})} \\ Q_{66} &= G_{12}, Q_{23} = G_{23}, Q_{13} = G_{13} \end{aligned} \quad (4.15)$$

4.4 Transformed Constitutive Relations

In a laminated composite structure, the fibres of the lamina are inclined at an angle β_f to the global x -axis. Therefore, constitutive relations must be transformed from local to global coordinate systems.

Transformation of constitutive relations in global $x - y$ coordinate system for a k^{th} lamina is given by (Watts et al., 2017)

$$\begin{Bmatrix} \sigma_{xx} \\ \sigma_{yy} \\ \tau_{xy} \end{Bmatrix}_k = \begin{bmatrix} \bar{Q}_{11} & \bar{Q}_{12} & \bar{Q}_{16} \\ \bar{Q}_{21} & \bar{Q}_{22} & \bar{Q}_{26} \\ \bar{Q}_{16} & \bar{Q}_{26} & \bar{Q}_{66} \end{bmatrix}_k \begin{Bmatrix} \varepsilon_{xx} \\ \varepsilon_{yy} \\ \gamma_{xy} \end{Bmatrix}_k = \bar{\mathbf{Q}} \bar{\boldsymbol{\varepsilon}}_1 \quad (4.16)$$

$$\begin{Bmatrix} \tau_{yz} \\ \tau_{xz} \end{Bmatrix}_k = \begin{bmatrix} \bar{Q}_{44} & \bar{Q}_{45} \\ \bar{Q}_{45} & \bar{Q}_{55} \end{bmatrix}_k \begin{Bmatrix} \gamma_{yz} \\ \gamma_{xz} \end{Bmatrix}_k = \bar{\mathbf{P}} \bar{\boldsymbol{\varepsilon}}_2 \quad (4.17)$$

$$\bar{\mathbf{Q}} = \mathbf{T} \mathbf{Q} \mathbf{T}' \quad \text{and} \quad \bar{\mathbf{P}} = \mathbf{T}_1 \mathbf{P} \mathbf{T}'_1 \quad (4.18)$$

$\mathbf{P}, \mathbf{Q}, \mathbf{T}$ and \mathbf{T}_1 are defined as

$$\mathbf{Q} = \begin{bmatrix} Q_{11} & Q_{12} & 0 \\ Q_{12} & Q_{11} & 0 \\ 0 & 0 & Q_{66} \end{bmatrix} \quad (4.19)$$

$$\mathbf{P} = \begin{bmatrix} Q_{23} & 0 \\ 0 & Q_{13} \end{bmatrix} \quad (4.20)$$

$$\mathbf{T} = \begin{bmatrix} \cos^2 \beta_f & \sin^2 \beta_f & -2\sin \beta_f \cos \beta_f \\ \sin^2 \beta_f & \cos^2 \beta_f & 2\sin \beta_f \cos \beta_f \\ \sin \beta_f \cos \beta_f & -\sin \beta_f \cos \beta_f & \cos^2 \beta_f - \sin^2 \beta_f \end{bmatrix} \quad (4.21)$$

$$\mathbf{T}_1 = \begin{bmatrix} \cos \beta_f & \sin \beta_f \\ -\sin \beta_f & \cos \beta_f \end{bmatrix} \quad (4.22)$$

The equations (4.16-4.17) are combined and written as

$$\boldsymbol{\sigma} = \begin{bmatrix} \bar{\mathbf{Q}} & 0 \\ 0 & \bar{\mathbf{P}} \end{bmatrix} \begin{Bmatrix} \bar{\boldsymbol{\epsilon}}_1 \\ \bar{\boldsymbol{\epsilon}}_2 \end{Bmatrix} = \mathbf{D}\boldsymbol{\epsilon} \quad (4.23)$$

4.5 Strain-Displacement Relations

The kinematic assumptions of the mid-plane of the plate with thickness h are formulated on the non-polynomial higher-order theory [Watts et al. \(2020\)](#)

$$u(x, y, z) = u_0(x, y) - z \frac{\partial w_0(x, y)}{\partial x} + f(z)\theta_x(x, y) \quad (4.24)$$

$$v(x, y, z) = v_0(x, y) - z \frac{\partial w_0(x, y)}{\partial y} + f(z)\theta_y(x, y) \quad (4.25)$$

$$w(x, y, z) = w_0(x, y) \quad (4.26)$$

u_0, v_0 are displacements in x and y direction and w_0 is the displacement in the z -direction at any point on the middle plane. θ_y and θ_x are normal to the mid-plane rotations about the x and y -axis, respectively. The exponential function, $f(z) = \left(z e^{1 - \frac{4z^2}{h^2}} + z \right)$ is derived to satisfy zero transverse shear conditions at the top and bottom surfaces of the sandwich laminate as shown

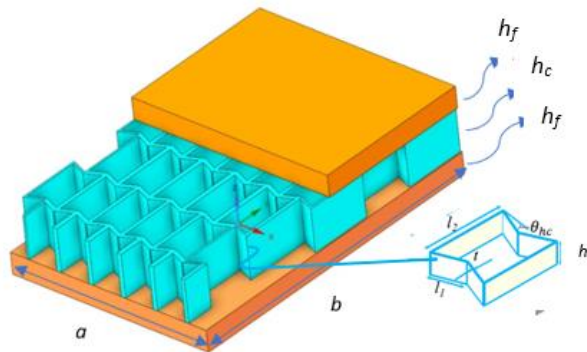


Figure 4.1: Sandwich Plate

in Figure 4.1

Additionally, h_c refers to the thickness of the auxetic core, and h_f represents the facings thickness of the top layer, which is equal to the thickness of the bottom layer.

The displacements are approximated using NURBS basis functions as follows:

$$q = \begin{Bmatrix} u_0 \\ v_0 \\ w_0 \\ \theta_x \\ \theta_y \end{Bmatrix} = \sum_{i=1}^{n \times m} \begin{bmatrix} \varphi_i & 0 & 0 & 0 & 0 \\ 0 & \varphi_i & 0 & 0 & 0 \\ 0 & 0 & \varphi_i & 0 & 0 \\ 0 & 0 & 0 & \varphi_i & 0 \\ 0 & 0 & 0 & 0 & \varphi_i \end{bmatrix} \begin{Bmatrix} u_{0i} \\ v_{0i} \\ w_{0i} \\ \theta_{xi} \\ \theta_{yi} \end{Bmatrix} = \sum_{i=1}^{n \times m} \varphi_i q_i \quad (4.27)$$

where φ_i is the NURBS-based approximation function and $(u_{0i}, v_{0i}, w_{0i}, \theta_{xi}, \theta_{yi})^T$ are the degrees of freedom of control point P_i .

The strain displacement relations are as follows:

$$\begin{Bmatrix} \varepsilon_{xx} \\ \varepsilon_{yy} \\ \gamma_{xy} \end{Bmatrix} = \begin{Bmatrix} \frac{\partial u_0}{\partial x} \\ \frac{\partial v_0}{\partial y} \\ \frac{\partial u_0}{\partial y} + \frac{\partial v_0}{\partial x} \end{Bmatrix} - z \begin{Bmatrix} \frac{\partial^2 w_0}{\partial x^2} \\ \frac{\partial^2 w_0}{\partial y^2} \\ 2 \frac{\partial^2 w_0}{\partial x \partial y} \end{Bmatrix} + f(z) \begin{Bmatrix} \frac{\partial \theta_x}{\partial x} \\ \frac{\partial \theta_y}{\partial y} \\ \frac{\partial \theta_x}{\partial y} + \frac{\partial \theta_y}{\partial x} \end{Bmatrix} + \frac{1}{2} \begin{Bmatrix} \left(\frac{\partial w_0}{\partial x} \right)^2 \\ \left(\frac{\partial w_0}{\partial y} \right)^2 \\ 2 \frac{\partial w_0}{\partial x} \frac{\partial w_0}{\partial y} \end{Bmatrix} \quad (4.28)$$

$$\begin{Bmatrix} \gamma_{xz} \\ \gamma_{yz} \end{Bmatrix} = \frac{\partial f(z)}{\partial z} \begin{Bmatrix} \theta_x \\ \theta_y \end{Bmatrix} \quad (4.29)$$

The non-linear component of in-plane strain can be written as:

$$\boldsymbol{\varepsilon}_{NL} = \frac{1}{2} \mathbf{H}_\theta \boldsymbol{\theta} \quad (4.30)$$

where

$$\mathbf{H}_\theta = \begin{bmatrix} w_{0,x} & 0 \\ 0 & w_{0,y} \\ w_{0,y} & w_{0,x} \end{bmatrix} \text{ and } \boldsymbol{\theta} = \begin{Bmatrix} w_{0,x} \\ w_{0,y} \end{Bmatrix}$$

The net strains, after including initial imperfections, can be rewritten as:

$$\varepsilon_1 = \varepsilon_m - z\varepsilon_h + f(z)\varepsilon_b + \varepsilon_{nl} + \varepsilon_I \quad (4.31)$$

$$\varepsilon_m = \sum_{i=1}^{ncp} \begin{bmatrix} \varphi_{i,x} & 0 & 0 & 0 & 0 \\ 0 & \varphi_{i,y} & 0 & 0 & 0 \\ \varphi_{i,y} & \varphi_{i,x} & 0 & 0 & 0 \end{bmatrix} \begin{bmatrix} u_{0i} \\ v_{0i} \\ w_{0i} \\ \theta_{xi} \\ \theta_{yi} \end{bmatrix} = \mathbf{B}_m \mathbf{q} \quad (4.32)$$

$$\varepsilon_h = \sum_{i=1}^{ncp} \begin{bmatrix} 0 & 0 & \varphi_{i,x x} & 0 & 0 \\ 0 & 0 & \varphi_{i,y y} & 0 & 0 \\ 0 & 0 & 2\varphi_{i,x y} & 0 & 0 \end{bmatrix} \begin{bmatrix} u_{0i} \\ v_{0i} \\ w_{0i} \\ \theta_{xi} \\ \theta_{yi} \end{bmatrix} = \mathbf{B}_h \mathbf{q} \quad (4.33)$$

$$\varepsilon_b = \sum_{i=1}^{ncp} \begin{bmatrix} 0 & 0 & 0 & \varphi_{i,x} & 0 \\ 0 & 0 & 0 & 0 & \varphi_{i,y} \\ 0 & 0 & 0 & \varphi_{i,y} & \varphi_{i,x} \end{bmatrix} \begin{bmatrix} u_{0i} \\ v_{0i} \\ w_{0i} \\ \theta_{xi} \\ \theta_{yi} \end{bmatrix} = \mathbf{B}_b \mathbf{q} \quad (4.34)$$

$$\varepsilon_{nl} = \sum_{i=1}^{ncp} \frac{1}{2} \begin{bmatrix} w_{0,x} & 0 \\ 0 & w_{0,y} \\ w_{0,y} & w_{0,x} \end{bmatrix} \begin{bmatrix} 0 & 0 & \varphi_{i,x} & 0 & 0 \\ 0 & 0 & \varphi_{i,y} & 0 & 0 \end{bmatrix} \begin{bmatrix} u_{0i} \\ v_{0i} \\ w_{0i} \\ \theta_{xi} \\ \theta_{yi} \end{bmatrix} = \mathbf{B}_{nl} \mathbf{q} \quad (4.35)$$

$$\varepsilon_I = \left\{ \begin{array}{l} \frac{\partial w_0}{\partial x} \frac{\partial w^*}{\partial x} \\ \frac{\partial w_0}{\partial y} \frac{\partial w^*}{\partial y} \\ \frac{\partial w_0}{\partial x} \frac{\partial w^*}{\partial y} + \frac{\partial w_0}{\partial y} \frac{\partial w^*}{\partial x} \end{array} \right\} = \sum_{i=1}^{ncp} \begin{bmatrix} w_x^* & 0 \\ 0 & w_y^* \\ w_y^* & w_x^* \end{bmatrix} \begin{bmatrix} 0 & 0 & \varphi_{i,x} & 0 & 0 \\ 0 & 0 & \varphi_{i,y} & 0 & 0 \end{bmatrix} = \mathbf{B}_I \mathbf{q} \quad (4.36)$$

$$\varepsilon_2 = \sum_{i=1}^{ncp} \begin{bmatrix} \frac{\partial f(z)}{\partial z} \end{bmatrix} \begin{bmatrix} 0 & 0 & 0 & \varphi_i & 0 \\ 0 & 0 & 0 & 0 & \varphi_i \end{bmatrix} \begin{bmatrix} u_{0i} \\ v_{0i} \\ w_{0i} \\ \theta_{xi} \\ \theta_{yi} \end{bmatrix} = \mathbf{B}_\gamma \mathbf{q} \quad (4.37)$$

where $[, x]$ and $[, y]$ denotes derivatives with respect to x and y , respectively. Using equations (4.32) - (4.37), strains are written as

$$\varepsilon = \begin{Bmatrix} \mathbf{B}_m^L \\ \mathbf{B}_\gamma \end{Bmatrix} \mathbf{q} + \frac{1}{2} \begin{Bmatrix} \mathbf{B}_m^{NL} \\ 0 \end{Bmatrix} \mathbf{q} + f(z) \begin{Bmatrix} \mathbf{B}_h \\ 0 \end{Bmatrix} \mathbf{q} + z \begin{Bmatrix} \mathbf{B}_b \\ 0 \end{Bmatrix} \mathbf{q} \quad (4.38)$$

$$\begin{aligned}\Rightarrow \varepsilon &= \begin{Bmatrix} \mathbf{B}_m^L + z\mathbf{B}_b + \mathbf{B}_h \\ \mathbf{B}_\gamma \end{Bmatrix} \mathbf{q} + \frac{1}{2} \begin{Bmatrix} \mathbf{B}_m^{NL} \\ 0 \end{Bmatrix} \mathbf{q} \\ \Rightarrow \varepsilon &= \varepsilon_L + \varepsilon_{NL} = \begin{Bmatrix} \mathbf{B}_L \\ \mathbf{B}_{NL} \end{Bmatrix} \mathbf{q}\end{aligned}$$

ε_L and ε_{NL} are the linear and non-linear components of strain, respectively.

4.6 Influence of Mode of Imperfections

The strains due to initial imperfection at the mid-surface can be written as (Girish & Ramachandra, 2005)

$$\varepsilon_x^* = \frac{1}{2}(w_{,x}^*)^2; \quad \varepsilon_y^* = \frac{1}{2}(w_{,y}^*)^2; \quad \gamma_{xy}^* = w_{,x}^*w_{,y}^*; \quad \gamma_{xz}^* = w_{,x}^*; \quad \gamma_{yz}^* = w_{,y}^* \quad (4.39)$$

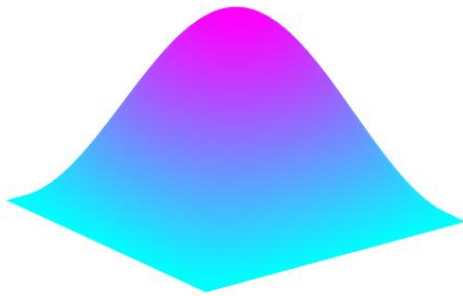
An imperfection function combines trigonometric and hyperbolic functions introduced previously by Kitipornchai et al. (2004). The imperfection considered in the present work is given by

$$w^* = \mu h \sec h \left[\delta_1 \left(\frac{x}{a} - \beta_1 \right) \right] \cos \left[\mu_1 \pi \left(\frac{x}{a} - \beta_1 \right) \right] \times \sec h \left[\delta_2 \left(\frac{y}{b} - \beta_2 \right) \right] \cos \left[\mu_2 \pi \left(\frac{y}{b} - \beta_2 \right) \right] \quad (4.40)$$

In the imperfection function, the symbol μ denotes the amplitude of imperfection, which exhibits values ranging from 0 to 1. The constants δ_1 and δ_2 serve to refer to the localised imperfection order, which possesses symmetry concerning $x/a = \beta_1$ and $y/b = \beta_2$, respectively. Additionally, μ_1 and μ_2 represent the half-wave numbers of the imperfection along the x and y axes, and h is the thickness of the plate. To better understand the effect of geometric imperfection's shape on the plate's buckling strength, two distinct forms of imperfection types, namely sinusoidal type and local imperfection (L2), are selected in the present investigation, as illustrated in Figure 4.2

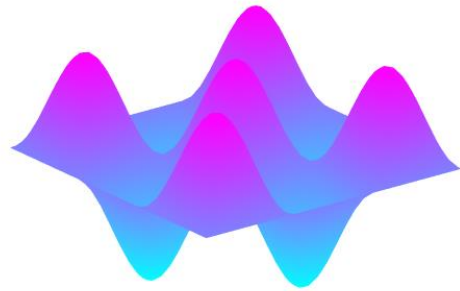
Figure 4.2: Description of various modes of initial Imperfections(Kitipornchai et al., 2004)

Sine type



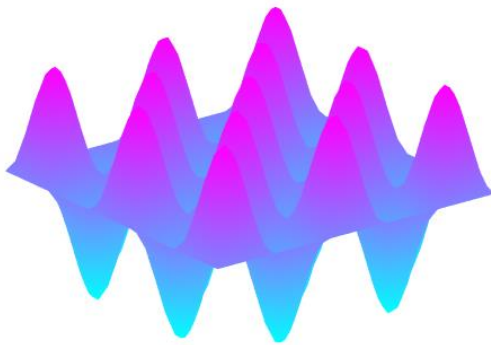
$$\delta_1 = \delta_2 = 0, \mu_1 = \mu_2 = 1, \beta_1 = \beta_2 = 0.5$$

G1



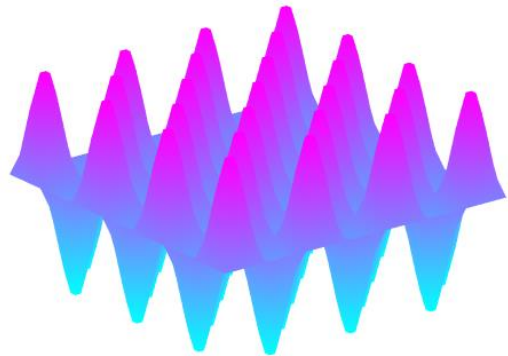
$$\delta_1 = \delta_2 = 0, \mu_1 = \mu_2 = 3, \beta_1 = \beta_2 = 0.5$$

G2



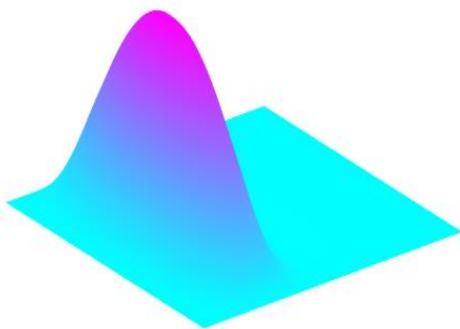
$$\delta_1 = \delta_2 = 0, \mu_1 = \mu_2 = 5, \beta_1 = \beta_2 = 0.5$$

G3



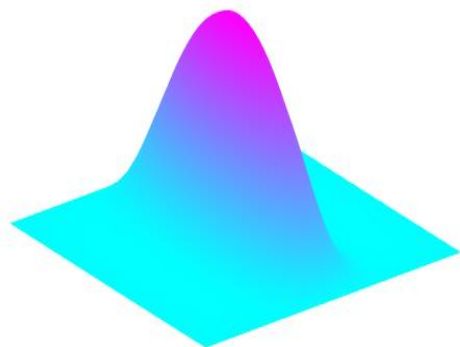
$$\delta_1 = \delta_2 = 0, \mu_1 = \mu_2 = 7, \beta_1 = \beta_2 = 0.5$$

L1



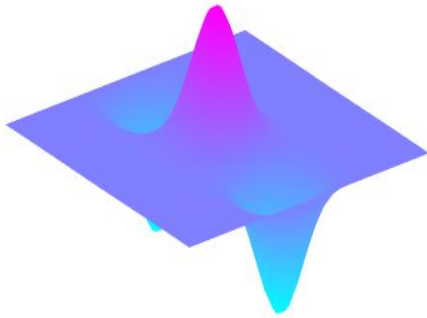
$$\delta_1 = 15, \delta_2 = 0, \mu_1 = 2, \mu_2 = 1, \beta_1 = 0.25, \beta_2 = 0.5$$

L2



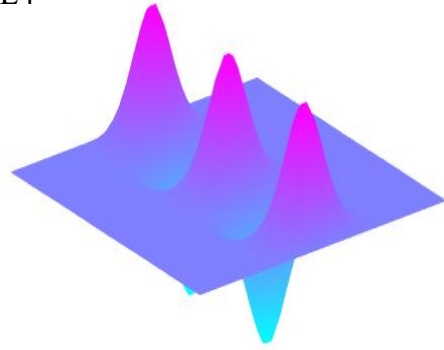
$$\delta_1 = 15, \delta_2 = 0, \mu_1 = 2, \mu_2 = 1, \beta_1 = 0.5, \beta_2 = 0.5$$

L3



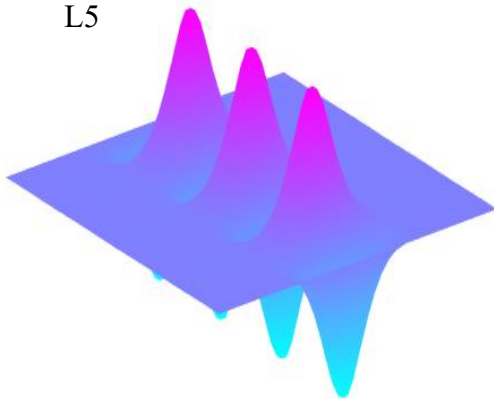
$$\delta_1 = 15, \delta_2 = 0, \mu_1 = 2, \mu_2 = 3, \beta_1 = 0.5, \beta_2 = 0.5$$

L4



$$\delta_1 = 15, \delta_2 = 0, \mu_1 = 2, \mu_2 = 5, \beta_1 = 0.5, \beta_2 = 0.5$$

L5



$$\delta_1 = 15, \delta_2 = 0, \mu_1 = 2, \mu_2 = 7, \beta_1 = 0.5, \beta_2 = 0.5$$

In non-uniform mechanical loading, it is assumed that the geometric imperfection of the plate is proportional to the first eigen-buckling mode shape and may be written as

$$\Delta = w_{max}^*/a \quad (4.41)$$

where w_{max}^* is the maximum value of imperfection.

4.7 Governing Equations

The governing equations of the plate structure are derived from the principle of virtual displacement (Tran, 2016)

$$\int_0^t (\delta U + \delta V - \delta K) dt = 0 \quad (4.42)$$

where the virtual strain energy δU is defined as:

$$\delta U = \int_V \delta \hat{\boldsymbol{\varepsilon}}^T \hat{\boldsymbol{\sigma}} dV \quad (4.43)$$

Before proceeding with the discretisation of the virtual strain energy in Eq. (4.42), it is necessary to consider further the variation of strain $\delta \hat{\boldsymbol{\varepsilon}}$ due to the virtual displacements as the sum of the variation of the linear and non-linear generalised strains as:

$$\delta \hat{\boldsymbol{\varepsilon}} = \delta \hat{\boldsymbol{\varepsilon}}_L + \delta \hat{\boldsymbol{\varepsilon}}_{NL} \quad (4.44)$$

where the variation of the non-linear component of the in-plane strain is obtained from Eq. (4.30) as:

$$\delta \boldsymbol{\varepsilon}_{NL} = H_\theta \delta \boldsymbol{\theta} \quad (4.45)$$

Substituting the stress and strain in the virtual strain energy is rewritten as:

$$\delta U = \int_\Omega \delta \hat{\boldsymbol{\varepsilon}}^T \hat{\mathbf{D}} \hat{\boldsymbol{\varepsilon}} - \delta \hat{\boldsymbol{\varepsilon}}^T \hat{\boldsymbol{\sigma}}_{th} d\Omega \quad (4.46)$$

The virtual work done by external forces

$$\delta V = - \int_\Omega \delta \mathbf{q}^T \bar{\mathbf{f}} d\Omega - \int_\Gamma \delta \mathbf{q}^T \bar{\mathbf{t}} d\Gamma \quad (4.47)$$

Where q presents the displacement field, $\bar{\mathbf{f}}$ represents the external load and $\bar{\mathbf{t}}$ is the prescribed traction on the natural boundaries. And the virtual kinetic energy is:

$$\delta K = \int_V \delta \dot{\mathbf{q}}^T \rho \dot{\mathbf{q}} dV \quad (4.48)$$

where ρ is the effective density of the material, and a dotted variable indicates its time derivative. Integrating Eq. (4.48) by part with respect to time, obtained a new form of the virtual kinetic energy.

$$\int_0^t \delta K dt = - \int_0^t \left(\int_V \delta \ddot{\mathbf{q}}^T \rho \mathbf{q} dV \right) dt \quad (4.49)$$

4.8 Stability Behaviour Under Non Uniform Mechanical Load

The in-plane forces, moments, higher-order forces and shear forces are expressed as (Sengar et al., 2023)

$$\begin{Bmatrix} \mathbf{N} \\ \mathbf{M} \\ \mathbf{P} \\ \mathbf{R} \end{Bmatrix} = \hat{\mathbf{D}} \hat{\boldsymbol{\varepsilon}} = \begin{bmatrix} \mathbf{A} & \mathbf{B} & \mathbf{E} & \mathbf{0} \\ \mathbf{B} & \mathbf{D} & \mathbf{F} & \mathbf{0} \\ \mathbf{E} & \mathbf{F} & \mathbf{H} & \mathbf{0} \\ \mathbf{0} & \mathbf{0} & \mathbf{0} & D^s \end{bmatrix} \begin{Bmatrix} \varepsilon_m \\ \varepsilon_h \\ \varepsilon_b \\ \varepsilon_\gamma \end{Bmatrix} \quad (4.50)$$

$$\begin{Bmatrix} \mathbf{N} \\ \mathbf{M} \\ \mathbf{P} \end{Bmatrix} = \sum_{k=1}^3 \int_{Z_k}^{Z_{k+1}} \boldsymbol{\sigma} \begin{Bmatrix} 1 \\ z \\ f(z) \end{Bmatrix} dz \quad (4.51)$$

$$\mathbf{R} = \sum_{k=1}^3 \int_{Z_k}^{Z_{k+1}} f'(z) \tau dz \quad (4.52)$$

$$(A_{ij}, B_{ij}, D_{ij}, E_{ij}, F_{ij}, H_{ij}) = \sum_{k=1}^3 \int_{Z_k}^{Z_{k+1}} Q_{ij}^k(1, z, z^2, f(z), zf(z), f^2(z)) dz \quad (4.53)$$

$$D_{\alpha\beta}^s = \sum_{k=1}^3 \int_{Z_k}^{Z_{k+1}} (f'(z))^2 P_{\alpha\beta} dz, (i, j, k = 1, 2, 3; \alpha, \beta = 1, 2) \quad (4.54)$$

Where $\hat{\mathbf{D}}$ is the rigidity matrix composed of the membrane, bending coupling and shear rigidity matrix. Q and G are material matrices.

The governing equations can be derived using Hamilton's principle (Watts et al., 2020)

$$\delta \int_{t_1}^{t_2} (T - U_s + W) dt = 0 \quad (4.55)$$

Where δ denotes the first variation, T and U_s are total kinetic and strain energy, respectively. W represents the work due to external loads and can be written as (Watts et al., 2020)

$$W = \frac{1}{2} \int_{r_p} \left[N_{xx} \left(\frac{\partial w_0}{\partial x} \right)^2 + N_{yy} \left(\frac{\partial w_0}{\partial y} \right)^2 + 2N_{xy} \left(\frac{\partial w_0}{\partial x} \right) \left(\frac{\partial w_0}{\partial y} \right) \right] d\Gamma_p \quad (4.56)$$

where Γ_p denotes the surface area of the mid-plane. N_{xx}, N_{yy}, N_{xy} are the pre-buckling stress components, which can be obtained as follows:

$$\begin{bmatrix} N_{xx} \\ N_{yy} \\ N_{xy} \end{bmatrix} = \sum_{i=1}^{NL} \int_{z_k}^{z_{k+1}} \begin{bmatrix} \sigma_{xx} \\ \sigma_{yy} \\ \sigma_{xy} \end{bmatrix} dz \quad (4.57)$$

where NL denotes the number of layers in the sandwich composite.

The weak form can be transformed into algebraic equations using a standard procedure. The algebraic equations, thus obtained, may be written as:

$$\mathbf{M}\ddot{\mathbf{X}} + \{\mathbf{K}_L + \mathbf{K}_{NL}\}\mathbf{X} = \mathbf{0} \quad (4.58)$$

Where \mathbf{M} is the mass matrix, \mathbf{K}_L is the linear stiffness matrix, and \mathbf{K}_{NL} is the non-linear stiffness matrix. The pre-buckled and post-buckled vibration behaviours can be analysed by assuming the displacement as a combination of static and time-dependent deflections:

$$\mathbf{X} = \mathbf{X}_s + \mathbf{X}_t \quad (4.59)$$

Where \mathbf{X}_s is static, and \mathbf{X}_t is the time-dependent deformation. The governing equations for post-buckling and the post-buckled configuration can be obtained by neglecting higher-order terms as follows:

$$\{\mathbf{K}_L + \mathbf{K}_{NL}\}\mathbf{X}_s = \mathbf{F} \quad (4.60)$$

$$\mathbf{M}\ddot{\mathbf{X}} + \{\mathbf{K}_L + \mathbf{K}_{NL}\}\mathbf{X}_t = \mathbf{0} \quad (4.61)$$

By assuming a sinusoidal response,

$$\mathbf{X}_t = \bar{\mathbf{X}} \sin \omega t \quad (4.62)$$

the above equation can be modified as an eigenvalue problem, which can be solved to obtain free vibration frequencies.

$$|\mathbf{K}_T - \omega^2 \mathbf{M}| \quad (4.63)$$

where \mathbf{K}_T is the tangent stiffness matrix.

The mass matrix is given by

$$\mathbf{M} = \int_{\Gamma_p} [\mathbf{S}^T \mathbf{Y} \mathbf{S}] d\Gamma_p \quad (4.64)$$

$$\mathbf{S} = \begin{bmatrix} \varphi_i & [0] & [0] & [0] & [0] \\ [0] & \varphi_i & [0] & [0] & [0] \\ [0] & [0] & \varphi_i & [0] & [0] \\ [0] & [0] & \varphi_{i,x} & [0] & [0] \\ [0] & [0] & \varphi_{i,y} & [0] & [0] \\ [0] & [0] & [0] & [\varphi_i] & [0] \\ [0] & [0] & [0] & [0] & \varphi_i \end{bmatrix} \quad (4.65)$$

$$\mathbf{Y} = \begin{bmatrix} I_0 & 0 & 0 & -I_1 & 0 & I_3 & 0 \\ 0 & I_0 & 0 & 0 & -I_1 & 0 & I_3 \\ 0 & 0 & I_0 & 0 & 0 & 0 & 0 \\ -I_1 & 0 & 0 & I_2 & 0 & -I_4 & 0 \\ 0 & -I_1 & 0 & 0 & I_2 & 0 & -I_4 \\ I_3 & 0 & 0 & -I_4 & 0 & I_5 & 0 \\ 0 & I_3 & 0 & 0 & -I_4 & 0 & I_5 \end{bmatrix} \quad (4.66)$$

Where

$$I_0, I_1, I_2, I_3, I_4, I_5 = \sum_{k=1}^{NL} \int_{z_k}^{z_{k+1}} \rho_s^k \{1, z, z^2, f, zf, f^2\} dz \quad (4.67)$$

4.9 Stability Behaviour of Plate Under Thermal Environment

The stress-strain relations for k^{th} lamina can be written as (Sengar et al., 2024):

$$\begin{bmatrix} \sigma_{xx} \\ \sigma_{yy} \\ \tau_{xy} \end{bmatrix}^k = \begin{bmatrix} Q_{11}^k & Q_{12}^k & 0 \\ Q_{21}^k & Q_{22}^k & 0 \\ 0 & 0 & Q_{33}^k \end{bmatrix} \begin{bmatrix} \varepsilon_{xx} \\ \varepsilon_{yy} \\ \gamma_{xy} \end{bmatrix}^k \quad \text{and} \quad \begin{bmatrix} \tau_{yz} \\ \tau_{xz} \end{bmatrix}^k = \begin{bmatrix} P_{11}^k & 0 \\ 0 & P_{22}^k \end{bmatrix} \begin{bmatrix} \gamma_{yz} \\ \gamma_{xz} \end{bmatrix}^k \quad (4.68)$$

Where

$$Q_{11} = \frac{E_1}{1 - \nu_{12}\nu_{21}}; Q_{22} = \frac{E_2}{1 - \nu_{12}\nu_{21}}; Q_{12} = Q_{21} = \frac{E_2\nu_{12}}{1 - \nu_{12}\nu_{21}}; \\ Q_{33} = G_{12}; P_{11} = G_{23}; P_{22} = G_{12} \quad (4.69)$$

The stress moment and shear resultant forces can be written as (Tran et al., 2016)

$$\begin{Bmatrix} \mathbf{N} \\ \mathbf{M} \\ \mathbf{P} \\ \mathbf{R} \end{Bmatrix} = \begin{bmatrix} \mathbf{A} & \mathbf{B} & \mathbf{E} & \mathbf{0} \\ \mathbf{B} & \mathbf{D} & \mathbf{F} & \mathbf{0} \\ \mathbf{E} & \mathbf{F} & \mathbf{H} & \mathbf{0} \\ \mathbf{0} & \mathbf{0} & \mathbf{0} & \mathbf{D}^s \end{bmatrix} \begin{Bmatrix} \varepsilon_m \\ \varepsilon_h \\ \varepsilon_b \\ \varepsilon_\gamma \end{Bmatrix} - \begin{Bmatrix} \mathbf{N}^{\text{th}} \\ \mathbf{M}^{\text{th}} \\ \mathbf{P}^{\text{th}} \\ \mathbf{0} \end{Bmatrix} = \hat{\mathbf{D}}_u \hat{\varepsilon} - \hat{\sigma}_0 \quad (4.70)$$

The thermal stress resultants are written as (Tran et al., 2016)

$$\{\mathbf{N}^{\text{th}} \quad \mathbf{M}^{\text{th}} \quad \mathbf{P}^{\text{th}}\} = \sum_{k=1}^3 \int_{Z_k}^{Z_{k+1}} Q_{ij}^k \begin{Bmatrix} \alpha \\ \alpha \\ 0 \end{Bmatrix} \{1 \quad z \quad f(z)\} \Delta T dz \quad (4.71)$$

The plate's total energy variation is calculated using the principle of virtual displacement (Tran et al., 2016)

$$\delta \Pi = \delta U_\varepsilon - \delta V = \int_\Omega \delta \hat{\varepsilon}^T \hat{\sigma} d\Omega - \int_\Omega \delta \mathbf{q}^T f_z d\Omega = 0 \quad (4.72)$$

From equations (4.27),(4.28) and(4.29) generalised strains can be rewritten in matrix form as

$$\hat{\varepsilon} = \left(\mathbf{B}_L + \frac{1}{2} \mathbf{B}_{NL} \right) \mathbf{q}_i \quad (4.73)$$

$$\mathbf{B}_L = \mathbf{B}_m - z \mathbf{B}_h + f(z) \mathbf{B}_b + \mathbf{B}_I \quad (4.74)$$

The first variation of the strains is defined as

$$\delta \hat{\varepsilon} = (\mathbf{B}_L + \mathbf{B}_{NL}) \delta \mathbf{q}_i \quad (4.75)$$

Substituting Eqs. (4.70) and (4.75) into Eq. (4.72), the governing equation can be written in the following matrix for

$$(\mathbf{K}_L + \mathbf{K}_{NL} - \mathbf{K}_0) \mathbf{q}_i = \mathbf{F} \quad (4.76)$$

$$\mathbf{K}_G = \int_\Omega (\mathbf{B}_g)^T \begin{bmatrix} N_x & N_{xy} \\ N_{xy} & N_y \end{bmatrix} (\mathbf{B}_g) d\Omega \quad (4.77)$$

$$\mathbf{F} = \int_\Omega (\mathbf{B}_L)^T \hat{\sigma}_0 \quad (4.78)$$

The linear stiffness matrix is denoted as \mathbf{K}_L , while the non-linear stiffness matrix is denoted as \mathbf{K}_{NL} . Additionally, \mathbf{K}_0 represents the initial stiffness matrix resulting from the initial compressive force caused by temperature. The load vector, designated as \mathbf{F} , depends on the thermal load.

In contrast, the non-linear stability characteristics are studied by solving a non-linear system of equations using the iterative and incremental process, i.e., the Newton–Raphson method. The incremental form of algebraic equations (4.76) is given by:

$$\mathbf{K}_T \Delta \mathbf{q} = \Delta \mathbf{F} \quad (4.79)$$

Where

$$q_{i+1} = q_i + \Delta q$$

$$\Delta \mathbf{F} = [\mathbf{F} - (\mathbf{K}_L + \mathbf{K}_{NL}(\mathbf{q}_i) - \mathbf{K}_0)\mathbf{q}_i] \quad (4.80)$$

$$\mathbf{K}_0 = \int_{\Omega} (\mathbf{B}_g)^T \begin{bmatrix} N_{xx}^{th} & N_{xy}^{th} \\ N_{xy}^{th} & N_{yy}^{th} \end{bmatrix} (\mathbf{B}_g) d\Omega \quad (4.81)$$

The solution procedure for Eq.(4.76) is described in [Figure 4.1](#).

4.10 Non-Linear Vibration

For the free vibration analysis of the plate without external forces, the weak form can be derived from the principle of virtual work as ([Kiani, 2018](#))

$$\int_{\Omega} \delta \hat{\boldsymbol{\varepsilon}}^T \hat{\boldsymbol{\sigma}} d\Omega = \int_{\Omega} \delta \mathbf{q}^T \mathbf{M} \ddot{\mathbf{q}} d\Omega \quad (4.82)$$

The vector q in Eq. (4.83) may be expressed as

$$q = \begin{Bmatrix} q_1 \\ q_2 \\ q_3 \end{Bmatrix} \quad (4.83)$$

where the following definitions apply

$$\mathbf{q}_1 = \begin{Bmatrix} u_0 \\ v_0 \\ w_0 \end{Bmatrix}, \quad \mathbf{q}_2 = \begin{Bmatrix} w_{,x} \\ w_{,y} \\ 0 \end{Bmatrix}, \quad \mathbf{q}_3 = \begin{Bmatrix} \theta_x \\ \theta_y \\ 0 \end{Bmatrix} \quad (4.84)$$

Substitution of Eqs. (4.50) and (4.73) into the definition of motion equation (4.83) results in

$$(\mathbf{K}_L + \mathbf{K}_{NL} - \mathbf{K}_G)\mathbf{q} + \mathbf{M}\ddot{\mathbf{q}} = 0 \quad (4.85)$$

The above equation is a nonlinear eigenvalue problem.

Where

$$\begin{aligned} \mathbf{K}_L = & \int_{\Gamma_p} \mathbf{B}_m^T \mathbf{A} \mathbf{B}_m d\Gamma_p - \int_{\Gamma_p} \mathbf{B}_m^T \mathbf{B} \mathbf{B}_b d\Gamma_p + \int_{\Gamma_p} \mathbf{B}_m^T \mathbf{E} \mathbf{B}_h d\Gamma_p - \int_{\Gamma_p} \mathbf{B}_b^T \mathbf{B} \mathbf{B}_m d\Gamma_p + \int_{\Gamma_p} \mathbf{B}_b^T \mathbf{D} \mathbf{B}_b d\Gamma_p - \\ & \int_{\Gamma_p} \mathbf{B}_b^T \mathbf{F} \mathbf{B}_h d\Gamma_p + \int_{\Gamma_p} \mathbf{B}_h^T \mathbf{E} \mathbf{B}_m d\Gamma_p - \int_{\Gamma_p} \mathbf{B}_h^T \mathbf{F} \mathbf{B}_b d\Gamma_p + \int_{\Gamma_p} \mathbf{B}_h^T \mathbf{H} \mathbf{B}_h d\Gamma_p + \int_{\Gamma_p} \mathbf{B}_\gamma^T \mathbf{D}_{\alpha\beta}^s \mathbf{B}_\gamma d\Gamma_p + \mathbf{K}_I^1 \end{aligned} \quad (4.86)$$

Where \mathbf{K}_I^I Includes the additional terms in the linear stiffness matrix due to initial imperfection.

$$\begin{aligned} \mathbf{K}_{NL} = & \int_{\Gamma_p} \mathbf{B}_{nl}^T \mathbf{A} \mathbf{B}_m d\Gamma_p - \int_{\Gamma_p} \mathbf{B}_{nl}^T \mathbf{B} \mathbf{B}_b d\Gamma_p + \int_{\Gamma_p} \mathbf{B}_{nl}^T \mathbf{E} \mathbf{B}_h d\Gamma_p \\ & + 0.5 \int_{\Gamma_p} \mathbf{B}_m^T \mathbf{A} \mathbf{B}_{nl} d\Gamma_p - 0.5 \int_{\Gamma_p} \mathbf{B}_b^T \mathbf{B} \mathbf{B}_{nl} d\Gamma_p \\ & + 0.5 \int_{\Gamma_p} \mathbf{B}_h^T \mathbf{E} \mathbf{B}_{nl} d\Gamma_p + 0.5 \int_{\Gamma_p} \mathbf{B}_{nl}^T \mathbf{A} \mathbf{B}_{nl} d\Gamma_p + \mathbf{K}_I^{nl} \end{aligned} \quad (4.87)$$

Where \mathbf{K}_I^{nl} Includes the additional terms in the non-linear stiffness matrix due to initial imperfection. The M and \mathbf{K}_G matrix is already given in eq. (4.64 and 4.77)

4.11 Solution Procedure for the Non-Linear Algebraic Equations

Figure 4.3 presents a brief flowchart of the present solution procedure, in which the Newton-Raphson iterative scheme is employed to solve the nonlinear algebraic equations.

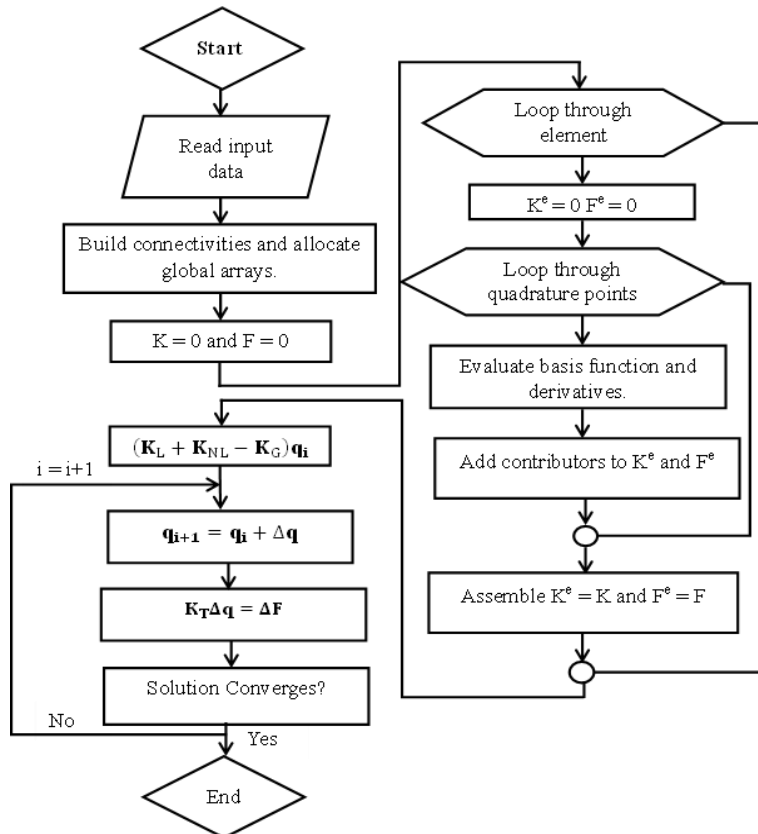


Figure 4.3: Flowchart of the nonlinear analysis method

4.11.1 Newton–Raphson Method.

Numerical analysis is a method used to find the roots of nonlinear equations. The approach involves assuming an initial estimate, q_0 , and determining its increment, Δq , so that the new estimate, $q_0 + \Delta q$, is close to the solution of Eq. (4.76). To determine the increment, linear ones locally approximate the nonlinear equations. This process is repeated until the original nonlinear equations are satisfied. If an approximate solution q_i is known at the i th iteration, the solution at the next iteration can be approximated using the first-order Taylor series. (Kim, 2015)

$$\mathbf{f}(\mathbf{q}^{i+1}) \approx \mathbf{f}(\mathbf{q}^i) + \mathbf{K}_T^i(\mathbf{q}^i) \cdot \Delta \mathbf{q}^i = \mathbf{F} \quad (4.88)$$

where $\mathbf{K}_T^i(\mathbf{q}^i)$ commonly referred to as the tangent stiffness matrix in structural applications and $\Delta \mathbf{q}^i$ represent the solution increment. The objective is to iteratively calculate $\Delta \mathbf{q}^i$ and update the solution, \mathbf{q}^{i+1} . By rearranging the terms, we can obtain a system of linearised equations represented as:

$$\mathbf{K}_T^i \Delta \mathbf{q}^i = \mathbf{F} - \mathbf{f}(\mathbf{q}^i) \quad (4.89)$$

After calculating the displacement increment, \mathbf{q}^i , a new approximate solution can be obtained using the following formula:

$$\mathbf{q}^{i+1} = \mathbf{q}^i + \Delta \mathbf{q}^i \quad (4.90)$$

The solution will not exactly satisfy the system of nonlinear equations and there will be some residual or unbalanced force, defined as follows:

$$\mathbf{R}^{i+1} = \mathbf{F} - \mathbf{f}(\mathbf{q}^{i+1}) \quad (4.91)$$

When solving a problem with numerical methods, it is important to ensure that the solution is accurate. One way to do this is by checking the residual, which is the difference between the calculated and actual solutions. If the residual is smaller than a certain tolerance level, then the calculated solution can be accepted as accurate and the process stops. However, if the residual is still too large, then the process is repeated until the residual becomes very small. The termination criterion is expressed in a normalised form as shown below:

$$\text{conv} = \frac{\sum_{j=1}^n (R_j^{i+1})^2}{1 + \sum_{j=1}^n (f_j)^2}$$

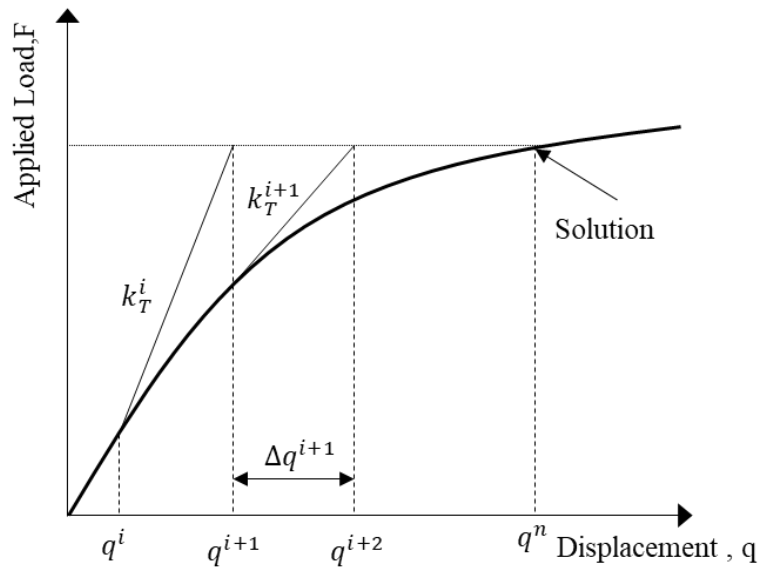


Figure 4.4: Conventional Newton-Raphson Method

The general procedures of the Newton-Raphson Method can be summarised in Figure 4.4. The Newton-Raphson method updates the tangent stiffness matrix of the structure at every iteration. In contrast, the modified Newton-Raphson method reforms it only in the first iteration and keeps it unchanged within the load cycle. Both methods offer a high convergence rate in the stable equilibrium range. However, as the limit point of the load-deflection curve is approached, numerous iterations may be needed even for a small load increment. In the Newton-Raphson method, the solution point at the specified applied load level is taken, making it impossible to trace any unloading path. This leads to a divergence in the solution scheme near the critical point due to the tangent stiffness matrix's the load increment's size exceeding the limit load, as demonstrated above.

4.11.2 Force Control Method

The incremental force method involves applying the load in increments as shown in Figure 4.5. Within each load increment, the standard Newton-Raphson method is used. The next load increment is applied once the solution corresponding to the previous load increment has converged. The converged solution at each increment is then used to estimate the next increment. To ensure a quick convergence to the solution, the magnitude of the increment, ΔF_2 , is chosen carefully. This process is repeated until the applied load increment reaches

its full magnitude. It's important to note that the solutions at the end of each load increment are all valid responses of the system at the given load level.

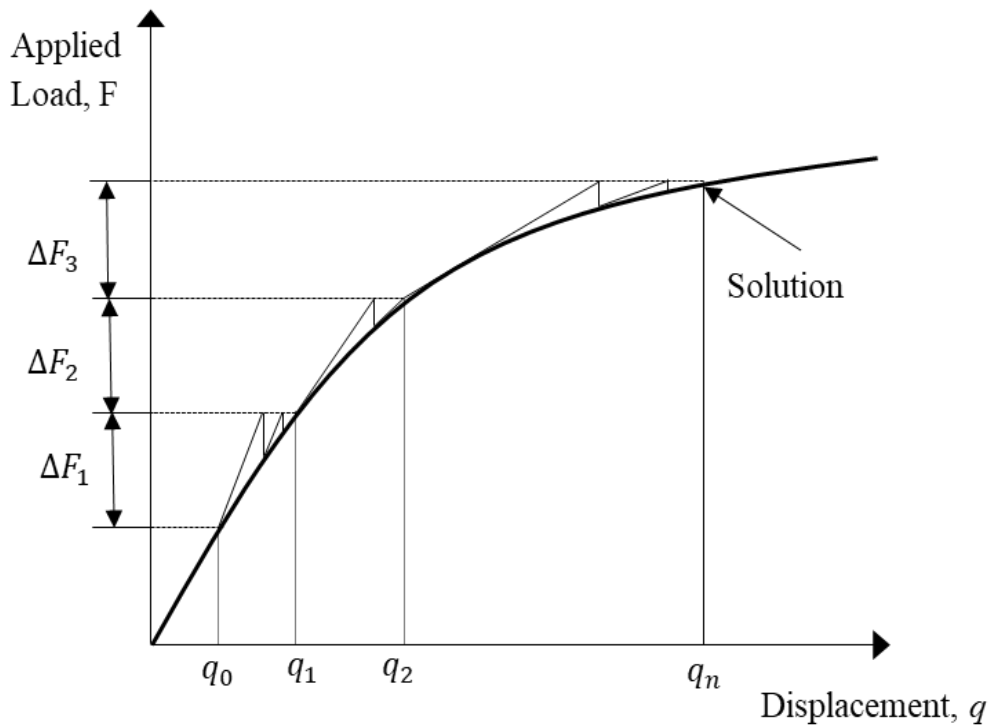


Figure 4.5: Force control method

4.11.3 Displacement Control Method

In contrast to prior load control techniques, this approach introduces a displacement constraint equation. The displacement control method was first suggested by [Argyris \(1965\)](#). However, the addition of the displacement constraint equation in his study compromised the symmetry of the tangent stiffness matrix. To preserve the symmetry of the tangent stiffness matrix, [Batoz & Dhatt \(1979\)](#) implemented an iterative approach to enforce the displacement constraint. As per their method, a solitary [Figure 4.6](#) illustrates the procedural diagram. While the constant displacement method smoothly passes the snap-through limit point, it struggles to converge in snap-back problems. As a result, it is typically employed alongside other solution techniques to address general non-linear problems

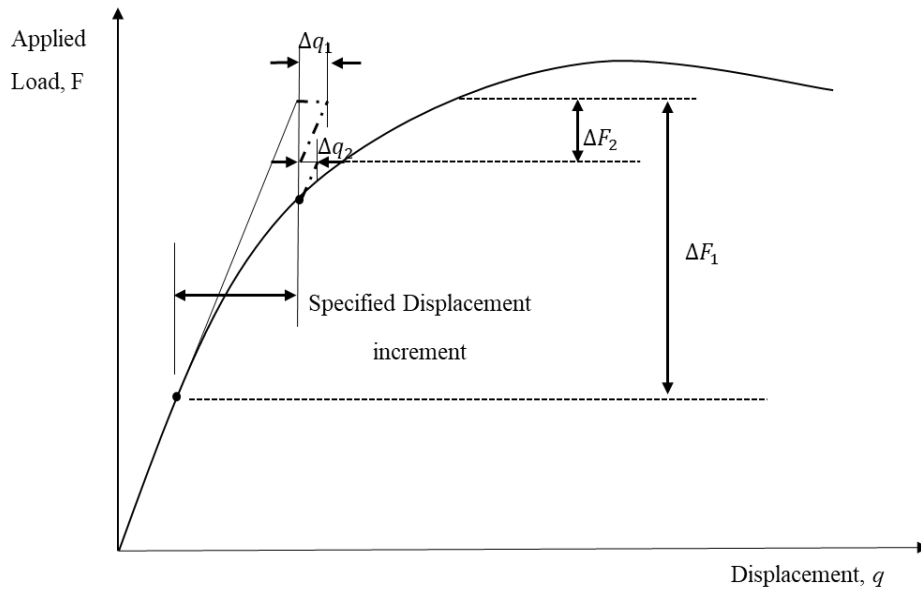


Figure 4.6: Displacement Control Method

4.11.4 Arc Length Method

Several methods of the arc-length technique have been proposed by various researchers in the past, including [Wempner \(1971\)](#), [Riks \(1979\)](#), [Ramm \(1981\)](#) for non-linear analysis. However,. The fundamental principle of the spherical arc-length method involves constraining the load increment to maintain a constant dot product of displacement along the iteration path in the 2-dimensional plane of load versus deformation. It is worth noting that the load increment sign will depend on the determinant of the updated tangent stiffness matrix. In simpler terms, a positive determinant will increase loading, while a negative determinant will decrease load. This idea of choosing the sign was first introduced by [Bergan \(1978\)](#) in their research on the method of the current stiffness parameter. The process of the spherical arc-length method is depicted in [Figure 4.7](#). Due to its high accuracy, reliability, and satisfactory convergence rate, it is considered the most widely used method for non-linear analysis. Additionally, it has been noted for its robustness and stability in pre- and post-buckling analysis.

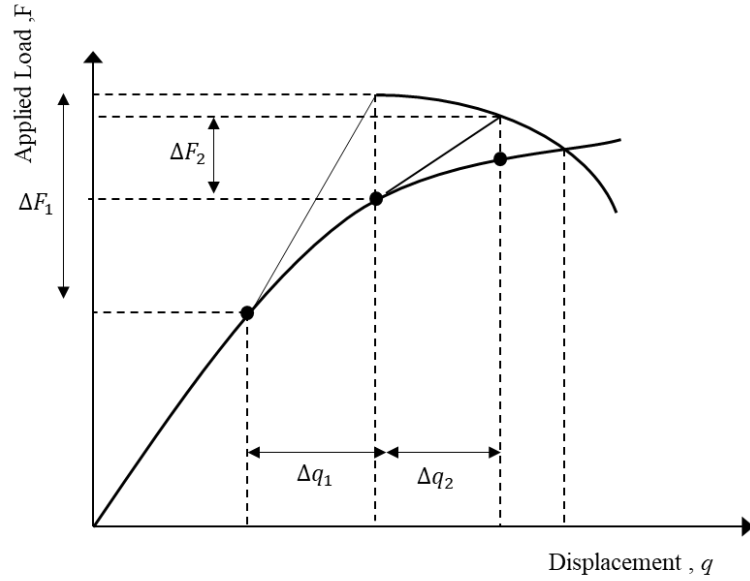


Figure 4.7: Arc length method

4.12 Mapping Technique in IGA

The physical space, parametric space, and parent space (element) for integration in IGA are shown in Figure 4.8. As mentioned before, the same basis functions are utilised for both geometric construction and discretisation of unknown field variables, given as

$$\mathbf{x} = \sum_{i=1}^{n \times m} \varphi_i(\xi, \eta) x_i, \quad \bar{\mathbf{q}} = \sum_{i=1}^{n \times m} \varphi_i(\xi, \eta) q_i \quad (4.92)$$

where \mathbf{x} and $\bar{\mathbf{q}}$ correspond to the physical coordinate vector of geometry and unknown field variable vector, respectively;

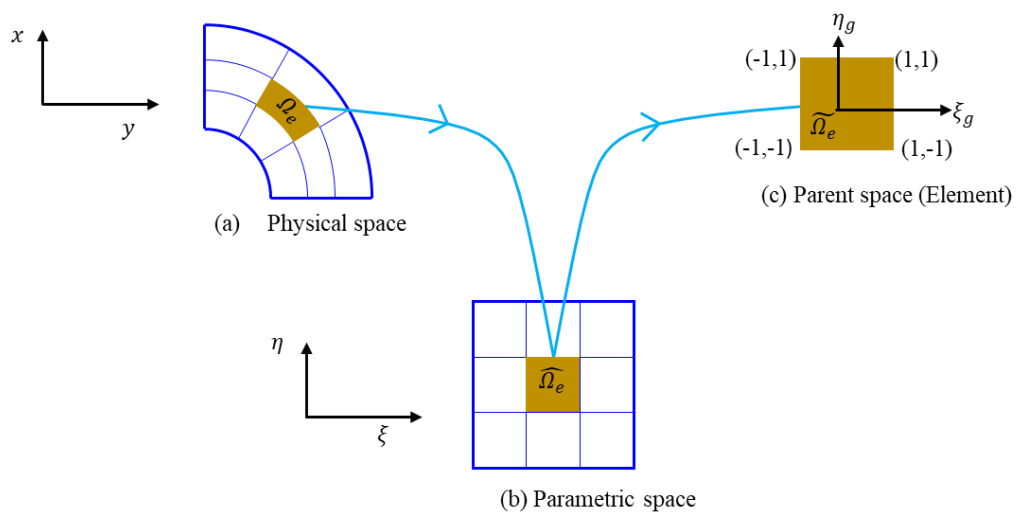


Figure 4.8: Mapping technique in isogeometric analysis.

This part provides information on the first and second derivatives of NURBS basis functions in relation to physical coordinate variables. Applying the chain rule makes it possible to calculate the first and second derivatives of the basis functions with respect to physical coordinates (x, y) .

$$\begin{Bmatrix} \frac{\partial \varphi_i}{\partial \xi} \\ \frac{\partial \varphi_i}{\partial \eta} \end{Bmatrix} = \begin{bmatrix} \frac{\partial x}{\partial \xi} & \frac{\partial y}{\partial \xi} \\ \frac{\partial x}{\partial \eta} & \frac{\partial y}{\partial \eta} \end{bmatrix} \begin{Bmatrix} \frac{\partial \varphi_i}{\partial x} \\ \frac{\partial \varphi_i}{\partial y} \end{Bmatrix} \rightarrow \begin{Bmatrix} \frac{\partial \varphi_i}{\partial x} \\ \frac{\partial \varphi_i}{\partial y} \end{Bmatrix} = [\mathbf{J}_{\xi\eta}]^{-1} \begin{Bmatrix} \frac{\partial \varphi_i}{\partial \xi} \\ \frac{\partial \varphi_i}{\partial \eta} \end{Bmatrix} \quad (4.93)$$

$$[\mathbf{J}_{\xi\eta}] = \begin{bmatrix} \frac{\partial x}{\partial \xi} & \frac{\partial y}{\partial \xi} \\ \frac{\partial x}{\partial \eta} & \frac{\partial y}{\partial \eta} \end{bmatrix} \quad (4.94)$$

where $\mathbf{J}_{\xi\eta}^{-1}$ indicates the inverse of the Jacobian matrix. Starting from Eq. (4.93), the second-order derivatives concerning the parametric coordinates ξ and η in the extended form can be evaluated as

$$\begin{Bmatrix} \frac{\partial^2 \varphi_i}{\partial \xi^2} \\ \frac{\partial^2 \varphi_i}{\partial \eta^2} \\ \frac{\partial^2 \varphi_i}{\partial \xi \partial \eta} \end{Bmatrix} = \begin{bmatrix} \left(\frac{\partial x}{\partial \xi}\right)^2 & \left(\frac{\partial y}{\partial \xi}\right)^2 & 2\left(\frac{\partial x}{\partial \xi}\right)\left(\frac{\partial y}{\partial \xi}\right) \\ \left(\frac{\partial x}{\partial \eta}\right)^2 & \left(\frac{\partial y}{\partial \eta}\right)^2 & 2\left(\frac{\partial x}{\partial \eta}\right)\left(\frac{\partial y}{\partial \eta}\right) \\ \left(\frac{\partial x}{\partial \xi}\right)\left(\frac{\partial x}{\partial \eta}\right) & \left(\frac{\partial y}{\partial \xi}\right)\left(\frac{\partial y}{\partial \eta}\right) & \left(\frac{\partial x}{\partial \xi}\right)\left(\frac{\partial y}{\partial \eta}\right) + \left(\frac{\partial x}{\partial \eta}\right)\left(\frac{\partial y}{\partial \xi}\right) \end{bmatrix} \begin{Bmatrix} \frac{\partial^2 \varphi_i}{\partial x^2} \\ \frac{\partial^2 \varphi_i}{\partial y^2} \\ \frac{\partial^2 \varphi_i}{\partial x \partial y} \end{Bmatrix} \quad (4.95)$$

$$+ \begin{bmatrix} \frac{\partial^2 x}{\partial \xi^2} & \frac{\partial^2 y}{\partial \xi^2} \\ \frac{\partial^2 x}{\partial \eta^2} & \frac{\partial^2 y}{\partial \eta^2} \\ \frac{\partial^2 x}{\partial \xi \partial \eta} & \frac{\partial^2 y}{\partial \xi \partial \eta} \end{bmatrix} \begin{Bmatrix} \frac{\partial \varphi_i}{\partial x} \\ \frac{\partial \varphi_i}{\partial y} \end{Bmatrix} \rightarrow \begin{Bmatrix} \frac{\partial^2 \varphi_i}{\partial x^2} \\ \frac{\partial^2 \varphi_i}{\partial y^2} \\ \frac{\partial^2 \varphi_i}{\partial x \partial y} \end{Bmatrix} = [\mathbf{J}_{\xi\eta}^{33}]^{-1} \left(\begin{Bmatrix} \frac{\partial^2 \varphi_i}{\partial \xi^2} \\ \frac{\partial^2 \varphi_i}{\partial \eta^2} \\ \frac{\partial^2 \varphi_i}{\partial \xi \partial \eta} \end{Bmatrix} - [\mathbf{J}_{\xi\eta}^{32}] \begin{Bmatrix} \frac{\partial \varphi_i}{\partial x} \\ \frac{\partial \varphi_i}{\partial y} \end{Bmatrix} \right)$$

$$[\mathbf{J}_{\xi\eta}^{33}] = \begin{bmatrix} \left(\frac{\partial x}{\partial \xi}\right)^2 & \left(\frac{\partial y}{\partial \xi}\right)^2 & 2\left(\frac{\partial x}{\partial \xi}\right)\left(\frac{\partial y}{\partial \xi}\right) \\ \left(\frac{\partial x}{\partial \eta}\right)^2 & \left(\frac{\partial y}{\partial \eta}\right)^2 & 2\left(\frac{\partial x}{\partial \eta}\right)\left(\frac{\partial y}{\partial \eta}\right) \\ \left(\frac{\partial x}{\partial \xi}\right)\left(\frac{\partial x}{\partial \eta}\right) & \left(\frac{\partial y}{\partial \xi}\right)\left(\frac{\partial y}{\partial \eta}\right) & \left(\frac{\partial x}{\partial \xi}\right)\left(\frac{\partial y}{\partial \eta}\right) + \left(\frac{\partial x}{\partial \eta}\right)\left(\frac{\partial y}{\partial \xi}\right) \end{bmatrix} \quad (4.96)$$

It should be noted that the numerical integration utilised in IGA is similar to that of FEM, utilising the Gauss-Legendre quadrature. However, IGA's implementation is more intricate, dividing the integral of the entire physical system into integrals over each physical element.

This approach results in a superior level of accuracy and is a distinguishing feature of IGA in comparison to FEM.

The integral is first pulled back to the parametric element for integration over each physical element using geometry mapping. Next, the integrals over the parametric element are further pulled back to the parent domain. This is where existing integration rules are usually defined. The mapping $\tilde{\Omega}_e \rightarrow \hat{\Omega}_e$ from the parent domain $[-1,1] \times [-1,1]$ to the parametric domain $[\xi_i, \xi_{i+1}] \times [\eta_i, \eta_{i+1}]$ is given by (Tran, 2016)

$$\xi = \frac{1}{2}[(\xi_{i+1} - \xi_i)\xi_g + (\xi_{i+1} + \xi_i)] \quad (4.97)$$

$$\eta = \frac{1}{2}[(\eta_{j+1} - \eta_j)\eta_g + (\eta_{j+1} + \eta_j)] \quad (4.98)$$

Therefore, the Jacobian of this transformation is defined as:

$$|\mathbf{J}_g| = \frac{1}{4}(\xi_{i+1} - \xi_i)(\eta_{j+1} - \eta_j) \quad (4.99)$$

Now, the function $f(x, y)$ can be integrated over an element in the physical domain (Ω_e) as follows (Tran, 2016)

$$\begin{aligned} \int_{\Omega} f(x, y) d\Omega &= \sum_{e=1}^n \int_{\Omega_e} f(x, y) d\Omega_e \\ &= \sum_{e=1}^n \int_{\hat{\Omega}_e} f(\xi, \eta) |\mathbf{J}| |\mathbf{J}_{g_e}| d\tilde{\Omega}_e \\ &= \sum_{e=1}^n \sum_i^{n_{\text{cop}}} \sum_j^{m_{\text{cop}}} f(\xi_i, \eta_j) |\mathbf{J}| |\mathbf{J}_{g_e}| W_i W_j \end{aligned} \quad (4.100)$$

where (ξ_i, η_i) are the Gaussian points and W_i, W_j are the weighting coefficients, which are introduced in Table 4.1

Table 4.1: Gauss points and weights in the Gauss-Legendre numerical integration

Gauss Point	Integration point	Weight
1	0.0000000000000000	2.0000000000000000
2	± 0.577350269189625	1.0000000000000000
3	0.0000000000000000	0.8888888888888888
	± 0.774596669241483	0.5555555555555555
4	± 0.339981043584856	0.652145154862546
	± 0.861136311594052	0.347854845137453
5	0.0000000000000000	0.5688888888888888
	± 0.538469310105683	0.478628670499366
	± 0.906179845938664	0.236926885056189
6	± 0.238619186083196	0.467913934572691
	± 0.661209386466264	0.360761573048138
	± 0.932469514203152	0.171324492379170
7	0.0000000000000000	0.417959183673469
	± 0.405845151377397	0.381830050505118
	± 0.741531185599394	0.279705391489276
	± 0.949107912342758	0.129484966168869

4.13 Oblique Boundary Transformation for Skew Plate

As the displacement fields of the skew plate are defined in an oblique coordinate system, it is necessary to transform the displacement variables from the orthogonal coordinate system (x, y) to the local oblique coordinate system (x', y') as shown in Figure 4.9. This

involves considering the relationship between axial displacements and rotations in the local coordinate system $\{q_i^L\}$ and the global coordinate system $\{q_i\}$, which can be represented in matrix form as follows

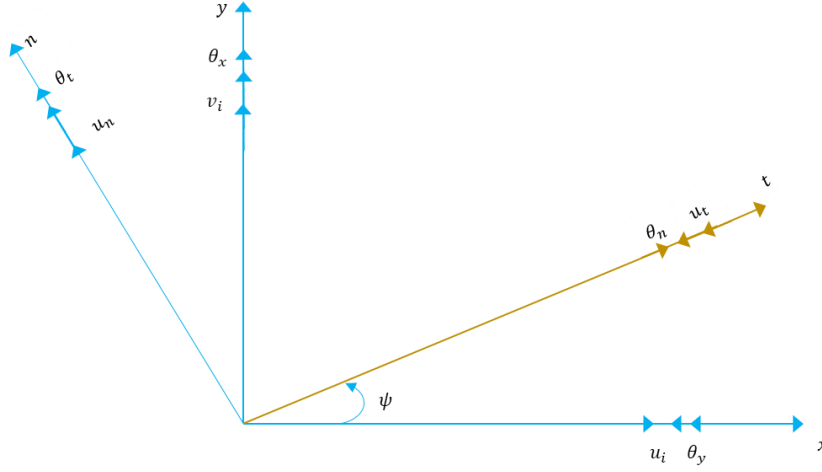


Figure 4.9: The coordinate system and displacement field variables of the skew sandwich plate

Where

$$\begin{bmatrix} u_i \\ v_i \\ w_i \\ \theta_{xi} \\ \theta_{yi} \end{bmatrix}_G = \mathbf{T}_m \begin{bmatrix} u_t \\ u_n \\ w_i \\ \theta_t \\ \theta_n \end{bmatrix}_L \quad (4.101)$$

$$\{q_i\} = [T_m]\{q_i^L\} \quad (4.102)$$

$$\mathbf{T}_m = \begin{bmatrix} T & \dots & \dots & \dots & \dots \\ \dots & T & \dots & \dots & \dots \\ \dots & \dots & T & \dots & \dots \\ \dots & \dots & \dots & T & \dots \\ \dots & \dots & \dots & \dots & T \end{bmatrix} \quad (4.103)$$

$$\mathbf{T} = \begin{bmatrix} \cos \psi & -\sin \psi & 0 & 0 & 0 \\ \sin \psi & \cos \psi & 0 & 0 & 0 \\ 0 & 0 & 1 & 0 & 0 \\ 0 & 0 & 0 & \cos \psi & -\sin \psi \\ 0 & 0 & 0 & \sin \psi & \cos \psi \end{bmatrix} \quad (4.104)$$

4.14 Boundary Conditions

As in finite element analysis, there are two types of boundary conditions: Dirichlet and Neumann. Boundary conditions imposed on primary unknown variables (Ex, deformation, temperature, etc.) are known as Dirichlet boundary conditions. Neumann boundary conditions are imposed on the derivative of the primary variable (Ex, slope, heat flux, etc.). The form $u = 0$ boundary conditions are called homogeneous Dirichlet boundary conditions, where u can be any primary variable. These conditions are enforced by assigning the corresponding control variables as zeros. Boundary conditions of the form $u = u_1$ are called non-homogeneous Dirichlet boundary conditions. These conditions can also be imposed by setting the corresponding control variables as u_1 . Assuming open uniform knot vectors, both Dirichlet boundary conditions can be satisfied if control variables are at free end or corner points due to the Kronecker delta property. If the Dirichlet boundary conditions are to be imposed at any other point (other than endpoints) of the domain, special techniques are used in that case: penalty, Lagrange multiplier, and least squares minimisation. An alternative way is to use h-refinement over the domain boundary over which the Dirichlet boundary condition is to be imposed. This method is simple to implement but sometimes results in minor errors because boundary conditions are partially satisfied. The imposition of the Neumann boundary condition in IGA is the same as in FEA. These conditions are naturally satisfied in the weak form.

4.15 Summary

In the present work, a non-polynomial higher-order theory of plates is employed for conducting both linear and non-linear analyses of sandwich plates. This chapter introduces a non-uniform rational B-spline (NURBS) based isogeometric analysis (IGA), structural modelling and constitutive relations for isotropic and composite plates. The governing equations, discretisation technique, and solution procedure for analysing sandwich plates are also presented. Two-way mapping between physical domain and parametric space as well as parametric space and master element that is used in isogeometric analysis for numerical integration is also described. The chapter also discusses various methods for tracing load-displacement paths in structural mechanics problems. Chapter 5 uses the arc length method to trace the nonlinear path, while chapters 6 and 7 employ force control and displacement control strategies, followed by boundary conditions.

Stability Analysis of Sandwich Plates under Non-uniform Mechanical Loading

5.1 Introduction

Chapter 4 presents the governing equations, discretisation technique, and solution procedure for analysing sandwich plates. This chapter delves into using non-polynomial theory with isogeometric analysis (IGA) to perform stability analysis for sandwich plates featuring FGCNTRC face sheets and metal foam core. The accuracy of the developed in-house MATLAB code is investigated for both linear and non-linear stability behaviour of sandwich plates with different boundary conditions. Section 5.2 details the geometry and material properties of the sandwich plates, while Section 5.3 explores the linear buckling behaviour of isotropic and sandwich plates under varying loading and boundary conditions. Section 5.4 compares results for the non-linear post-buckling analysis of isotropic plates and presents new results on the non-linear post-buckling behaviour of skew sandwich plates. Through-thickness displacements are discussed in Section 5.5, and Section 5.6 summarises the important contributions of this chapter. The non-linear stability of skew sandwich plates under non-uniform mechanical loadings is a complex area of study. Our research aims to investigate the buckling, post-buckling, and post-buckled vibration behaviour of initial imperfect sandwich plates with a metal foam core (square, skew) under various mechanical loadings (uniform, parabolic, sinusoidal, triangular, and concentrated) and different boundary conditions (simply supported and clamped).

5.2 Geometry and Material Properties

The geometry of the skew plate is described in [Figure 5.1](#). The face sheets are nanocomposites made up of CNTs and polymethyl methacrylate (PMMA) matrix. The elastic constants of the constituents are given in [Table 5.1](#). The distribution of CNTs in the face sheets influences the effective material properties. The three types of CNT distributions through the face sheets' thickness, uniform distribution (UD), FGX and FGO, are shown in [Figure 5.2](#). The functions

corresponding to the graded distributions of CNTs are given in [Table 5.2](#). The total volume fraction of CNTs in all three cases is assumed to be the same.

Table 5.1: Material properties for the various cases considered in the present study.

Cellular Aluminium (Thang et al., 2018)	Cellular Aluminium: $G_1=26.923$ GPa, $\nu = 0.3$, $E_1 = 2G_1(1+\nu)$, $\rho = 2707$ kg/m ³
FGCNTRC Plate (Wang & Shen, 2012)	CNTs: $E_{11}=5.4466$ TPa, $E_{22}=7.08$ TPa, $G_{12}=1.9445$ TPa, $G_{13} = G_{12}$, $G_{23}=1.2G_{12}$, $\nu_{12} = 0.175$, $\rho = 1400$ kg/m ³ PMMA: $E_m = 2.5$ GPa, $\nu_m = 0.3$, $\rho_m = 1150$ kg/m ³
Three-layered Sandwich Plate	Face Sheets: FGCNTRCs CNTs: $E_{11}=5.4466$ TPa, $E_{22}=7.08$ TPa, $G_{12}=1.9445$ TPa, $G_{13} = G_{12}$, $G_{23}=1.2G_{12}$, $\nu_{12} = 0.175$, $\rho = 1400$ kg/m ³ PMMA: $E_m = 2.5$ GPa, $\nu_m = 0.34$, $\rho_m = 1150$ kg/m ³ Core Layer: Cellular Aluminium, $G_1=26.923$ GPa, $\nu = 0.3$, $E_1 = 2G_1(1+\nu)$, $\rho = 2707$ kg/m ³

Table 5.2: Volume fraction function of CNTs for different distributions

CNTs Distribution Type	Volume Fraction of CNTs in Face Sheets
UD.	V_{CN}^*
F.G.X.	$\frac{4}{h_t - h_b} \left(\left \frac{h_t + h_b}{2} - z \right \right) V_{CN}^*$
F.G.O.	$\frac{4}{h_t - h_b} \left(\frac{h_t - h_b}{2} - \left \frac{h_t + h_b}{2} - z \right \right) V_{CN}^*$

In [Table 5.2](#) h_t and h_b are the z coordinates of the end positions of face sheets. The properties of the CNTs and PMMA at room temperature (300 K) ([Wang & Shen, 2012](#)) and are given in [Table 5.1](#). The extended rule of mixtures with efficiency parameters is used to evaluate the effective material properties of the face sheets, which are given by:

$$E_{11} = \eta_1 V_{CN} E_{11}^{CN} + V_m E_m \quad (5.1)$$

$$\eta_2 / E_{22} = V_{CN} / E_{22}^{CN} + V_m / E_m \quad (5.2)$$

$$\eta_3 / G_{12} = V_{CN} / G_{12}^{CN} + V_m / G_m \quad (5.3)$$

$$\nu_{12} = V_{CN}^* \nu_{12}^{CN} + V_m \nu_m \quad (5.4)$$

E_{11}^{CN} , E_{22}^{CN} , G_{12}^{CN} and ν_{12}^{CN} are in-plane Young's moduli, shear moduli and Poisson's ratio of CNTs, respectively. E_m , G_m and ν_m are the Young's moduli, shear moduli and Poisson's ratio for the PMMA matrix. V_{CN} and V_m are the volume fractions of CNT and the matrix, respectively. The material properties of the resultant FGCNTRC are assumed to be scale dependent. The scale dependency of material properties is incorporated by determining the efficiency parameters. The efficiency parameters (η_1, η_2, η_3) (Jiang et al., 2014) considered in the present investigation are given in Table 5.3. The aluminium foam core layer is isotropic, and two types (uniform, non-uniform symmetric) of porosity distribution are assumed to investigate the influence of porosity, as shown in Figure 5.3. The corresponding porosity functions are listed in Table 5.4. where E_0 and G_0 are the maximum values of Young's and shear moduli, respectively. The amount of porosity is controlled by introducing the coefficient of porosity (e_0). h_c is the thickness of the core layer.

Table 5.3: Efficiency parameters for the FGCNTRC (Wang & Shen, 2012)

Volume Fraction (V_{CN}^*)	Efficiency Parameters
0.12	$\eta_1 = 0.137, \eta_2 = 1.022, \eta_3 = 0.7\eta_2$
0.17	$\eta_1 = 0.142, \eta_2 = 1.626, \eta_3 = 0.7\eta_2$
0.28	$\eta_1 = 0.141, \eta_2 = 1.585, \eta_3 = 0.7\eta_2$

Table 5.4: Porosity distribution functions

Porosity Distribution Type	Material Properties
	$E(z) = E_0(1 - e_0\Lambda)$
	$G(z) = G_0(1 - e_0\Lambda)$
Uniform Porosity Distribution (UPD)	where
	$\Lambda = \frac{1}{e_0} - \frac{1}{e_0} \left(\frac{2}{\pi} \sqrt{1 - e_0} - \frac{2}{\pi} + 1 \right)^2$
Symmetric Porosity Distribution (SPD)	$E(z) = E_0 \left(1 - e_0 \cos \left(\frac{\pi z}{h_c} \right) \right)$
	$G(z) = G_0 \left(1 - e_0 \cos \left(\frac{\pi z}{h_c} \right) \right)$

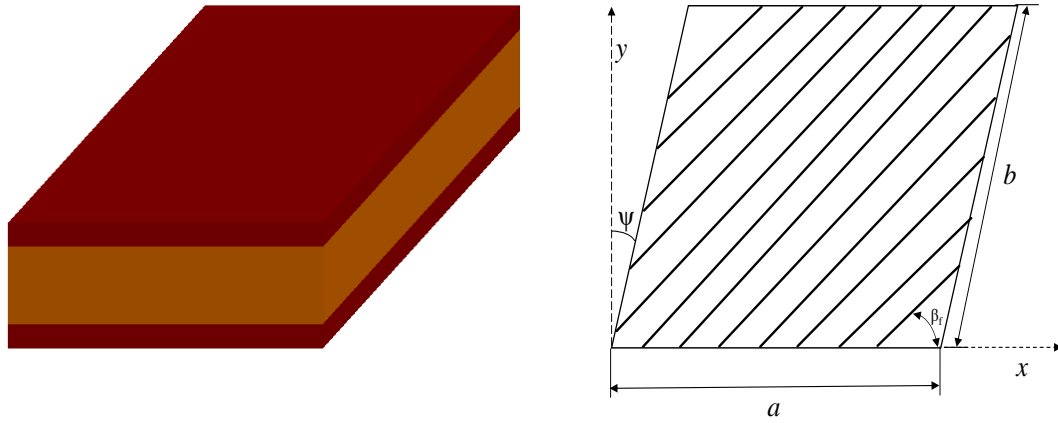


Figure 5.1: Geometrical parameters for the sandwich skew plate

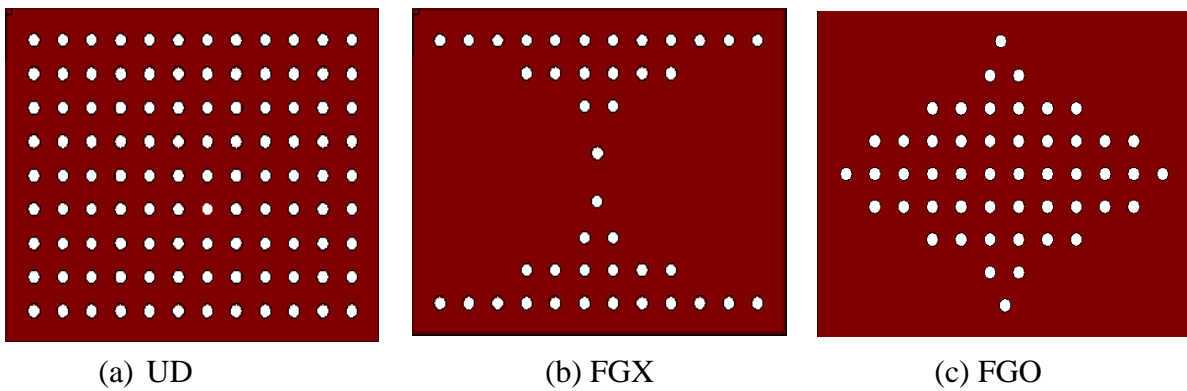
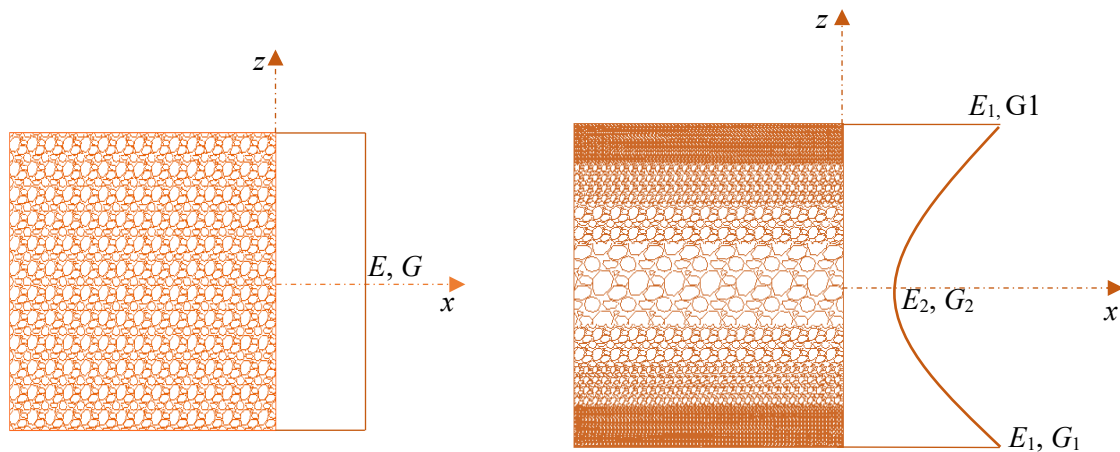


Figure 5.2: Various types of CNT pattern distributions in the top and bottom face sheets



(a) Uniform Porosity Distribution (U.P.D.) (b) Symmetric Porosity Distribution (S.P.D)

Figure 5.3. Types of porosity function through the thickness of the core

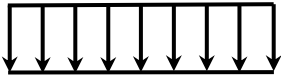
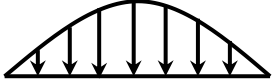
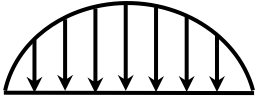

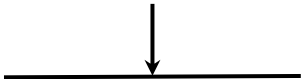
Load Diagram	Load type	Load equation
	Uniform	$F_u = q_0$
	Parabolic	$F_p = 6q_0 \frac{y}{b_1} \left(1 - \frac{y}{b_1}\right)$
	Sinusoidal	$F_s = \frac{q_0\pi}{2} \sin \frac{\pi y}{b_1}$
	Triangular	$F_t = \begin{cases} 4q_0 \frac{y}{b_1} & 0 \leq y \leq \frac{b_1}{2} \\ 4q_0 \left(1 - \frac{y}{b_1}\right) & \frac{b_1}{2} \leq y \leq b_1 \end{cases}$
	Concentrated	$F_c = q_0 b_1$ At $y = \frac{b_1}{2}$

Figure 5.4: Functions for arbitrary compressive loads ($b_1 = b \cos \psi$)

5.2.1 Boundary Conditions

The following boundary conditions are considered in the present analysis:

Simply supported (SSSS) At all edges: $u_n = u_t = w_0 = 0$

Clamped (CCCC) At all edges: $u_n = u_t = w_0 = \theta_n = \theta_t = 0$

where u_t and u_n denote displacements along tangential and normal directions to the edge, whereas θ_n and θ_t represent the rotation of the mid-plane about the axis tangential and normal to the edge, respectively. w_0 is the transverse deflection of the mid-plane of the plate.

5.3 Linear Buckling Analysis

This section presents the linear buckling analysis of isotropic and sandwich plates subjected to non-uniform mechanical load. Convergence studies and new results on linear buckling analysis of isotropic, single-layered and FGCNTRC skew plates are presented in Section 5.3.1 and results for sandwich plates with various types of support conditions and skew angles are discussed in Section 5.3.2.

5.3.1 Isotropic Plates

A validation study is performed first to confirm the accuracy of the code. The linear buckling loads for SSSS isotropic skew plate subjected to uniform edge compression are obtained for different skew angles. The values obtained are compared with the results given by Babu and Kant (Babu & Kant, 1999) were obtained using FEM with FSDT and HSDT in Table 5.5 while present work based on IGA with refined higher order theory and are found to be in good agreement. The convergence study is performed for two different orders of the B-spline curve, $p = 2$ and $p = 3$, and it has been observed that when the order is higher, the results converge faster and require a lesser number of knot insertions.

Table 5.5: Convergence study of linear buckling load parameters for SSSS thin ($a/h = 1000$) isotropic skew plate subjected to uniform compression ($N_{cr}a^2/\pi^2D$), $D = Eh^3/12(1 - \nu^2)$

Order, p	nk	NCP	Skew angle (ψ)				
			0°	15°	30°	45°	
2	8	11×11	4.0196	4.4356	6.1191	11.6062	
	10	13×13	4.0144	4.4255	6.0745	11.2882	
	12	15×15	4.0117	4.4203	6.0515	11.1126	
	14	17×17	4.0102	4.4173	6.0381	11.0056	
	16	19×19	4.0093	4.4155	6.0295	10.9357	
	18	21×21	4.0086	4.4142	6.0237	10.8875	
	20	23×23	4.0080	4.4133	6.0197	10.8529	
	22	25×25	4.0078	4.4127	6.0166	10.8271	
			Babu & Kant (1999)	4.00	4.40	5.92	10.23
3	7	11×11	4.0001	4.3957	5.9264	10.3358	
	9	13×13	4.0000	4.3955	5.9233	10.2957	
	11	15×15	4.0000	4.3954	5.9214	10.2792	
	13	17×17	4.0000	4.3953	5.9201	10.2688	
	15	19×19	4.0000	4.3952	5.9190	10.2611	
	17	21×21	4.0000	4.3952	5.9182	10.2549	
	19	23×23	4.0000	4.3951	5.9175	10.2499	
			Babu & Kant (1999)	4.00	4.40	5.92	10.23

Table 5.6: Linear buckling loads for single-layered porous aluminium skew plate subjected to uniform edge loads $\left(\frac{P_{cr}a^2}{E_1h^3}, \frac{a}{h} = 50\right)$

Boundary Condition	Skew angle, ψ	UPD			SPD		
		$e_0 = 0.1$	$e_0 = 0.3$	$e_0 = 0.5$	$e_0 = 0.1$	$e_0 = 0.3$	$e_0 = 0.5$
SSSS	0°	3.3752	2.8959	2.3873	3.4761	3.2141	2.9517
	15°	3.7077	3.1812	2.6225	3.8185	3.5306	3.2422
	30°	4.9832	4.2755	3.5246	5.1318	4.7441	4.3557
	45°	8.5629	7.3469	6.0566	8.8163	8.1454	7.4718
CCCC	0°	8.4508	7.2507	5.9773	8.7011	8.0396	7.3751
	15°	9.0821	7.7923	6.4238	9.3508	8.6391	7.9239
	30°	11.3219	9.7140	8.0080	11.6554	10.7647	9.8683
	45°	16.7526	14.3735	11.8492	17.2408	15.9102	14.5664

Therefore, order, $p = 3$ is used for approximation for all the subsequent studies. For $p = 3$, the results converged for 19-knot insertions, and thus, the same knot insertions are used for all further investigations. It can be seen from Table 5.5 that the linear buckling load parameter increases with an increasing skew angle due to an increase in the stiffness of the plate.

Table 5.6 presents the linear buckling loads for a single-layered cellular aluminium skew plate under uniform compression for different skew angles, boundary conditions and porosity distributions. The critical load decreases with the increase in porosity coefficient because the effective modulus decreases as the porosity coefficient is increased. The buckling load increases with the skew angle for a particular boundary condition. Moreover, the buckling load is higher for a CCCC than an SSSS plate as the plate is more constrained under clamped conditions, and consequently, higher stiffness is offered. The buckling load is also found to be higher for the non-uniform SPD than the uniform porosity distribution because the symmetric porosity distribution reduces the stiffness of the plate by a smaller amount than the uniform porosity distribution. The linear buckling loads for an FGCNTRC skew plate under two different types of edge compression (*Parabolic Load*: $F = \frac{4q_0y}{b_1} \left(1 - \frac{y}{b_1}\right)$, $b_1 = b \cos \psi$) are presented in Table 5.7 for different skew angles and boundary conditions. It should be noted that the function of the parabolic edge load used for the validation study in Table 5.7 is different from that described in Figure 5.4, which is used in all the other investigations.

5.3.2 Sandwich Plate with Various Support Conditions

Table 5.7: Linear buckling loads for FGCNTRC plate subjected to uniaxial edge loads $(N_{cr}a^2/\pi^2D_m), D_m = E_m h^3/12(1 - \nu^2), \frac{a}{h} = 50, V_{CN}^* = 0.17)$

Boundary Condition	Skew angle (ψ)	Uniform Load			Parabolic Load		
		UD	FGX	FGO	UD	FGX	FGO
SSSS	(Kiani (2017))	-	-	-	59.1758	84.3354	33.2042
	0°	51.6034	73.2386	29.3230	59.1645	83.7756	33.7371
	15°	52.8781	74.6711	30.4554	60.7305	85.5804	35.0908
	30°	58.2350	80.7457	35.1194	67.2147	93.0473	40.6476
	45°	75.9021	101.1506	49.9002	88.3829	117.6155	58.3026
CCCC	(Kiani (2017))	-	-	-	192.5509	264.7015	110.7794
	0°	177.4228	244.1586	101.8428	194.4289	266.9257	112.0621
	15°	180.0280	247.0183	104.1976	197.5852	270.5128	114.7881
	30°	190.6830	258.8288	113.5791	210.1730	284.7865	125.5588
	45°	223.0980	295.3898	140.6409	247.6384	327.4383	156.5064

The results are also compared with those obtained by Kiani (Kiani, 2017) using the Ritz method and Airy stress function formulation with FSDT for the case of parabolic loading, while present work based on IGA with refined higher order theory and the results are in excellent agreement. It is observed that the buckling loads are higher for the FGX distribution and least for the FGO distribution for a particular skew angle and boundary condition. This indicates that the stiffness of the plate is higher when the CNTs are distributed more towards the plate's surfaces than to the centre. The effect of the type of edge compression on linear buckling load for sandwich skew plates is studied in Table 5.8. The material properties of the constituents are tabulated in Table 5.1. The sandwich plate is made of FGCNTRC face sheets with a uniform distribution of CNTs and a cellular aluminium core with a uniform porosity distribution. The study is performed for different edge loadings and boundary conditions. The resultant net load is assumed to be the same for all loading types. Table 5.8 shows that the buckling load increases with a/h ratio due to higher stiffness. The concentration of stresses is highest when the plate is subjected to a concentrated load; hence, the buckling loads are the least for the concentrated loading condition.

Table 5.8: Effect of edge compression on non-dimensional critical load parameter for the sandwich skew plate. $\left(\frac{P_{cr}a^2}{E_c h^3}, V_{CN}^* = 0.17, \text{UD, UPD, } e_0 = 0.3, h_c/h_f = 8\right)$

Boundary Condition	$\frac{a}{h}$	Skew angle(ψ)	Uniform	Parabolic	Sinusoidal	Triangular	Concentrated
SSSS	10	0°	2.2403	1.8858	1.8562	1.7854	1.3260
		15°	2.4421	2.0674	2.0363	1.9624	1.4758
		30°	3.2125	2.7757	2.7406	2.6598	2.0873
		45°	5.3082	4.8014	4.7674	4.7055	3.4707
	100	0°	2.3561	1.9838	1.9528	1.8785	1.4010
		15°	2.5764	2.1810	2.1482	2.0703	1.5640
		30°	3.4294	2.9592	2.9215	2.8343	2.2392
		45°	5.8788	5.2932	5.2529	5.1761	4.5613
CCCC	10	0°	6.0591	5.1170	5.0362	4.8364	3.3054
		15°	6.3924	5.4251	5.3431	5.1432	3.5515
		30°	7.5462	6.4905	6.4042	6.2019	4.3787
		45°	10.0540	8.7621	8.6575	8.4147	5.9996
	100	0°	7.1398	6.0408	5.9468	5.7154	4.1433
		15°	7.6056	6.4716	6.3759	6.1437	4.5432
		30°	9.3162	8.0697	7.9698	7.7415	6.1002
		45°	13.6136	12.1069	11.9966	11.7682	9.7466

Table 5.9 reports the effect of CNT distribution in facings on the eigen-buckling loads for the sandwich skew plate with cellular aluminium core with uniform porosity distribution subjected to uniform edge load. The buckling loads are presented for different types of CNT distributions, CNT volume fractions and boundary conditions. The results indicate that an increase in the concentration of CNTs in the facings increases the eigen buckling loads for a particular type of CNT distribution pattern. This is due to the higher elasticity modulus of the plate and higher overall stiffness. The buckling loads are found to be highest for FGX distribution, followed by UD, while being least in the case of FGO distribution for particular boundary conditions, skew angle and CNT volume fraction. Non-dimensional critical loads for sandwich skew plates subjected to uniaxial uniform edge load are reported in **Table 5.10** for two types of porosity functions in the core, different ratios of the core thickness (h_c) to face sheet thickness (h_f), boundary conditions and skew angles. The symmetric porosity distribution in the core layer yields higher buckling loads compared to UPD as the effective elastic modulus, and hence, the stiffness is lesser when the distribution is uniform compared to non-uniform symmetric distribution due to higher porosity.

Table 5.9: Effect of CNT distribution in facings on linear buckling loads for sandwich skew plate subjected to uniform compression ($\frac{P_{cr}a^2}{E_c h^3}, \frac{a}{h} = 100, e_0 = 0.3, h_c/h_f = 4, \text{U.P.D.}$)

V_{CN}^*	Skew angle (ψ)	SSSS			CCCC		
		UD	FGX	FGO	UD	FGX	FGO
0.12	0°	1.7120	1.7496	1.6751	5.4922	5.6417	5.3440
	15°	1.8557	1.8946	1.8175	5.8017	5.9544	5.6504
	30°	2.4176	2.4621	2.3741	6.9593	7.1261	6.7943
	45°	4.0560	4.1195	3.9942	9.9581	10.1712	9.7473
0.17	0°	2.1153	2.1714	2.0612	7.0262	7.2478	6.8096
	15°	2.2766	2.3344	2.2212	7.3763	7.6019	7.1565
	30°	2.9122	2.9773	2.8510	8.7032	8.9465	8.4682
	45°	4.7885	4.8789	4.7060	12.2213	12.5244	11.9318
0.28	0°	2.8399	2.9351	2.7527	9.8989	10.2687	9.5486
	15°	3.0164	3.1143	2.9283	10.2859	10.6618	9.9332
	30°	3.7221	3.8319	3.6293	11.7857	12.1883	11.4202
	45°	5.8542	6.0047	5.7412	15.9320	16.4231	15.5107

Table 5.10: Effect of porosity functions in the core on linear buckling loads for the sandwich skew plate under uniform compression ($\frac{P_{cr}a^2}{E_c h^3}, V_{CN}^* = 0.17, \text{UD}, \frac{a}{h} = 100$)

Boundary Condition	h_c/h_f	Skew angle (ψ)	UPD			SPD		
			$e_0 = 0.1$	$e_0 = 0.3$	$e_0 = 0.5$	$e_0 = 0.1$	$e_0 = 0.3$	$e_0 = 0.5$
SSSS	4	0°	2.2577	2.1153	1.9642	2.2877	2.2100	2.1322
		15°	2.4376	2.2766	2.1051	2.4715	2.3837	2.2957
		30°	3.1445	2.9122	2.6628	3.1931	3.0669	2.9398
		45°	5.2194	4.7885	4.3211	5.3091	5.0754	4.8390
	8	0°	2.6021	2.3562	2.0952	2.6539	2.5198	2.3855
		15°	2.8502	2.5764	2.2851	2.9078	2.7586	2.6091
		30°	3.8092	3.4294	3.0229	3.8889	3.6822	3.4746
		45°	6.5549	5.8788	5.1508	6.6961	6.3281	5.9573
		0°	7.3910	7.0262	6.6383	7.4675	7.2672	7.0659
CCCC	4	15°	7.7805	7.3763	6.9452	7.8650	7.6435	7.4205
		30°	9.2478	8.7032	8.1168	9.3611	9.0637	8.7631
		45°	13.0982	12.2213	11.2652	13.2791	12.8014	12.3155
	8	0°	7.7659	7.1401	6.4753	7.8974	7.5549	7.2114
		15°	8.2879	7.6059	6.8795	8.4309	8.0580	7.6835
		30°	10.1970	9.3167	8.3728	10.3808	9.9002	9.4159
		45°	14.9625	13.6147	12.1591	15.2422	14.5059	13.7609

As the porosity coefficient is increased, the buckling load decreases. It is found that buckling loads are increasing with h_c/h_f ratios. This indicates that the core layer contributes more to the

plate's stiffness than the face sheets, as the elasticity modulus of the core layer is more compared to the effective modulus of the face sheets.

5.4 Non-linear Post-Buckling Analysis

The present numerical technique is efficient for the linear buckling analysis of isotropic and sandwich plates in the previous section. The same numerical technique is extended here for the non-linear post-buckling and post-buckled vibration behaviour of the isotropic and sandwich plates.

5.4.1 Isotropic plates

In this subsection, the efficiency of the present numerical technique and the accuracy of the computer code developed herein is tested by the non-linear post-buckling analysis of the isotropic plate, which comparative results are available in the literature.

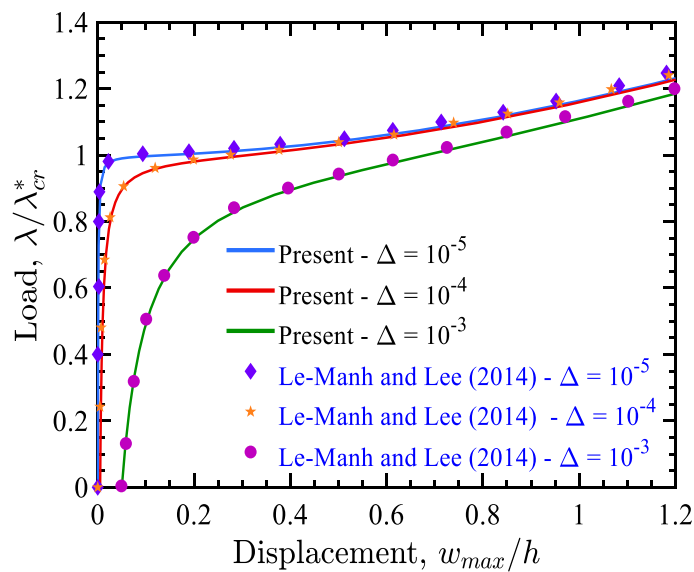


Figure 5.5: Post-buckling behaviour of an initially imperfect SSSS square isotropic plate under uniform compression

The in-house MATLAB code is validated for non-linear stability analysis of skew plates. The present results for post-buckling paths of a simply supported isotropic square plate subjected to uniaxial uniform edge load are compared to those presented by Le-Manh and Lee (Le-Manh & Lee, 2014) were obtained using NURBS based IGA with FSDT in Figure 5.5 for different

values of initial imperfections while present work based on IGA with refined higher order theory and are found to be in good agreement. A bifurcation point is observed when the initial imperfection is very small, of the order of 10^{-5} or lesser.

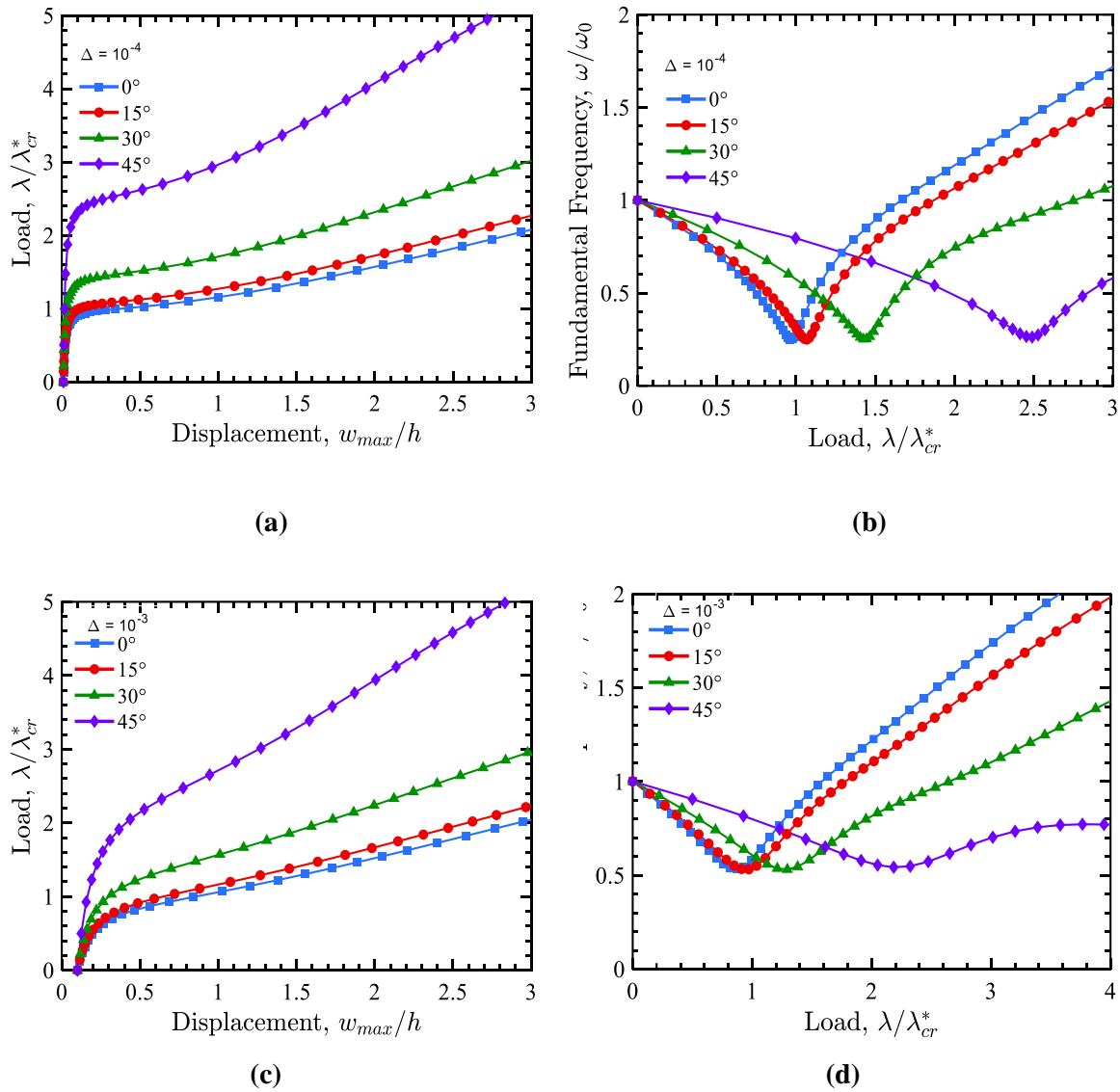


Figure 5.6: Post buckling and free vibration behaviour about the post-buckled configuration of a skew isotropic plate with different values of initial imperfections subjected to uniaxial uniform edge load.

Figures 5.6a, 5.6b, 5.6c and 5.6d show the post-buckling paths and natural frequencies of the post-buckled configuration of an SSSS isotropic skew plate subjected to uniform compression with initial imperfections 10^{-4} and 10^{-3} . The linear buckling load for the square plate is taken as the reference load (λ_{cr}^*) for all the cases. It is seen from Figures 5.6a and 5.6c that the post-buckled strength is highest for the skew angle of 45° and least for 0° because of increasing

stiffness with the skew angle, as mentioned earlier. Theoretically, at the critical load, the fundamental frequency of the perfect skew plate should be zero. However, the plate exhibits small vibrational frequencies due to the imperfection, as seen in [Figures 5.6b and 5.6d](#).

5.4.2 Skew Sandwich Plate

The post-buckling behaviours of sandwich skew ($\psi = 45^\circ$) plate with FGCNTRC facings and aluminium foam core with uniform porosity distribution are shown in [Figures 5.7a and 5.7b](#) for different distribution patterns of carbon nanotubes in the facings. The critical load for the UD case is taken as a reference (λ_{cr}^*). It is evident from the figures that there is no significant change in behaviour concerning changes in the CNT distribution pattern. This implies that the CNT pattern in the face sheets has no considerable influence on the post-buckling strength of the sandwich plate.

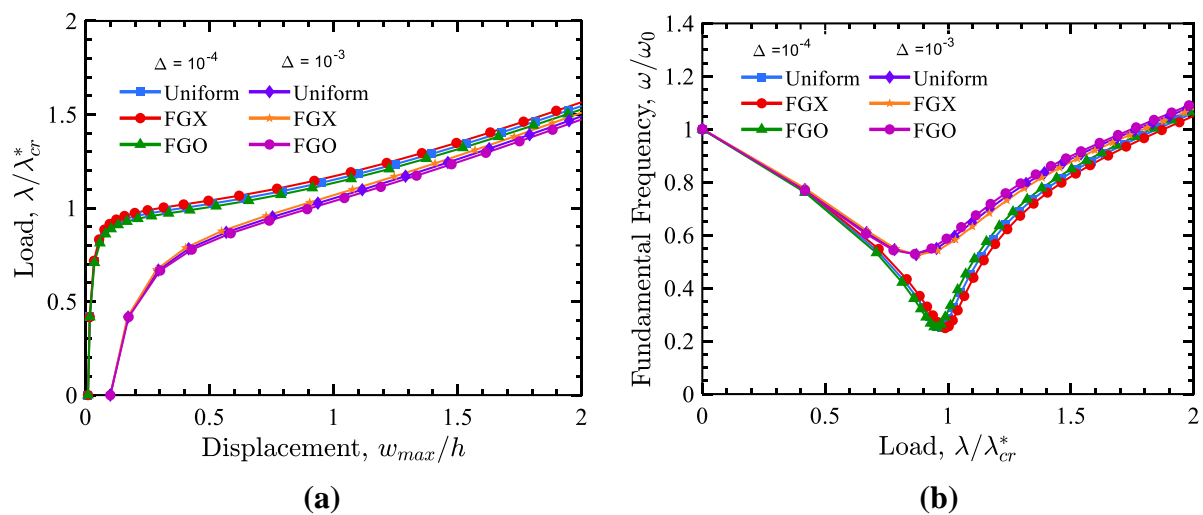


Figure 5.7: Influence of CNT distribution in the facings on post-buckling behaviour of a skew sandwich plate subjected to uniform compression ($a/h = 100$, $\psi = 45^\circ$, $h_c/h_f = 4$, $V_{CNT}^* = 0.17$, $e_0 = 0.3$, U.P.D.)

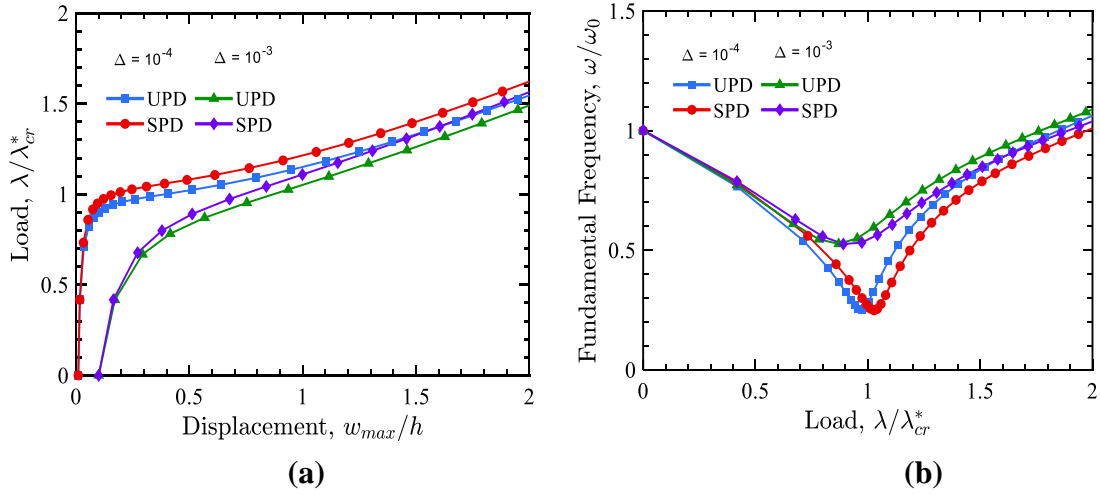


Figure 5.8: Influence of porosity functions in the core of a skew sandwich plate on post-buckling behaviour subjected to uniaxial uniform edge load ($a/h = 100, \psi = 45^\circ, h_c/h_f = 4, V_{CNT}^* = 0.17, e_0 = 0.3, UD$)

Figures 5.8a and 5.8b present the post-buckling paths and eigen frequencies about a post-buckled state of an SSSS skew sandwich plate subjected to uniform compression for different porosity distributions. The critical load for the UPD is taken as a reference (λ_{cr}^*). It is observed that the post-buckled strength is higher for SPD. The frequencies are higher for SPD than UPD before buckling and higher for UPD than SPD in the post-buckling regime. Figures 5.9a and 5.9b illustrate the post-buckling behaviours of a simply supported skew sandwich plate with UD of CNTs in the facings and UPD in the core under different edge loadings.

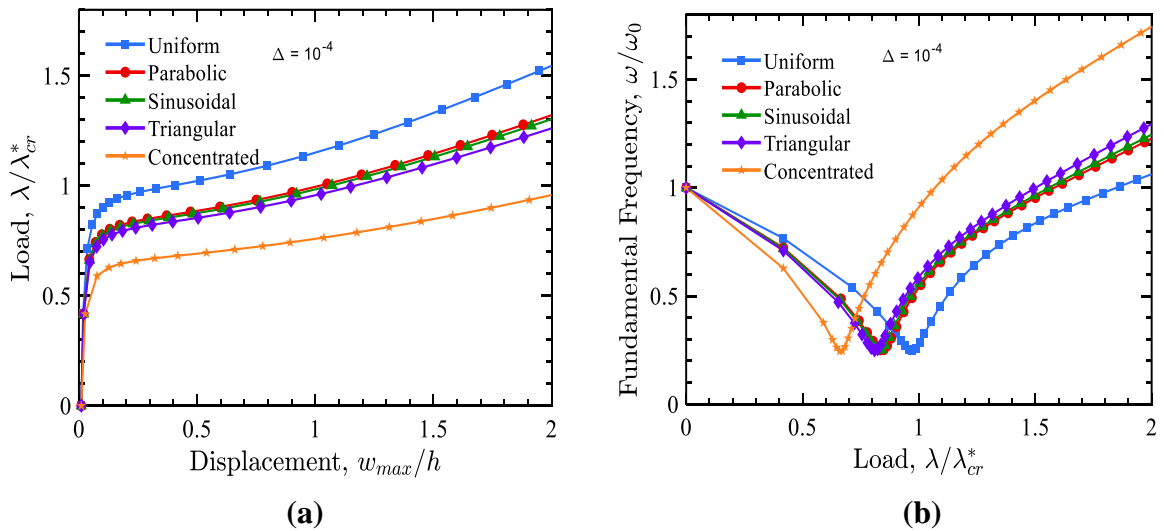


Figure 5.9: Influence of edge load distribution on post-buckling behaviour of a skew sandwich plate ($a/h = 100, \psi = 45^\circ, h_c/h_f = 4, V_{CNT}^* = 0.17, e_0 = 0.3, UD, UPD$.)

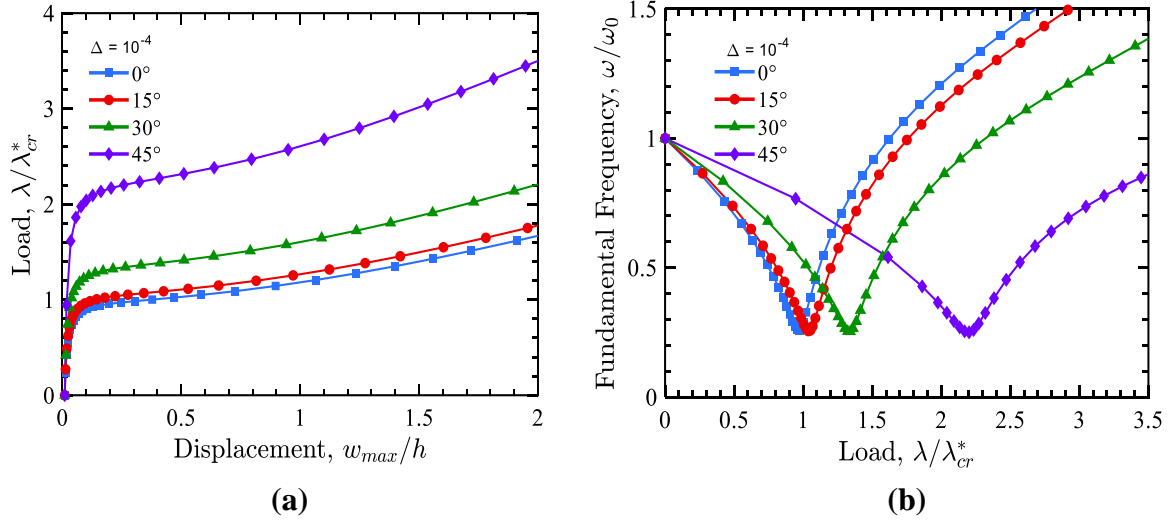


Figure 5.10: influence of skew angle on post-buckling paths and post-buckled vibration behaviour of a skew sandwich plate ($a/h = 100, h_c/h_f = 4, V_{CNT}^* = 0.17, e_0 = 0.3, UD, UPD.$)

The linear buckling of the plate subjected to uniform compression is taken as the reference (λ_{cr}^*). Figure 5.9a shows that the post-buckling strength is the least for concentrated load and is greatest under uniform edge load. From Figure 5.9b, it can be seen that the lowest load at which the plate exhibits minimum frequency is when the plate is under a concentrated load. The influence of skew angle on the post-buckling and post-buckled vibration behaviour is presented in Figures 5.10a and 5.10b. The buckling parameter of the square plate is taken as the reference (λ_{cr}^*). The post-buckling strength increases with the skew angle due to the increase in stiffness of the plate. Figure 5.10b shows that for the same load, the fundamental frequency of the equilibrium position is highest when the skew angle is 45° and is least for 0° in the pre-buckling regime. The trend is reversed in the post-buckled configuration.

5.5 Displacement Through Thickness

Analysing displacement through the thickness is essential to comprehending how structures behave when subjected to dynamic loading conditions. This factor plays a significant role in several applications, including vibration analysis, modal analysis, and structural design. To understand the displacement patterns through the thickness of vibrating structures, engineers and researchers frequently rely on numerical methods and finite element analysis to analyse and visualise the data. The mode shapes of a vibrating structure provide a visual representation of the displacement distribution across the structure, highlighting the unique characteristics of each vibrational mode. These mode shapes are inherently linked to the natural frequency of

vibration and are affected by factors such as boundary conditions, material properties, and the type of excitation. As one examines the displacement through the thickness of the structure, it becomes apparent that this varies along the length of the structure, demonstrating the complex interplay between these various factors.

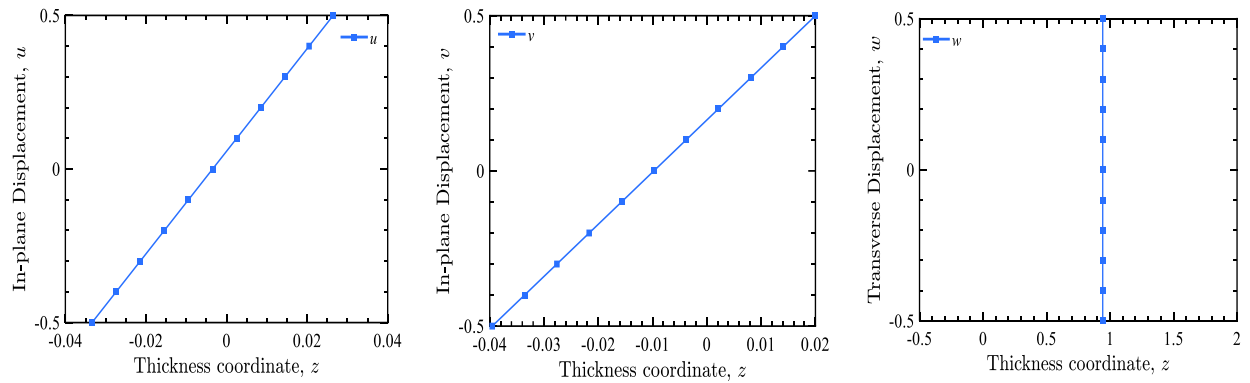


Figure 5.11: In-plane and Transverse Displacement through-thickness for pre-buckled vibration behaviour about the equilibrium position ($\frac{\lambda}{\lambda_{cr}} = 0.5$) of a square sandwich plate subjected to uniform compression ($\frac{a}{h} = 100, \frac{h_c}{h_f} = 4, V_{CNT}^* = 0.17, e_0 = 0.3$, U. P. D.)

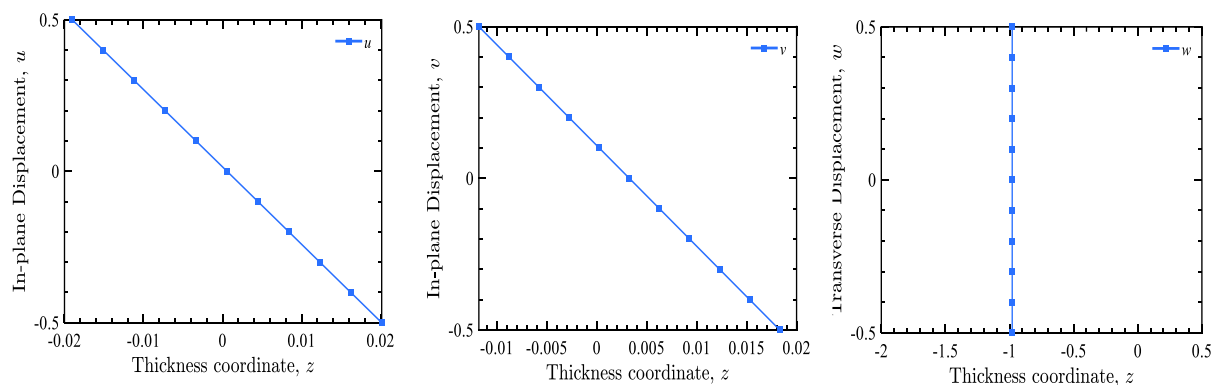


Figure 5.12: In-plane and Transverse Displacement through-thickness for post-buckled vibration behaviour about the equilibrium position ($\frac{\lambda}{\lambda_{cr}} = 1.5$) of a square sandwich plate subjected to uniform compression ($\frac{a}{h} = 100, \frac{h_c}{h_f} = 4, V_{CNT}^* = 0.17, e_0 = 0.3$, U. P. D.)

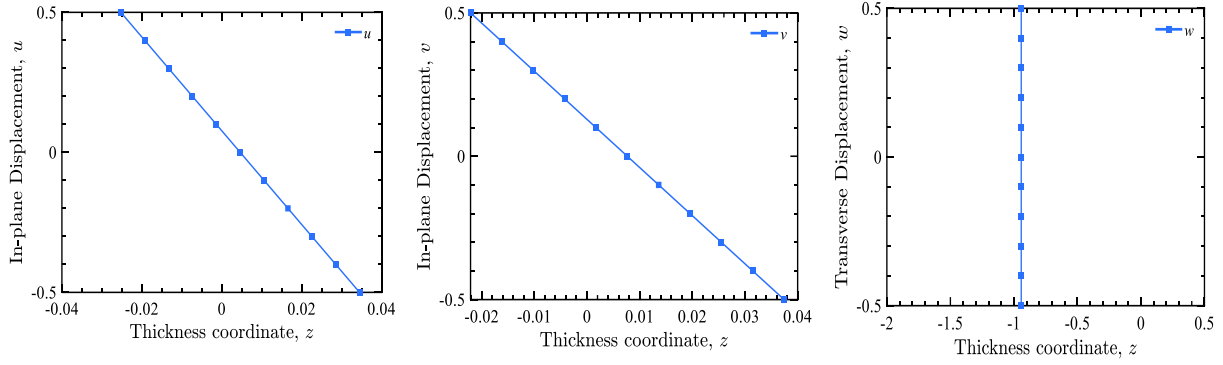


Figure 5.13: In-plane and Transverse Displacement through-thickness for pre-buckled vibration behaviour about the equilibrium position ($\frac{\lambda}{\lambda_{cr}^*} = 0.5$) of a square sandwich plate subjected to uniform compression ($\frac{a}{h} = 100, \frac{h_c}{h_f} = 8, V_{CNT}^* = 0.17, e_0 = 0.3, \text{U. P. D.}$)

Figures 5.11, 5.12, 5.13, and 5.14 display the relative displacements across the thickness of the sandwich plate, comparing two distinct core-to-face sheet thickness ratios. These results were obtained through non-polynomial higher-order theory, illustrating pre-buckled and post-buckled vibration behaviour. Generally, the specific modes in the thickness direction depend on the position within the given sandwich structures.

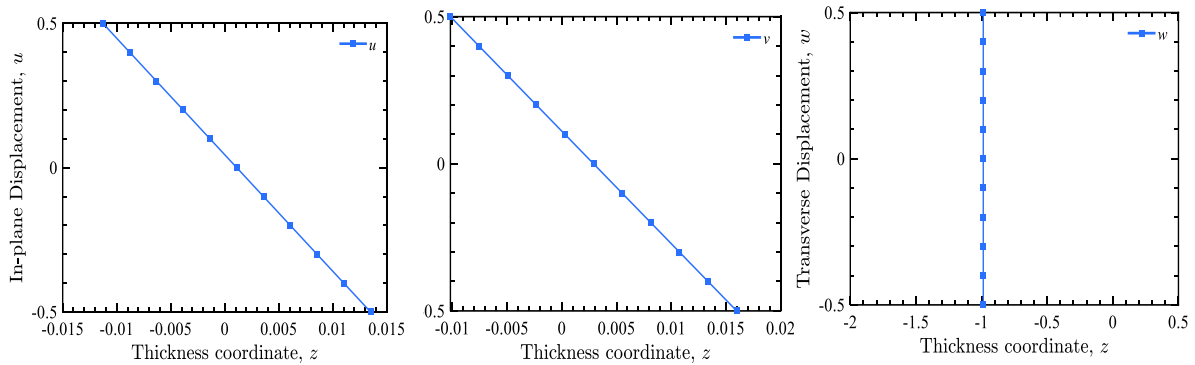


Figure 5.14: In-plane and Transverse Displacement through-thickness for post-buckled vibration behaviour about the equilibrium position ($\frac{\lambda}{\lambda_{cr}^*} = 1.5$) of a square sandwich plate subjected to uniform compression ($\frac{a}{h} = 100, \frac{h_c}{h_f} = 8, V_{CNT}^* = 0.17, e_0 = 0.3, \text{U. P. D.}$)

The zigzag-based displacement model can be employed to obtain the accurate distribution of displacements through-thickness for a specific mode. This study primarily focuses on the global buckling and post-buckled vibration behaviour of sandwich plates. Therefore, the

authors utilised the equivalent single-layer theory to comprehend the vibration behaviour of plates around pre-buckled and post-buckled equilibrium configurations.

5.6 Summary

An isogeometric (IGA) non-polynomial higher-order theory formulation is used to study the post-buckling and free vibration behaviour of the post-buckled configuration of the skew plate with FGCNTRC facings and an aluminium foam core. The midplane assumptions are based on a non-polynomial higher-order theory, and the strain-displacement relations are based on von Kármán assumptions. The effect of CNT pattern in face sheets, porosity distribution in the core layer, edge loading conditions, skew angle, side-to-thickness ratio, and volume fraction index of CNTs on the stability and vibration behaviour of the sandwich plates are studied. The skew angle affects the static and dynamic characteristics of the sandwich plate for all boundary conditions. As the skew angle of the sandwich plate increases, the buckling strength increases for both SSSS and CCCC skew sandwich plates due to the higher stiffness of the plate. The buckling strength of the sandwich skew plate under uniform compression reduces with the reduction in the porosity due to lower flexural stiffness and the same geometric stiffness. The buckling load and post-buckling strength are higher for the SPD than UPD because the symmetric porosity distribution reduces the stiffness of the plate by a smaller amount than the uniform porosity distribution. In the pre-buckling region, the frequencies are higher for SPD than UPD and higher for UPD than SPD in the post-buckling regime. The buckling loads increase with h_c/h_f ratio. This indicates that the core layer contributes more to the plate's stiffness than the face sheets, as the elasticity modulus of the core layer is more than the resultant modulus of the facings. The buckling strength is higher when the CNTs are distributed more towards the plate's surfaces than the centre. The critical load is highest for uniform compression and least under concentrated load due to a high concentration of stresses.

Stability Analysis of Plates in Thermal Environment

6.1 Introduction

In this chapter, an in-depth investigation is conducted on sandwich plates' linear and non-linear stability behaviours in a thermal environment. The efficiency of the Isogeometric analysis, with non-polynomial higher-order theory, and the accuracy of the in-house MATLAB code have already been established in Chapter 5 for linear and non-linear analyses of sandwich plates under non-uniform mechanical loading conditions. The suitability of the same numerical technique and the in-house MATLAB code is explored for the sandwich plate's linear buckling and non-linear post-buckling analysis in a thermal environment. Section 6.2 presents the geometrical and material variables of sandwich plates, providing a detailed overview of the parameters that affect the stability behaviours of sandwich plates. Section 6.3 explains the plates' linear thermal buckling analysis, highlighting the sandwich plates' response to thermal loads. Section 6.4 examines the behaviour of sandwich plates after buckling and the influence of thermal loads on this behaviour. Finally, Section 6.5 summarises the observations from this numerical work, providing valuable insights into the linear and non-linear stability behaviours of sandwich plates and the influence of thermal loads on these behaviours. The non-linear stability behaviour of skew sandwich plates with re-entrant auxetic cores under thermal loading is limited. The present work investigates the buckling and post-buckling behaviour of initially imperfect sandwich plates (square and skew) with an auxetic core possessing tunable material properties under various thermal loading conditions and boundary constraints.

6.2 Geometrical and Material Variables of Sandwich Plate

[Figure 6.1](#) illustrates the shape and geometrical parameters of the skew plates. An essential aspect to consider is determining the thermomechanical properties of carbon nanotubes as a function of temperature. To achieve this, a fourth-degree interpolation function is utilised to

calculate the thermomechanical characteristics of CNTs. Through this function, each property is accurately represented as:

$$P = P_0 + P_1(T/T_0) + P_2(T/T_0)^2 + P_3(T/T_0)^3 + P_4(T/T_0)^4 \quad (6.1)$$

in which $T = T_0 + \Delta T$, ΔT is the temperature increment in the environment containing the material and $T_0 = 300$ K (room temperature). The values of unique coefficients P_i are provided in Table 6.1 for each thermomechanical property. The three forms of CNT distributions (Kiani, 2018), uniform distribution (UD), FGX and FGO, are illustrated in Figure 6.2, and the corresponding functions are tabulated in Table 6.2. In all three scenarios, the total volume fraction of CNTs is considered to be the same. In Table 6.2, h_t and h_b represent the top and bottom positions of two-layer ends in the transverse direction. The matrix is made of PMMA, and its material properties are assumed to vary linearly with temperature (Thanh et al., 2017)

$$E_m = (3.52 - 0.0034T)\text{GPa}, v_m = 0.34, \alpha_m = 45(1 + 0.0005\Delta T) \times \frac{10^{-6}}{K}, \rho_m = 1150\text{kg/m}^3$$

The resultant Young's modulus, shear modulus and Poisson's ratio of facings are determined using the modified rule of mixtures with efficiency parameters as:

$$E_{11} = \eta_1 V_{CN} E_{11}^{CN} + V_m E_m \quad (6.2)$$

$$\eta_2/E_{22} = V_{CN}/E_{22}^{CN} + V_m/E_m \quad (6.3)$$

$$\eta_3/G_{12} = V_{CN}/G_{12}^{CN} + V_m/G_m \quad (6.4)$$

The effective Poisson ratio of face sheets depends weakly on position (Jam & Kiani, 2015; Shen, 2011) and is expressed as a

$$v_{12} = V_{CN} v_{12}^{CN} + V_m v_m \quad (6.5)$$

$$\rho = V_{CN} \rho^{CN} + V_m \rho_m \quad (6.6)$$

The longitudinal and transverse thermal expansion coefficients can be represented as follows (Kiani, 2018)

$$\alpha_{11} = V_{CN} \alpha_{11}^{CN} + V_m \alpha_m \quad (6.7)$$

$$\alpha_{22} = (1 + v_{12}^{CN}) V_{CN} \alpha_{22}^{CN} + (1 + v_m) V_m \alpha_m - v_{12} \alpha_{11} \quad (6.8)$$

E_{11}^{CN} , E_{22}^{CN} , G_{12}^{CN} and v_{12}^{CN} indicate the properties of CNTs, while E_m , G_m and v_m are similar to the PMMA matrix. V_{CN} and V_m are the volume fractions of CNT and the matrix, respectively. α_{11}^{CN} , α_{22}^{CN} and α_m are the thermal expansion coefficients of the CNT and matrix, respectively. The efficiency parameters (η_1, η_2, η_3) (Jiang et al., 2014) given in Table 6.3 are used to account

for the difference in the resultant properties estimated through the simple rule of mixtures and those determined using molecular dynamics simulations.

Table 6.1: P_i coefficients for various thermomechanical characteristics associated with fourth-order interpolation. (Kiani, 2018)

P	P_0	P_1	P_2	P_3	P_4
E_{11} [TPa]	+6.56537	-1.76156	+1.13347	-0.32260	+0.03193
E_{22} [TPa]	+8.22710	-2.19725	+1.41176	-0.40125	+0.03964
G_{12} [TPa]	+1.10442	+1.88427	-1.47623	+0.49029	-0.05829
α_{11} [$10^{-6}/^\circ\text{C}$]	-1.12800	+6.88290	-2.60621	+0.31023	-0.00054
α_{22} [$10^{-6}/^\circ\text{C}$]	+5.43593	-0.29201	+0.02268	+0.00182	-0.00023
ν_{12}	+0.17500	0	0	0	0

Table 6.2: CNTs' volume fraction function for various distributions

CNTs Pattern	UD	FGX	FGO
The volume fraction of CNTs in the facings	V_{CN}^*	$\frac{4}{h_t - h_b} \left(\left \frac{h_t + h_b}{2} - z \right \right) V_{CN}^*$	$\frac{4}{h_t - h_b} \left(\frac{h_t - h_b}{2} - \left \frac{h_t + h_b}{2} - z \right \right) V_{CN}^*$

Table 6.3: FGCNTRC efficiency parameters (Wang & Shen, 2012)

Volume Fraction (V_{CN}^*)	Efficiency Values
0.12	$\eta_1 = 0.137, \eta_2 = 1.022, \eta_3 = 0.7\eta_2$
0.17	$\eta_1 = 0.142, \eta_2 = 1.626, \eta_3 = 0.7\eta_2$
0.28	$\eta_1 = 0.141, \eta_2 = 1.585, \eta_3 = 0.7\eta_2$

The material properties of the auxetic re-entrant core made up of aluminium ($E = 69$ GPa, $\nu = 0.3$, $G = 27$ GPa and $\rho = 2700$ kg/m³) (Gupta & Pradyumna, 2022) are dependent on various geometrical parameters and can be written as (Thuy Anh et al., 2022)

$$E_{11}^{(c)} = E \left(\frac{t}{l_1} \right)^3 \frac{\left(\frac{l_2}{l_1} - \sin \theta_{hc} \right)}{\cos^3 \theta_{hc} \left[1 + \left(\tan^2 \theta_{hc} + \frac{l_2}{l_1} \sec^2 \theta_{hc} \right) \left(\frac{t}{l_1} \right)^2 \right]}$$

$$E_{22}^{(c)} = E \left(\frac{t}{l_1} \right)^3 \frac{1}{\cos \theta_{hc} \left(\frac{l_2}{l_1} - \sin \theta_{hc} \right) \left(\tan^2 \theta_{hc} + \left(\frac{t}{l_1} \right)^2 \right)}$$

$$G_{12}^{(c)} = E \left(\frac{t}{l_1} \right)^3 \frac{1}{\left(\frac{l_2}{l_1} \right) \left(1 + 2 \frac{l_2}{l_1} \right) \cos \theta_{hc}}$$

$$G_{23}^{(c)} = G \left(\frac{t}{l_1} \right) \frac{\cos \theta_{hc}}{\left(\frac{l_2}{l_1} - \sin \theta_{hc} \right)} \quad (6.9)$$

$$G_{13}^{(c)} = G \frac{\left(\frac{t}{l_1} \right)}{2 \cos \theta_{hc}} \left[\frac{\left(\frac{l_2}{l_1} - \sin \theta_{hc} \right)}{\left(1 + 2 \frac{l_2}{l_1} \right)} + \frac{\left(\frac{l_2}{l_1} + 2 \sin^2 \theta_{hc} \right)}{2 \left(\frac{l_2}{l_1} - \sin \theta_{hc} \right)} \right]$$

$$v_{12}^{(c)} = - \frac{\sin \theta_{hc} \left(1 - \left(\frac{t}{l_1} \right)^2 \right) \left(\frac{l_2}{l_1} - \sin \theta_{hc} \right)}{\cos^2 \theta_{hc} \left[1 + \left(\tan^2 \theta_{hc} + \frac{l_2}{l_1} \sec^2 \theta_{hc} \right) \left(\frac{t}{l_1} \right)^2 \right]}$$

$$v_{21}^{(c)} = - \frac{\sin \theta_{hc} \left(1 - \left(\frac{t}{l_1} \right)^2 \right)}{\left(\tan^2 \theta_{hc} + \left(\frac{t}{l_1} \right)^2 \right) \left(\frac{l_2}{l_1} - \sin \theta_{hc} \right)}$$

$$\rho^{(c)} = \rho \frac{\left(\frac{t}{l_1} \right) \left(\frac{l_2}{l_1} + 2 \right)}{2 \cos \theta_{hc} \left(\frac{l_2}{l_1} - \sin \theta_{hc} \right)}$$

$$\alpha_{11}^{(c)} = \alpha \times \frac{\left(\frac{t}{l_1} \right) \cos \theta_{hc}}{\left(\sin \theta_{hc} + \frac{l_2}{l_1} \right)}; \alpha_{22}^{(c)} = \alpha \times \frac{\left(\frac{t}{l_1} \right) \left(\frac{l_2}{l_1} + \sin \theta_{hc} \right)}{\left(2 \frac{l_2}{l_1} + 1 \right) \cos \theta_{hc}}$$

$E_{11}^{(c)}$, $E_{22}^{(c)}$, $G_{12}^{(c)}$, $G_{23}^{(c)}$, $G_{13}^{(c)}$, $\nu_{12}^{(c)}$, $\nu_{21}^{(c)}$ and $\alpha_{11}^{(c)}$, $\alpha_{22}^{(c)}$ are Young's moduli shear moduli, Poisson's ratio and longitudinal and transverse thermal expansion coefficients of the auxetic core. ρ is the density of the core material, i.e., aluminium. Where l_1 is the length of the inclined cell rib, l_2 is the length of the vertical cell rib, t is the rib thickness, and θ_{hc} is the inclined cell angle, as shown in [Figure 6.1](#). Additionally, h_2 refers to the thickness of the auxetic core, and h_1 represents the facings thickness of the top layer, which is equal to the bottom layer thickness.

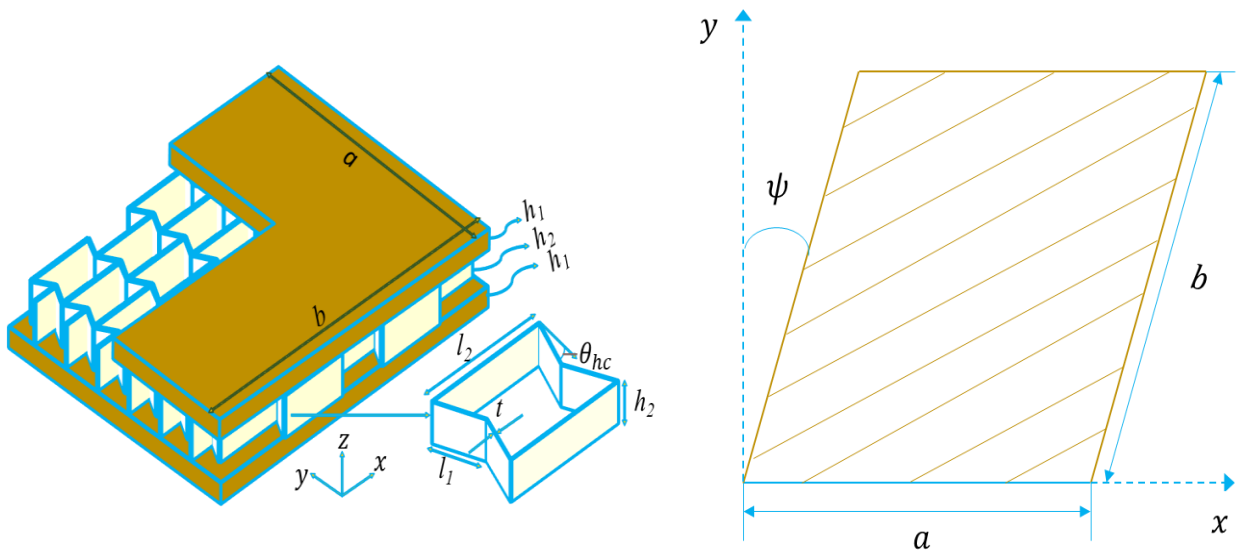


Figure 6.1: Shapes and geometrical parameters of the sandwich skew plate

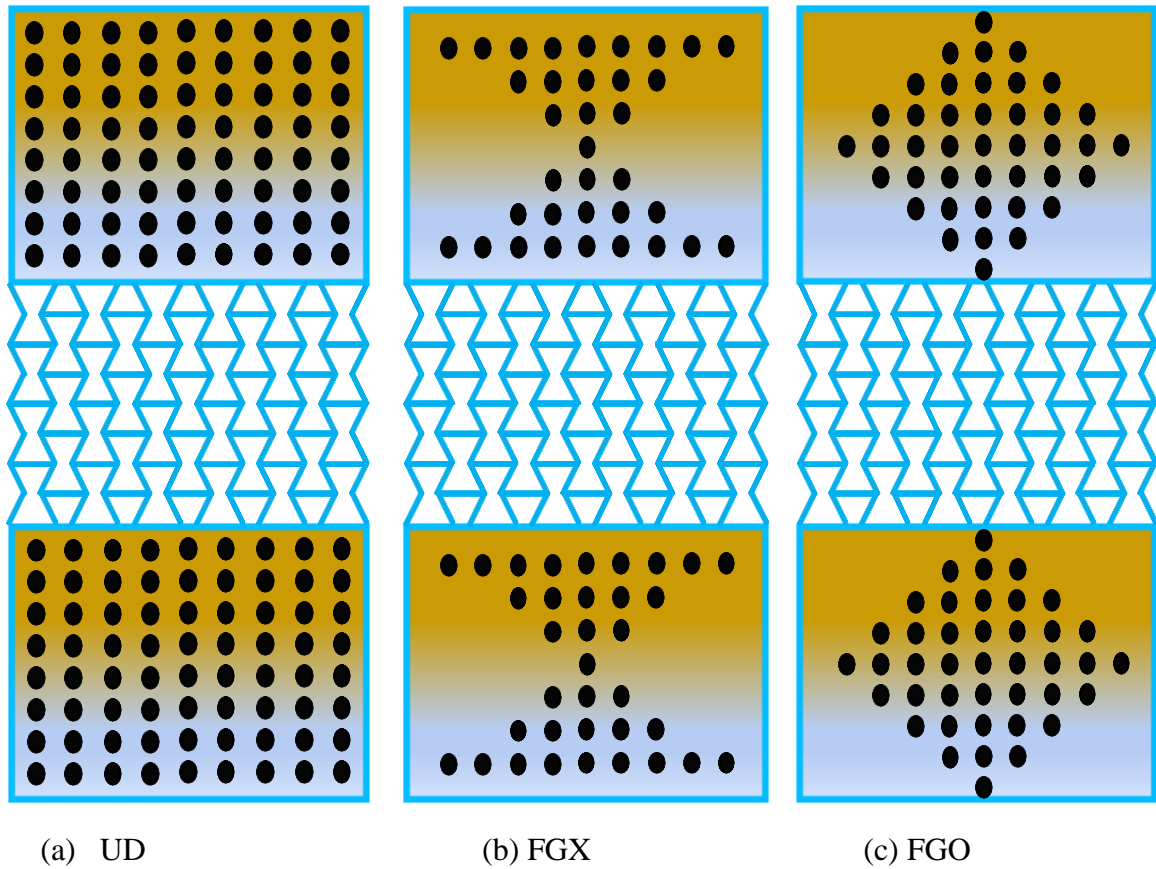


Figure 6.2: Different CNT patterns in facings and the re-entrant auxetic core.

6.2.1 Boundary Conditions

The different types of edge constraints for the plate are given as:

$$(A) \text{ Simply supported : (SSSS): } \begin{cases} u_0 = v_0 = w_0 = \theta_y = 0 \text{ on } x = 0, a \\ u_0 = v_0 = w_0 = \theta_x = 0 \text{ on } y = 0, b \end{cases}$$

$$(S^1S^1S^1S^1): \begin{cases} v_0 = w_0 = \theta_y = 0 \text{ on } x = 0, a \\ u_0 = w_0 = \theta_x = 0 \text{ on } y = 0, b \end{cases}$$

$$(B) \text{ Clamped support : (CCCC): } \begin{cases} u_0 = v_0 = w_0 = \theta_x = \theta_y = 0 \\ w_{0,x} = w_{0,y} = 0 \end{cases} \text{ All edges}$$

In the present article SSSS, boundary conditions are used for all the cases unless a particular case is specified.

6.3 Linear Thermal Buckling Analysis

A MATLAB code has been created to conduct linear buckling and non-linear post-buckling analyses of sandwich plates under thermal loading conditions. Several validation studies have been undertaken to ascertain the correctness of the code.

6.3.1 Linear Stability Analysis for Isotropic, Laminated, and Sandwich Plate

Firstly, the MATLAB code developed is confirmed by performing validation studies on linear thermal buckling analysis of the plate:

- Critical temperature parameters (T_{cr}) for the SSSS FGCNTRC square plate under thermal load are determined for different volume fractions in [Table 6.4](#). The results are compared to those given by [Shen & Zhang \(2010\)](#) were obtained using multi-scale approach, and [Kiani \(2017\)](#) was obtained using Ritz-based solution with FSDT while present work based on IGA with refined higher order theory and are in good agreement. The study is conducted for two distinct orders of the B-spline curve, $p = 2$ and $p = 3$, where p is the order of the curve, and it is noticed that the results converge faster and require a lesser number of knot insertions (nk) as the order of the curve increases. Hence, order 3 with 13-knot insertions is employed in all the following investigations.
- [Table 6.5](#) shows the thermal buckling parameter (λ_{cr}) for a $[0/90^\circ]$ laminated skew plates with various skew angles and boundary conditions. The findings of [Kant & Babu \(2000\)](#) were obtained using a higher-order shear deformation theory (HSDT) with finite elements.

Table 6.4: Convergence of critical buckling temperature parameter (T_{cr}) for simply supported (SSSS) FGCNTRC plates established on a temperature-dependent analysis. ($a/b = 1$)

a/h	p	nk	NCP	V_{CN}^*						
				0.12		0.17		0.28		
				UD	FGX	UD	FGX	UD	FGX	
10	2	2	5 × 5	392.25	405.91	403.89	420.80	396.21	411.93	
		4	7 × 7	390.95	404.64	402.35	419.28	395.04	410.85	
		6	9 × 9	390.54	404.33	401.86	418.92	394.63	410.54	
		8	11 × 11	390.24	404.09	401.53	418.65	394.31	410.28	
		10	13 × 13	390.03	403.90	401.30	418.43	394.08	410.08	
		12	15 × 15	389.89	403.75	401.15	418.28	393.93	409.92	
	3	2	14	17 × 17	389.79	403.65	401.05	418.16	393.81	409.80
			16	19 × 19	389.72	403.57	400.97	418.08	393.73	409.70
			3	7 × 7	389.87	403.74	401.14	418.27	393.90	409.89
		3	5	9 × 9	389.44	403.24	400.69	417.73	393.41	409.30
			7	11 × 11	389.41	403.19	400.65	417.68	393.37	409.24
			9	13 × 13	389.41	403.18	400.65	417.68	393.37	409.23
			11	15 × 15	389.40	403.18	400.65	417.67	393.36	409.23
			13	17 × 17	389.40	403.18	400.65	417.67	393.36	409.23
			15	19 × 19	389.40	403.18	400.65	417.67	393.36	409.23
			Shen & Zhang (2010)	388.19	403.91	399.44	419.09	391.62	410.58	
			Kiani (2017)	387.63	402.25	399.03	419.13	390.81	415.79	
20	2	2	5 × 5	341.42	353.57	345.23	359.64	346.24	361.71	
		4	7 × 7	340.34	352.23	344.03	358.13	345.08	360.31	
		6	9 × 9	339.94	351.84	343.57	357.66	344.69	359.96	
		8	11 × 11	339.75	351.63	343.36	357.42	344.49	359.74	
		10	13 × 13	339.66	351.51	343.25	357.29	344.38	359.61	
		12	15 × 15	339.60	351.44	343.19	357.21	344.32	359.52	
	3	2	14	17 × 17	339.57	351.39	343.16	357.16	344.28	359.47
			16	19 × 19	339.54	351.36	343.13	357.13	344.25	359.43
			3	7 × 7	339.61	351.46	343.20	357.23	344.33	359.54
		3	5	9 × 9	339.46	351.25	343.04	357.01	344.15	359.30
			7	11 × 11	339.45	351.24	343.03	356.99	344.14	359.28
			9	13 × 13	339.45	351.24	343.03	356.99	344.14	359.28
			11	15 × 15	339.45	351.24	343.03	356.99	344.14	359.28
			13	17 × 17	339.45	351.24	343.03	356.99	344.14	359.28
			15	19 × 19	339.45	351.24	343.03	356.99	344.14	359.28
			Shen & Zhang (2010)	339.42	353.20	343.00	359.52	344.08	362.06	
			Kiani (2017)	339.40	352.77	343.00	359.43	344.05	364.07	

formulation, while Kiani (2017) employed First-order shear deformation theory FSDT with the Ritz method for thin plates. The obtained results agree with those of Kant & Babu (2000) and Kiani (2017), while present work based on IGA with refined higher order theory, confirming the effectiveness of the proposed approach.

- (c) Since no study is available for linear thermal buckling behaviour of auxetic core sandwich plates with FGCNTRC facings, the present formulation is validated for its accuracy by

comparing it with similar works. Table 6.6 shows the non-dimensional frequencies of the re-entrant core-based sandwich plate for different h_2/h ratios and cell angle θ_{hc} , along with the results of Gupta & Pradyumna (2022) were obtained using FEM with TSDT and Cong & Duc (2021) were obtained using analytical approach with Reddys FSDT, while present work based on IGA with refined higher order theory, and it shows good agreement. The non-dimensional parameters, $\bar{\omega}_L = \omega(a^2/h)\sqrt{12\rho(1-\nu^2)/E_2}$ is considered for non-dimensional values.

- (d) The linear buckling loads of an initially imperfect uniformly heated isotropic ceramic plate ($E=380\text{GPa}$, $\alpha = 7.4\times 10^{-6}/^\circ\text{C}$, $\nu = 0.30$, $a/h = 100$) simply supported ($S^1S^1S^1S^1$) is plotted against different imperfection amplitude size μ of a sine type imperfection in Figure 6.4. Figure 6.4 illustrates that critical temperature increases steadily change in imperfection amplitude μ from 0 to 1, establishing a good match of the present results with those based on the layer wise theory model (Cetkovic, 2022) while present work based on IGA with refined higher order theory.

Table 6.5: Thermal buckling parameter $\lambda_{cr} = 100\alpha_{22}\Delta T_{cr}$ of $[0/90^\circ]_s$ laminated skew plates with numerous skew angles and BC. ($a/h = 100$, $a/b = 1$)

BC	Skew angle (ψ)	Present	Kiani (2017)	Kant & Babu (2000)
SSSS	0°	0.0996	0.0997	0.0996
	15°	0.1018	0.1018	0.1017
	30°	0.1118	0.1108	0.1116
	45°	0.1433	0.1433	0.1427
CCCC	0°	0.3352	0.3354	0.3348
	15°	0.3444	0.3446	0.3441
	30°	0.3576	0.3578	0.3572
	45°	0.4175	0.4179	0.4169

Figure 6.3 shows the effects of the inclination angle of the unit cell on the Poisson's ratio of the auxetic core sandwich plate with varied l_2/l_1 and $t/l_1 = 0.1$ values. It can be seen that negative poisons ratio (NPR) values are associated with positive cell angles. Therefore, cell angle ($\theta_{hc} = 30^\circ$) is used for all subsequent investigations unless specified. Table 6.7 analyses the influence of various geometric imperfection modes on critical buckling temperature $\Delta\bar{T}_{cr}$ of thin ($a/h = 100$) ceramic plate. It is noted that the L3 and L2 local-type imperfections show the least effect on critical buckling temperature, whereas the greater influence has all global-type imperfections G3, G2 and G1. Table 6.8 shows the influence of two imperfection modes with different width-to-thickness ratios on the critical buckling temperature of a simply supported (SSSS) square sandwich plate with the auxetic core. As the imperfection amplitude increases and the width-to-thickness ratio decreases, the critical buckling temperature for the square

sandwich plate increases. The results are expected since, with increasing the thickness, the flexural rigidity of the plate increases. Table 6.9 includes new results on the effect of two imperfection modes on critical temperature for sandwich plates with auxetic core for numerous skew angles and boundary conditions. As the imperfection amplitude and skew angle increase, the critical temperature for the skew sandwich plate increases. It is also observed that critical buckling temperate is higher for CCCC boundary conditions than SSSS boundary conditions.

Table 6.6: Non-dimensional frequency parameters of the auxetic core sandwich plate for various θ_{hc} and h_2/h . ($a/h = 100, t/l_1 = 0.1, l_2/l_1 = 2, a/b = 1$)

θ_{hc}	h_2/h	Present	Gupta & Pradyumna (2022)	Cong & Duc (2021)
0°	0.3	22.774	22.723	22.814
	0.5	24.877	24.825	24.905
	0.7	26.318	26.298	26.409
	0.9	23.916	23.911	23.990
30°	0.3	22.522	22.486	22.552
	0.5	24.269	24.238	24.317
	0.7	24.997	24.996	25.102
	0.9	20.986	21.031	21.049

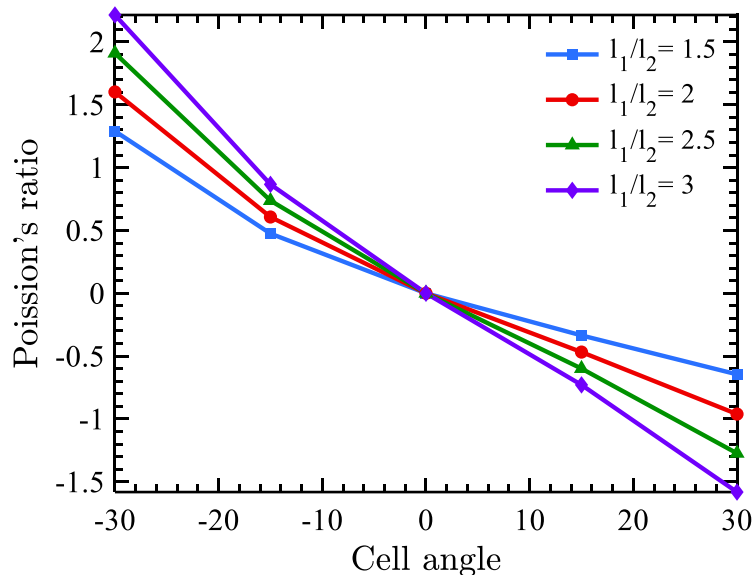


Figure 6.3: Poisson's ratio Vs. cell angle with various cell aspect ratio

Table 6.10 contains the results for linear stability characteristics of a sandwich plate with different types of CNT distribution in face sheets. Buckling loads are shown for various CNT

distributions, concentrations, and BCs. The tabulated values indicate that increasing the CNT concentration in the facings improves buckling strength for a specific CNT distribution pattern. This may be attributed to improved effective elasticity modulus and overall stiffness of the plate. Furthermore, buckling strength improves when the CNTs are non-uniformly distributed (FGX) through-thickness for a particular case of BC, skew angle, and CNT volume fraction. The influence of cell angle (θ_{hc}) of the re-entrant core on the critical temperature of the sandwich plate is studied in Table 6.11. It can be inferred that the change in cell angle and rib thickness ratio (l_1/l_2) has minimal effect on the results. The results are reported in Table 6.12 for three distinct (h_2/h) ratios. The upper and lower facings' thickness should be the same for the sandwich laminate.

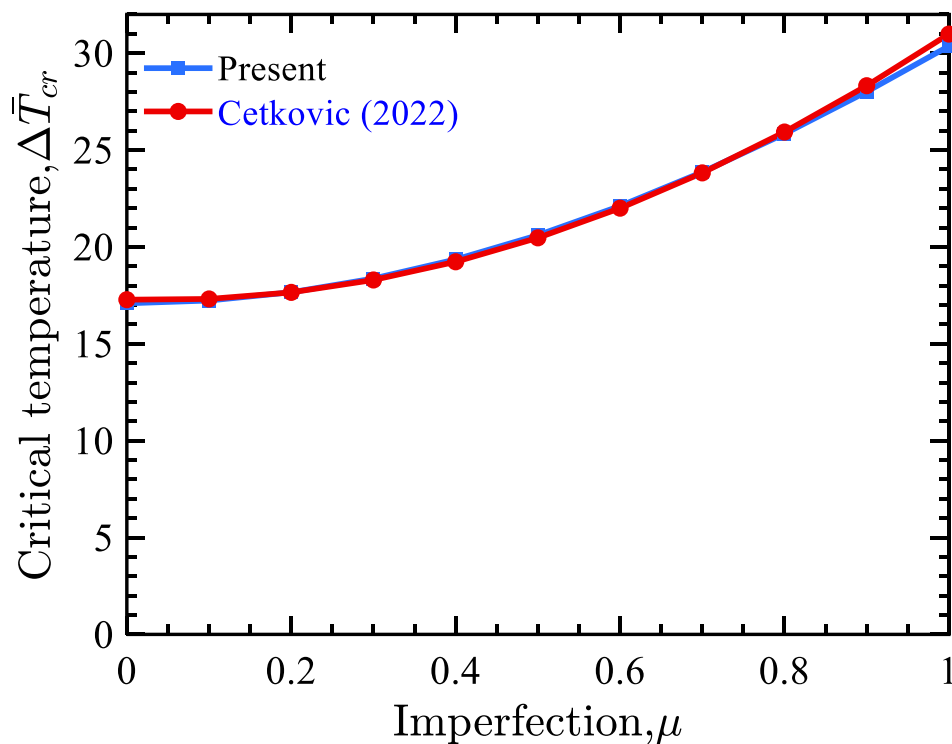


Figure 6.4: Critical buckling temperature ($\Delta\bar{T}_{cr}$) Vs. Imperfection size μ for isotropic imperfect ceramic plate

Table 6.7: Critical temperature $\Delta\bar{T}_{cr}$ of the isotropic imperfect ceramic plate for different imperfection modes under uniform temperature rise ($E = 380GPa, \alpha = 7.4 \cdot \frac{10^{-6}}{^{\circ}C}, \nu = 0.30, \frac{a}{h} = 100, S^1S^1S^1S^1$)

μ	Imperfection mode						
	S	G1	G2	G3	L1	L2	L3
0	17.0894	17.0894	17.0894	17.0894	17.0894	17.0894	17.0894
0.1	17.2324	17.2656	17.2749	17.3305	17.1267	17.1642	17.1418
0.2	17.6600	17.7836	17.8213	18.0419	17.2372	17.3851	17.2929
0.3	18.3690	18.6143	18.7018	19.1914	17.4171	17.7432	17.5263
0.4	19.3534	19.7163	19.8785	20.7348	17.6608	18.2246	17.8195
0.5	20.6051	21.0463	21.3108	22.6243	17.9615	18.8127	18.1488
0.6	22.1127	22.5521	22.9612	24.8168	18.3116	19.4902	18.4935
0.7	23.8621	24.2040	24.7984	27.2772	18.7035	20.2399	18.8374

Table 6.8: Critical buckling temperature $(\Delta T)_{cr}$ of the simply supported square sandwich plate with auxetic core for two different imperfection modes under a uniform temperature rise ($l_2/l_1 = 2, t/l_1 = 0.1, h_2/h=0.5$ and $a/h = 100, V_{CNT}^* = 0.17, \theta_{hc} = 30^{\circ}, UD$)

μ	Imperfection mode					
	10		20		100	
	S	L2	S	L2	S	L2
0	218.8950	218.8950	81.4072	81.4072	3.8868	3.8868
0.1	226.7205	219.8575	83.6416	81.6942	3.9837	3.8994
0.2	249.7625	222.2592	90.2869	82.5025	4.2731	3.9367
0.3	286.6976	225.2103	101.1649	83.7012	4.7514	3.9965
0.4	335.1496	228.1453	115.9572	85.1378	5.4117	4.0758
0.5	375.2046	230.8894	134.1621	86.6851	6.2426	4.1712
0.6	375.9160	233.4550	155.0191	88.2589	7.2256	4.2789
0.7	376.7536	235.9023	174.0783	89.8138	8.3328	4.3954
0.8	377.7159	238.2882	190.4021	91.3311	9.1583	4.5177
0.9	378.8012	240.6545	208.1551	92.8075	10.0348	4.6431
1	380.0075	243.0293	212.9974	94.2469	10.9912	4.7698

Table 6.9: Critical temperature (ΔT_{cr}) of the skew sandwich plate for two imperfection modes under a uniform temperature rise ($a/h = 100, h_2/h = 0.5, t/l_1 = 0.1, l_2/l_1 = 2, V_{CNT}^* = 0.17, \theta_{hc} = 30^\circ, UD$)

BC	Imperfection mode	Skew Angle (ψ)	Imperfection amplitude, (μ)			
			0.2	0.5	1	
SSSS	S	0°	4.2731	6.2426	10.9912	
		15°	4.3471	6.3324	11.4223	
		30°	4.6726	6.7263	13.1141	
		45°	5.7963	8.1114	15.8256	
	L2	0°	3.9367	4.1712	4.7698	
		15°	4.0094	4.2458	4.8497	
		30°	4.3270	4.5734	5.2069	
		45°	5.4113	5.7007	6.4531	
	CCCC	S	0°	14.9861	16.5697	21.3569
			15°	15.1139	16.7048	21.9000
			30°	15.6942	17.3278	22.7907
			45°	17.7590	19.5757	25.6078
L2		0°	14.8571	15.6966	17.8209	
		15°	14.9847	15.8291	17.9708	
		30°	15.5620	16.4311	18.6500	
		45°	17.6112	18.5795	21.0714	

Table 6.10: The effect of CNT distribution pattern in facings on critical temperature parameter (ΔT_{cr}) for the skew sandwich plate for uniform temperature rise ($a/h = 100, h_2/h = 0.5, t/l_1 = 0.1, l_2/l_1 = 2, V_{CNT}^* = 0.17, \theta_{hc} = 30^\circ, UD$)

V_{CN}^*	Skew angle (ψ)	SSSS			CCCC		
		UD	FGX	FGO	UD	FGX	FGO
0.12	0°	3.6776	3.8505	3.7176	14.0425	14.7135	14.1752
	15°	3.7396	3.9123	3.7831	14.1506	14.8198	14.2892
	30°	4.0124	4.1854	4.0706	14.6452	15.3099	14.8099
	45°	4.9607	5.1403	5.0643	16.4386	17.1070	16.6883
0.17	0°	3.8868	4.1398	3.9796	14.6793	15.6440	15.0034
	15°	3.9592	4.2136	4.0568	14.8060	15.7710	15.1377
	30°	4.2748	4.5365	4.3924	15.3785	16.3498	15.7445
	45°	5.3503	5.6438	5.5297	17.4075	18.4258	17.8868
0.28	0°	4.3567	4.8778	4.6220	16.4290	18.3765	17.4000
	15°	4.4156	4.9428	4.6873	16.5301	18.4856	17.5105
	30°	4.6769	5.2319	4.9766	16.9964	18.9929	18.0214
	45°	5.6031	6.2603	5.9981	18.7198	20.8882	19.9113

Table 6.11: Influence of cell angle and skew angle on critical temperature parameter (ΔT_{cr}) for a sandwich skew plate ($a/h = 100, t/l_1 = 0.1, V_{CNT}^* = 0.17, UD$) for uniform temperature rise

Skew Angle (ψ)	θ_{hc}	l_2/l_1							
		SSSS				CCCC			
		1.5	2	2.5	3	1.5	2	2.5	3
0°	-30°	3.9089	3.9074	3.9064	3.9057	14.6565	14.6539	14.6527	14.6523
	-15°	3.9004	3.8989	3.8980	3.8975	14.5774	14.5787	14.5801	14.5814
	15°	3.8877	3.8841	3.8826	3.8820	14.6065	14.5891	14.5820	14.5790
	30°	3.8904	3.8868	3.8858	3.8858	14.7193	14.6793	14.6616	14.6528
15°	-30°	3.9835	3.9810	3.9794	3.9783	14.7892	14.7846	14.7821	14.7807
	-15°	3.9773	3.9744	3.9726	3.9714	14.7144	14.7128	14.7123	14.7123
	15°	3.9648	3.9588	3.9560	3.9545	14.7428	14.7205	14.7107	14.7060
	30°	3.9650	3.9592	3.9572	3.9567	14.8502	14.8060	14.7863	14.7763
30°	-30°	4.3049	4.2987	4.2945	4.2915	15.3790	15.3662	15.3581	15.3525
	-15°	4.3092	4.3002	4.2944	4.2904	15.3239	15.3099	15.3013	15.2955
	15°	4.3002	4.2837	4.2750	4.2698	15.3554	15.3119	15.2904	15.2782
	30°	4.2900	4.2748	4.2683	4.2651	15.4418	15.3785	15.3497	15.3345
45°	-30°	5.3842	5.3659	5.3537	5.3449	17.4263	17.3886	17.3634	17.3453
	-15°	5.4242	5.3953	5.3767	5.3637	17.4339	17.3813	17.3472	17.3235
	15°	5.4383	5.3872	5.3591	5.3414	17.5021	17.3910	17.3313	17.2944
	30°	5.3973	5.3503	5.3281	5.3157	17.5349	17.4075	17.3470	17.3129

Table 6.12: Influence of type of core to plate thickness on critical temperature parameter for skew sandwich plate ($a/h = 100, t/l_1 = 0.1, l_2/l_1 = 2, V_{CNT}^* = 0.17, UD$)

θ_{hc}	Skew Angle (ψ)	SSSS			CCCC		
		$h_2/h = 0.2$	$h_2/h = 0.5$	$h_2/h = 0.8$	$h_2/h = 0.2$	$h_2/h = 0.5$	$h_2/h = 0.8$
-30°	0°	2.7485	3.9074	5.6879	10.2791	14.6539	21.2134
	15°	2.7984	3.9810	5.8218	10.3673	14.7846	21.4650
	30°	3.0149	4.2987	6.3841	10.7622	15.3662	22.5411
	45°	3.7477	5.3659	8.2009	12.1480	17.3886	26.0705
-15°	0°	2.7461	3.8989	5.6429	10.2448	14.5787	21.0916
	15°	2.7961	3.9744	5.7949	10.3330	14.7128	21.3778
	30°	3.0129	4.3002	6.4375	10.7283	15.3099	22.6077
	45°	3.7467	5.3953	8.5228	12.1140	17.3813	26.6320
15°	0°	2.7464	3.8841	5.4630	10.2537	14.5891	20.9787
	15°	2.7965	3.9588	5.6060	10.3420	14.7205	21.2327
	30°	3.0135	4.2837	6.2359	10.7378	15.3119	22.3884
	45°	3.7484	5.3872	8.3862	12.1260	17.3910	26.4200
30°	0°	2.7499	3.8868	5.4231	10.3046	14.6793	20.9661
	15°	2.7999	3.9592	5.5420	10.3928	14.8060	21.1690
	30°	3.0166	4.2748	6.0749	10.7885	15.3785	22.1207
	45°	3.7512	5.3503	7.9404	12.1793	17.4075	25.5923

6.4 Thermal Post-buckling Analysis

Thermal post-buckling is the analysis of structural components or systems under thermal loading after buckling. This section presents the thermal post-buckling analysis of an imperfect sandwich plate.

6.4.1 Validation Study

Firstly, two comparison studies are performed to explain the present model's efficacy for non-linear post-buckling analysis.

- (a) The post-buckling path of a CCCC skew plate ($\psi = 45^\circ, E = 1\text{GPa}, \nu = 0.3, \alpha = 10^{-6}/^\circ\text{C}$) illustrated in Figure 6.5, using the present approach, matches well with that of Prakash et al. (2008) were obtained using the deformable finite element approach. In this case, the temperature is normalised $T^* = T_{cr}E\alpha L^2h/(\pi^2D)$ with the flexural rigidity $D = Eh^3/12(1 - \nu^2)$.

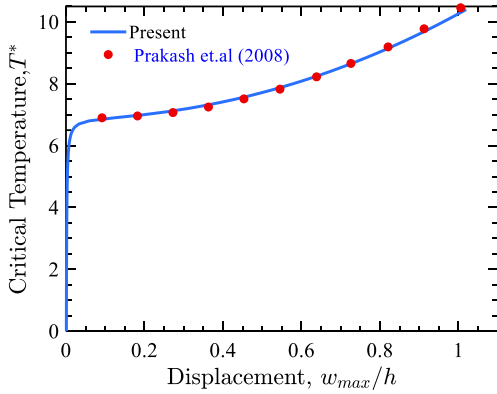


Figure 6.5: A comparison of thermal post-buckling equilibrium path of CCCC isotropic square plate.

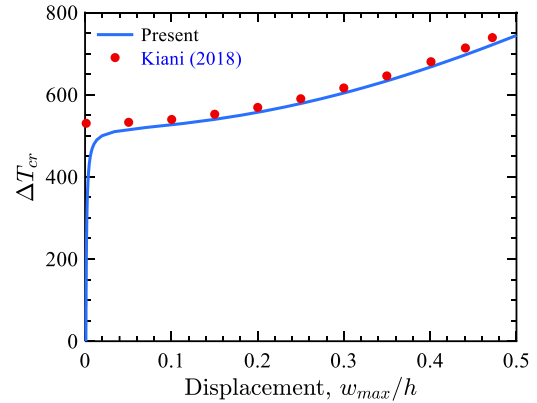


Figure 6.6: A comparison of the post-buckling behavior of a $[0/90^\circ]_s$ laminated plates. ($a/b = 1, a/h = 30$)

- (b) Secondly, symmetric laminated $[0/90^\circ]_s$ and temperature-dependent properties are considered for comparison, as shown in Figure 6.6 The following expressions can be used to describe how strongly temperature affects the material properties of the layers:

$$E_{11}(T) = 40 \times 10^9(1 - 0.5 \times 10^{-3}(T - T_0))\text{Pa}, E_{22}(T) = 1 \times 10^9(1 - 0.2 \times 10^{-3}(T - T_0))\text{Pa}$$

$$G_{13}(T) = 0.5 \times 10^9(1 - 0.2 \times 10^{-3}(T - T_0))\text{Pa}, G_{23}(T) = 0.2 \times 10^9(1 - 0.2 \times 10^{-3}(T - T_0))\text{Pa}$$

$$\alpha_{11}(T) = 1 \times 10^{-6}(1 + 0.5 \times 10^{-3}(T - T_0))1/\text{K}, \alpha_{22}(T) = 10 \times 10^{-6}(1 + 0.5 \times 10^{-3}(T - T_0))1/\text{K}$$

$$\nu_{12} = 0.25$$

The obtained results are very close to those of [Kiani \(2018\)](#) and are obtained using an eigenvalue problem solution while present work based on IGA with refined higher order theory.

6.4.2 Thermal Post-Buckling of Square Sandwich Plate

In the previous section, the numerical technique used for linear analysis of plates was found to be efficient. In this section, the same numerical technique is extended to study the non-linear post-buckling behaviour of the square sandwich plate. In this section, the parametric study of the square sandwich plate's thermal post-buckling is presented in detail.

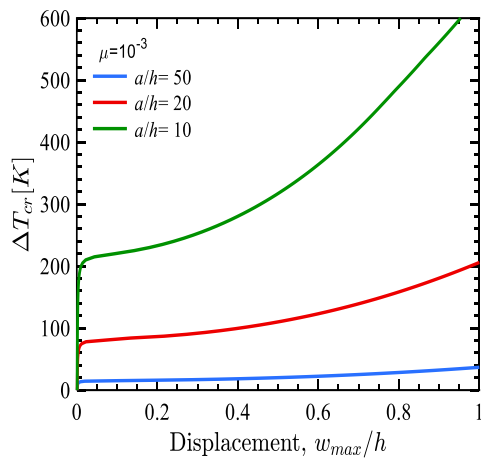


Figure 6.7: Influence of width-to-plate thickness ratio of a sandwich plate on post-buckling behaviour subjected to uniform temperature rise ($h_2/h = 0.5$, $t/l_1 = 0.1$, $l_2/l_1 = 2$, $V_{CNT}^* = 0.17$, $\theta_{hc} = 30^\circ$, UD,SSSS)

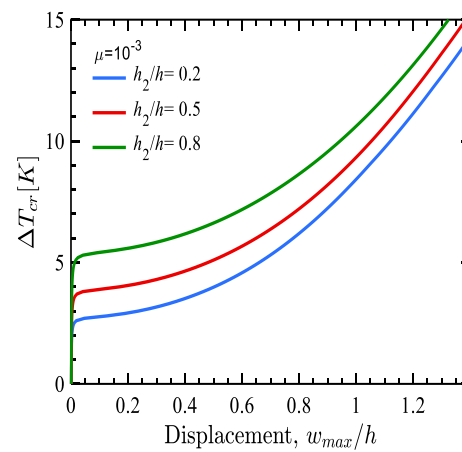


Figure 6.8: Influence of core to a plate thickness of a square sandwich plate on post-buckling behaviour subjected to uniform temperature rise ($a/h = 100$, $V_{CNT}^* = 0.17$, $\theta_{hc} = 30^\circ$, $t/l_1 = 0.1$, $l_2/l_1 = 2$, SSSS)

[Figure 6.7](#) presents the thermal post-buckling of plates with different a/h ratios. It is shown that the critical buckling temperature of sandwich plates increases as the a/h ratio decreases. This is accepted since, with increasing the thickness, the flexural rigidity of the plate increases. [Figure 6.8](#) indicates the effect of core thickness to plate thickness ratio on the square sandwich plate's thermal post-buckling equilibrium path with simply supported (SSSS) boundary conditions. UD of face sheets are considered for the sake of comparison. It is observed from

the results that the critical buckling temperature of the sandwich plate may be enhanced by increasing the core-to-thickness ratio where the total thickness of the plate is constant.

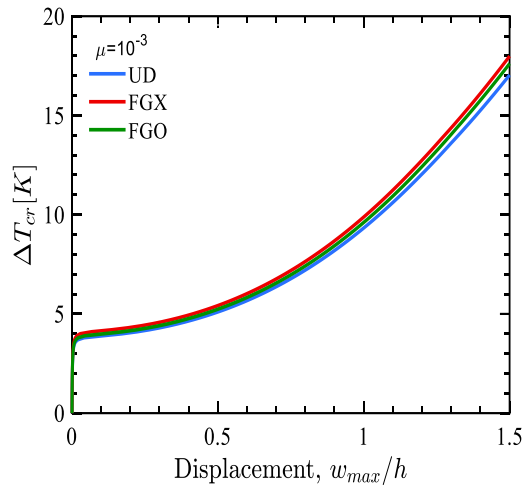


Figure 6.9: Influence of CNT distribution in the face sheets of a square sandwich plate on post-buckling behaviour subjected to uniform temperature rise ($a/h = 100, h_2/h = 0.5, t/l_1 = 0.1, l_2/l_1 = 2, \theta_{hc}=30^\circ, V_{CNT}^* = 0.17, SSSS$)

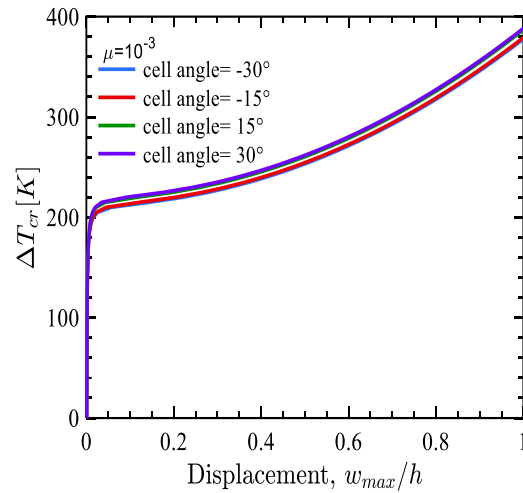


Figure 6.10: Influence of core auxeticity on a square sandwich plate consists of isotropic face sheets on post-buckling behaviour subjected to thermal load ($UD, V_{CNT}^* = 0.17, t/l_1 = 0.1, l_2/l_1 = 2, SSSS$)

Figure 6.9 shows the Influence of CNT distribution in the face sheets of a square sandwich plate on post-buckling behaviour subjected to uniform temperature rise. The figure shows that the thermal post-buckling equilibrium paths of sandwich plates with UD, FG-X, and FG-O face sheets are approximately the same.

The core angle in auxetic materials is a critical parameter influencing their unique mechanical properties and behaviour. In Figure 6.10, four cell angles are considered for comparison in the present studies. As the cell angle increases, the post-buckling strength increases.

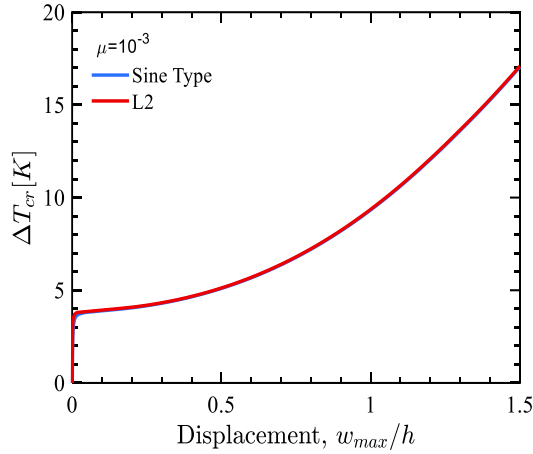


Figure 6.11: Influence of types of imperfections of a sandwich plate on post-buckling behaviour subjected to uniform temperature rise ($a/h = 100, h_2/h = 0.5, t/l_1 = 0.1, l_2/l_1 = 2, V_{CNT}^* = 0.17, \theta_{hc} = 30^\circ$)

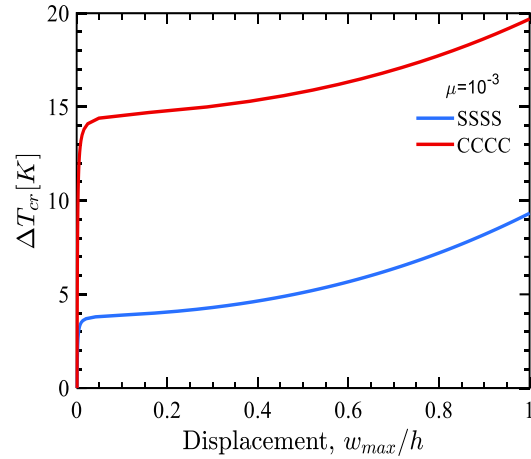


Figure 6.12: Influence of boundary conditions of the skew sandwich plate on post-buckling behaviour subjected to thermal load ($a/h = 100, h_2/h = 0.5, V_{CNT}^* = 0.17, \theta_{hc} = 30^\circ, t/l_1 = 0.1, l_2/l_1 = 2$)

The sinusoidal and L2-type imperfections on a plate can have significant post-buckling effects, influencing how the plate behaves after it has experienced buckling. [Figure 6.11](#) shows the post-buckling behaviour of a square sandwich plate under the two different types of initial imperfections, i.e., sine type and L2 type. It is observed from the figure that thermal post-buckling equilibrium paths of sandwich plates with sine type and L2 type imperfections are approximately the same due to the similar shape of imperfections. The effect of boundary conditions on the sandwich plate, including an auxetic core, is shown in [Figure 6.12](#) As expected, the critical buckling temperature of CCCC plates is higher than that of SSSS plates. This observed trend may be ascribed to an edge clamped being stiffer than an edge just supported.

6.4.3 Thermal Post-Buckling of Skew Sandwich Plate

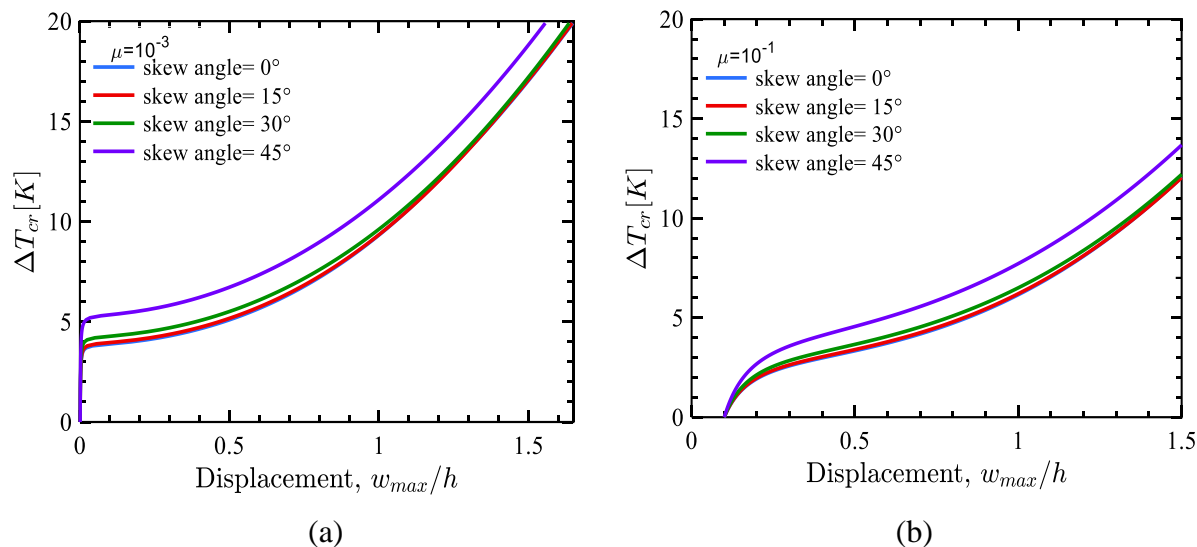


Figure 6.13: Influence of skew angle on the post-buckling path of a sandwich skew plate under uniform temperature rise ($a/h = 100$, $h_2/h = 0.5$, $t/l_1 = 0.1$, $l_2/l_1 = 2$, $V_{CNT}^* = 0.17$, $\theta_{hc} = 30^\circ$, UD, SSSS)

Figures 6.13a and 6.13b indicate the effect of skew angles on the sandwich plate's post-buckling behaviour with two magnitudes of initial imperfections and SSSS BCs. It is observed from the figures that the post-buckled strength can be improved by increasing the skewness of the plate, as mentioned earlier. Figure 6.14a shows the influence of imperfection amplitude on the load-deflection path of the skew sandwich plate. It is clear from the results that as the imperfection amplitude increases, the post-buckling strength decreases accordingly. Similar behaviours are observed in L2-type imperfection, as shown in Figure 6.14b. The effect of the CNT distribution pattern on the thermal post-buckling behaviour of skew sandwich plates in Figure 6.15a shows that there is no substantial change in the post-buckling strength with variations in the CNT pattern. According to the findings illustrated in Figure 6.15b, an increase in the volume fraction of carbon nanotubes results in a higher critical temperature of the plate. This phenomenon occurs because the carbon nanotubes have a very high value of Young's modulus, and the face sheets' stiffness is directly proportional to the CNT volume fraction value. Figure 6.16 includes the effect of core thickness to total thickness ratio on the skew sandwich plate's non-linear stability characteristics with SSSS BCs. It is observed from the figure that the buckling strength may also be enhanced by modifying the core-to-thickness ratio while keeping the overall thickness the same. It has been observed that as the relative thickness of the core increases, the buckling load parameter also increases because the rate of change of

geometric stiffness with a change in core thickness is higher than that of the overall stiffness of the sandwich plate.

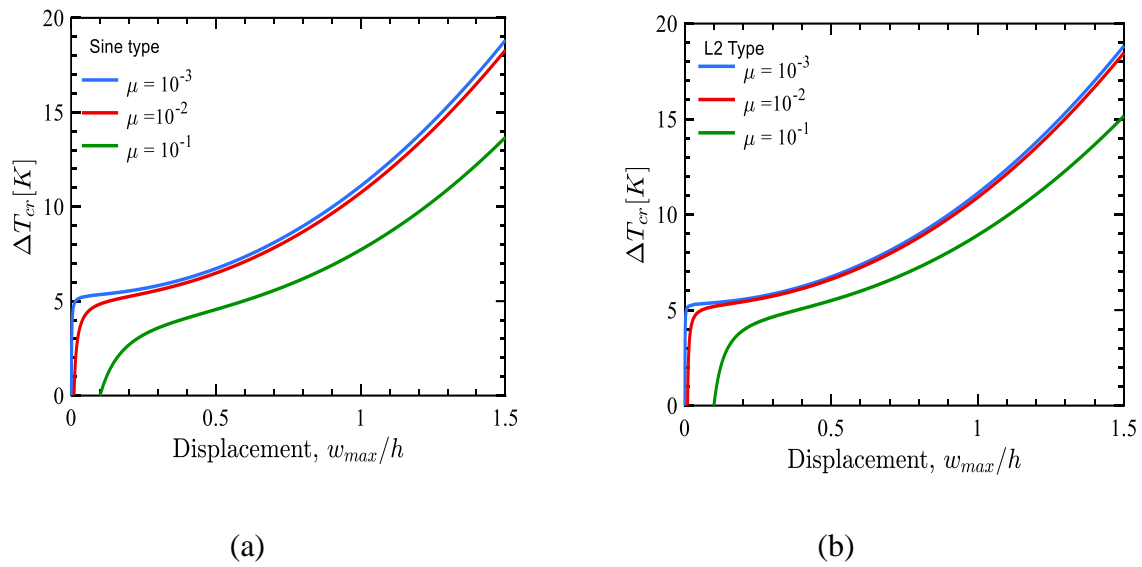


Figure 6.14: Influence of sine type and L2 type imperfections on post-buckling paths of a skew sandwich plate ($a/h = 100, h_2/h = 0.5, t/l_1 = 0.1, l_2/l_1 = 2, V_{CNT}^* = 0.17, \theta_{hc} = 30^\circ, \psi = 45^\circ, UD, SSSS$)

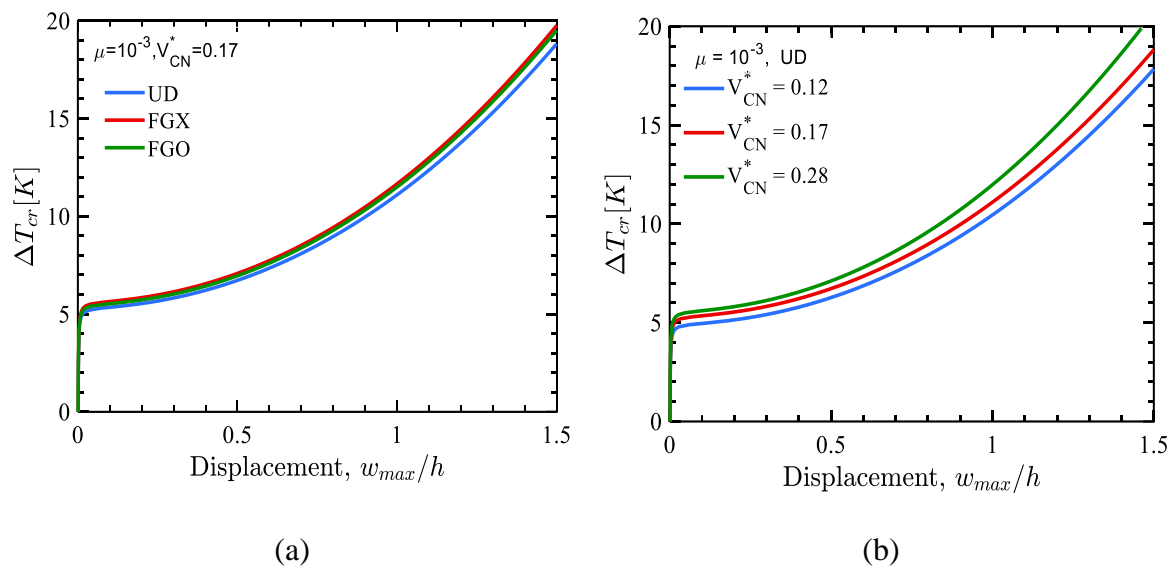


Figure 6.15: The effect of CNT distribution in the face sheets of a skew sandwich plate on post-buckling behaviour subjected to uniform temperature rise ($a/h = 100, h_2/h = 0.5, t/l_1 = 0.1, l_2/l_1 = 2, \theta_{hc} = 30^\circ, \psi = 45^\circ, SSSS$)

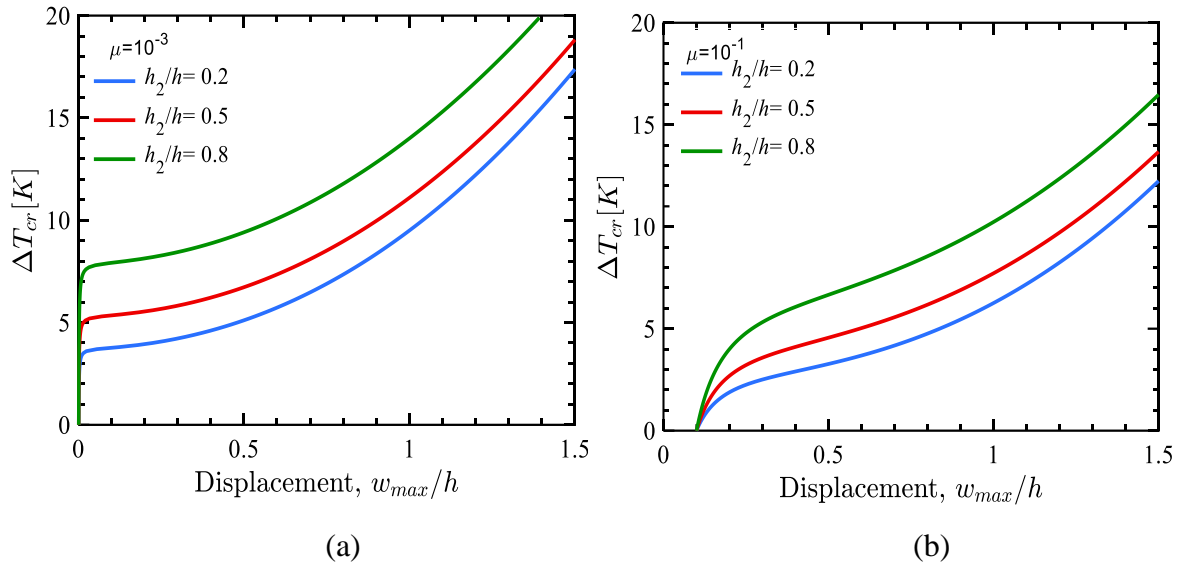


Figure 6.16: Effect of core-to-plate thickness ratio of a skew sandwich plate on post-buckling behaviour subjected to uniform temperature rise ($a/h = 100, h_2/h = 0.5, t/l_1 = 0.1, l_2/l_1 = 2, V_{CNT}^* = 0.17, \theta_{hc} = 30^\circ, \psi = 45^\circ, \text{UD, SSSS}$)

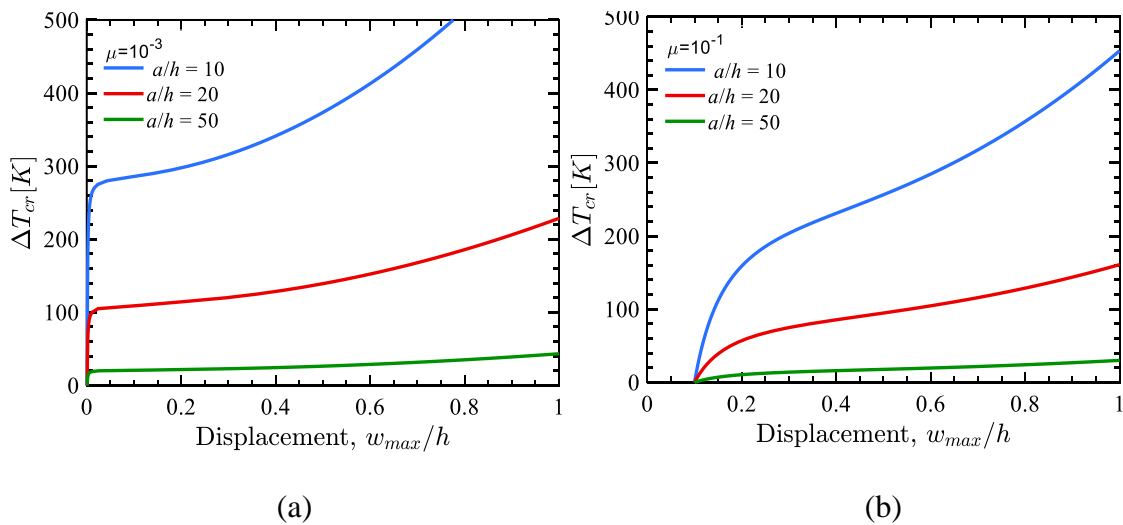


Figure 6.17: Influence of width to a plate thickness of a skew sandwich plate on post-buckling behaviour subjected to uniform temperature rise ($a/h = 100, h_2/h = 0.5, t/l_1 = 0.1, l_2/l_1 = 2, V_{CNT}^* = 0.17, \theta_{hc} = 30^\circ, \psi = 45^\circ, \text{UD, SSSS}$)

Figure 6.17 presents the non-linear thermomechanical stability behaviour of skew sandwich plates with various a/h ratios. It is shown that the critical temperature of sandwich plates increases as the a/h ratio decreases because, with the increase in the thickness, the flexural

rigidity of the plate increases. The cell angle in auxetic core geometry is a critical parameter influencing their unique mechanical properties and behaviour.

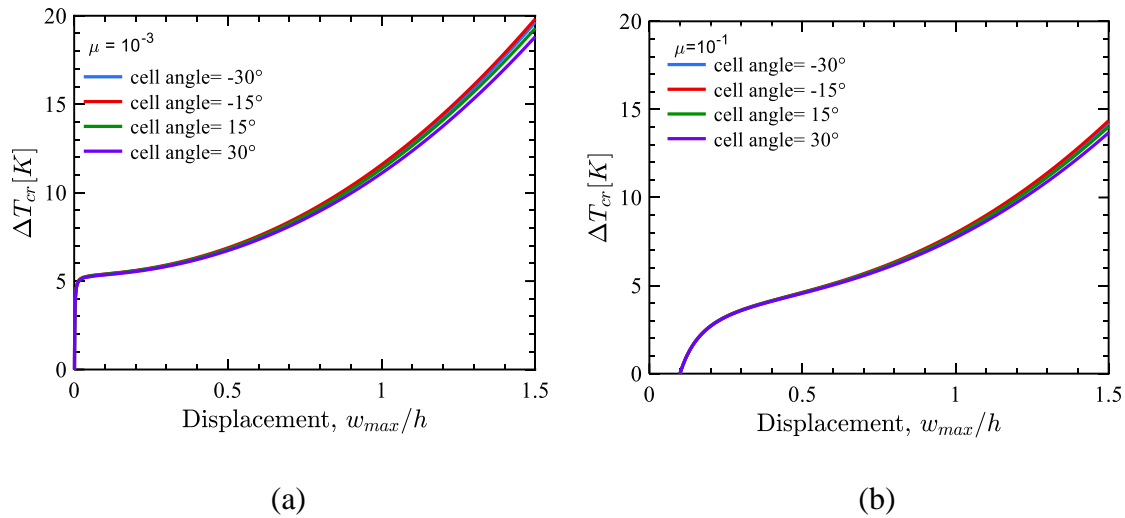


Figure 6.18: Influence of core auxeticity on a skew sandwich plate on post-buckling behaviour subjected to thermal load ($a/h = 100, h_2/h = 0.5, t/l_1 = 0.1, l_2/l_1 = 2, V_{CNT}^* = 0.17, \psi = 45^\circ, UD, SSSS$)

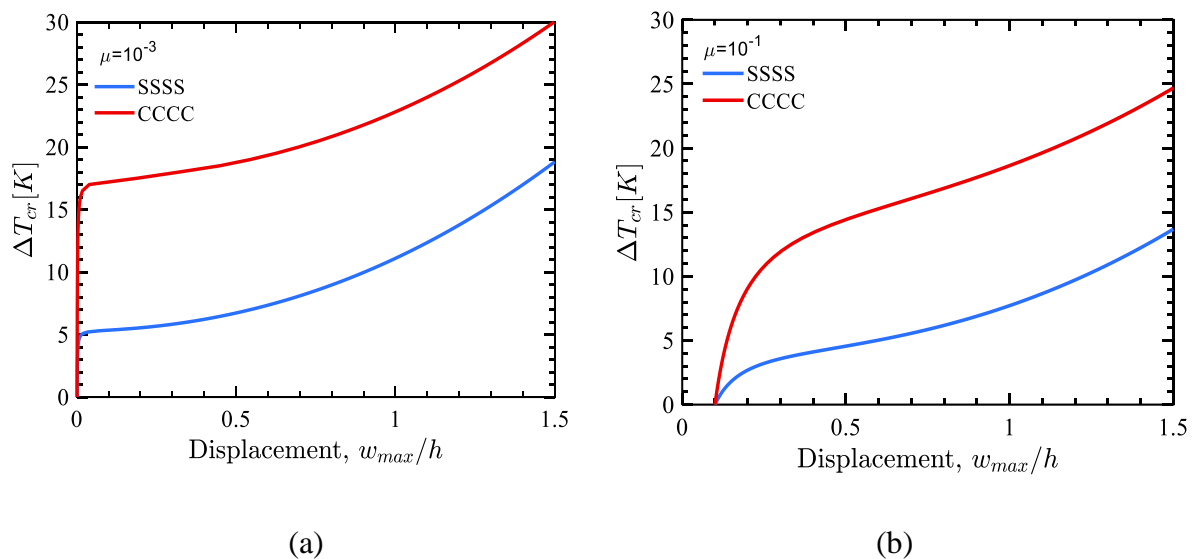


Figure 6.19: Influence of boundary conditions of the skew sandwich plate on post-buckling behaviour subjected to uniform temperature rise ($a/h = 100, h_2/h = 0.5, t/l_1 = 0.1, l_2/l_1 = 2, V_{CNT}^* = 0.17, \theta_{hc} = 30^\circ, \psi = 45^\circ, UD$)

Figure 6.18 considers the thermomechanical stability paths of skew sandwich plates with auxetic cores for four different cell angles. It is apparent from the results that the cell angle in the core geometry does not contribute towards the buckling strength. The impact of boundary conditions on the skew sandwich plate, including a re-entrant auxetic core, is shown in Figure 6.19. As expected, the critical buckling temperature of CCCC plates is higher than that of SSSS

plates. This observed trend may be ascribed to an edge clamped being stiffer than an edge just simply supported.

6.5 Summary

This study analyses thermomechanical stability characteristics of initially imperfect sandwich plates made of FGCNTRC facings and re-entrant auxetic core. The material properties for carbon nanotubes (CNTs) at different temperature values are interpolated using polynomial interpolation, and the resultant material properties are evaluated using the extended rule of mixtures with the efficiency parameters. The system of equations is formulated using a non-polynomial theory, incorporating the von Karman assumptions. Firstly, validation studies are conducted on linear/non-linear thermal post-buckling behaviour of perfect isotropic/laminated/sandwich plates to ascertain the efficacy of the present methodology. Subsequently, parametric studies are conducted to explore the effects of CNT patterns in facings, core auxeticity, skew angle and boundary conditions.

New findings on the influence of the type and magnitude of global geometric imperfection and geometrical parameters of the auxetic core are reported for the first time. The following observations have been made from the present work:

- (a) The magnitude of the geometrical imperfection has a significant influence on the post-buckling strength of the sandwich plate.
- (b) As the sandwich laminate's width-to-thickness ratio increases, post-buckling deflection is found to be more at the same temperature.
- (c) The buckling strength of the FGCNTRC skew sandwich plates in a thermal environment change significantly with a variation in the skew angle.
- (d) The post-buckling strength of the sandwich plate can be improved by increasing the volume fraction of CNTs in the face sheets.
- (e) The FG-X pattern of CNTs in facings results in higher buckling temperature and less post-buckling deflection in comparison to other distribution patterns.
- (f) The critical buckling strength of the sandwich plates may also be enhanced by increasing the core thickness ratio to the plate's total thickness.

- (g) The critical buckling temperature of the skew sandwich plates with a positive cell angle of auxetic core and negative Poisson's ratio is slightly lower than those with a negative cell inclination angle.

Non-linear vibration analysis of sandwich plate in thermal environment

7.1 Introduction

This chapter investigates the linear and non-linear vibration behaviours of sandwich plates with auxetic cores having tunable material properties. The accuracy of the isogeometric analysis (IGA) method with non-polynomial higher-order theory and in-house MATLAB code has been established for the linear and non-linear analyses of isotropic, laminated and sandwich plates in Chapter 5. Section 7.2 explores the same numerical technique and the in-house MATLAB code for the linear vibration analysis of isotropic, laminated, functionally graded carbon nanotube-reinforced composite (FGCNTRC) and sandwich plates in a thermal environment. Section 7.3 investigates the effect of geometrical parameters on the non-linear vibration characteristics of functionally graded carbon nanotube-reinforced composite (FGCNTRC) and sandwich plates. The chapter concludes with a summary of observations from the present numerical work in Section 7.4. The geometrical parameters and CNTs distribution pattern of sandwich plates are presented in [Figures 7.1](#) and [7.2](#), respectively. The material properties considered in the present investigation have already been discussed in Chapter 6.

Unless otherwise stated, the following numerical studies utilise Poly methyl methacrylate (PMMA) as the matrix. In Chapter 6, CNTs are employed as reinforcements, and their properties are given in [Table 7.1](#)

7.1.1 Boundary conditions

The different types of edge constraints for the plate are given as:

Simply supported: (SSSS) : $\{ u_0 = v_0 = w_0 = 0 \text{ at } x = 0, a \text{ and } y = 0, b \}$

$$(S^1S^1S^1S^1): \begin{cases} v_0 = w_0 = \theta_y = 0 \text{ on } x = 0, a \\ u_0 = w_0 = \theta_x = 0 \text{ on } y = 0, b \end{cases}$$

Clamped support : (CCCC): $\begin{cases} u_0 = v_0 = w_0 = \theta_x = \theta_y = 0 \\ w_{0,x} = w_{0,y} = 0 \end{cases}$ All edges

Table 7.1: Temperature-dependent material properties for SWCNT(Zhu et al., 2012)

Temperature (K)	E_{11}^{CNT} (TPa)	E_{22}^{CNT} (TPa)	G_{12}^{CNT} (TPa)	α_{11}^{CNT} ($10^{-6}/K$)	α_{22}^{CNT} ($10^{-6}/K$)
300	5.6466	7.0800	1.9445	3.4584	5.1682
500	5.5308	6.9348	1.9643	4.5361	5.0189
700	5.4744	6.8641	1.9644	4.6677	4.8943

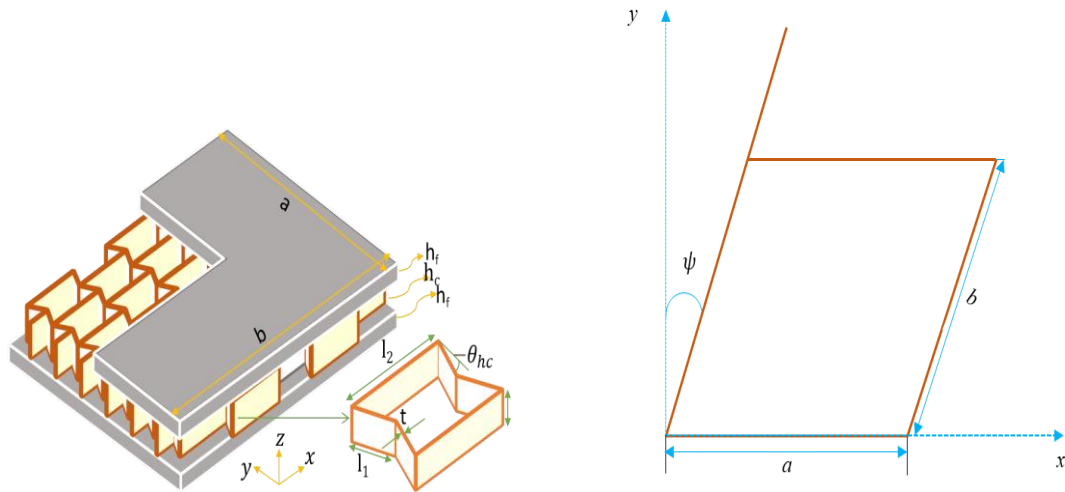
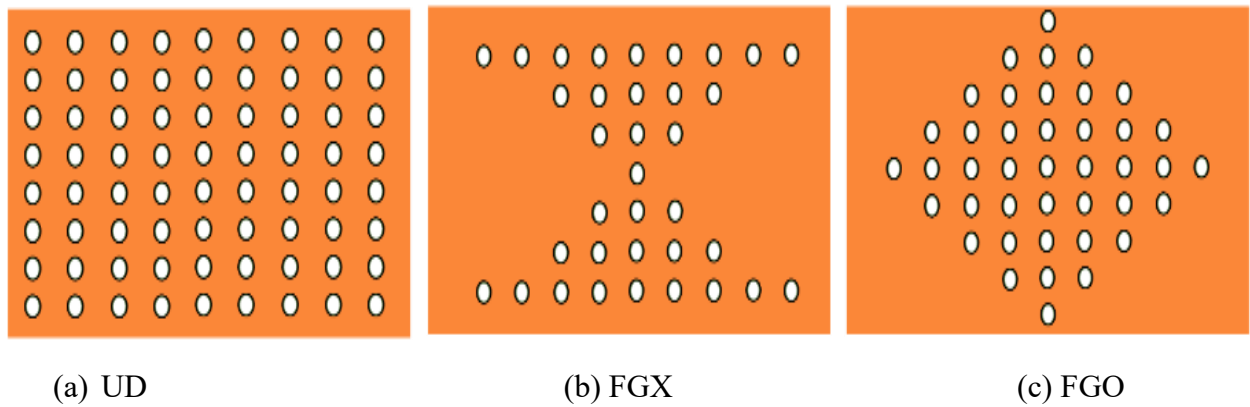


Figure 7.1: Geometrical parameters of the sandwich plate



(a) UD

(b) FGX

(c) FGO

Figure 7.2: CNT distribution pattern

7.2 Linear Vibration Analysis

Table 7.2: Convergence study of the influence of width-to-thickness ratio and CNT volume fraction on the non-dimensional natural frequency parameter $\bar{\omega} = \omega(a^2/h)\sqrt{\rho_m/E_m}$ for simply supported $S^1S^1S^1S^1$ FGCNTRC square plates.

a/h	p	n	NCP	V_{CN}^*									
				0.11			0.14			0.17			
				UD	FGX	FGO	UD	FGX	FGO	UD	FGX	FGO	
10	2	2	5×5	13.933	15.260	11.451	14.782	16.045	12.207	17.304	18.885	14.222	
		4	7×7	13.799	15.132	11.322	14.654	15.928	12.079	17.135	18.727	14.058	
		6	9×9	13.734	15.075	11.263	14.587	15.870	12.018	17.053	18.656	13.983	
			8	11×11	13.695	15.037	11.233	14.545	15.830	11.985	17.006	18.608	13.945
			10	13×13	13.673	15.012	11.216	14.520	15.803	11.967	16.978	18.578	13.925
			12	15×15	13.659	14.997	11.207	14.504	15.785	11.956	16.962	18.559	13.914
			14	17×17	13.651	14.987	11.200	14.494	15.773	11.949	16.951	18.547	13.906
			16	19×19	13.645	14.979	11.196	14.487	15.765	11.944	16.943	18.538	13.901
		3	3	7×7	13.662	15.002	11.209	14.507	15.790	11.958	16.965	18.565	13.916
			5	9×9	13.622	14.953	11.181	14.461	15.734	11.927	16.916	18.506	13.883
			7	11×11	13.620	14.950	11.180	14.458	15.730	11.925	16.913	18.501	13.881
			9	13×13	13.620	14.949	11.179	14.458	15.729	11.925	16.913	18.501	13.881
			11	15×15	13.619	14.949	11.179	14.457	15.729	11.924	16.913	18.501	13.880
			13	17×17	13.619	14.949	11.179	14.457	15.729	11.924	16.913	18.501	13.880
			15	19×19	13.619	14.949	11.179	14.457	15.729	11.924	16.913	18.501	13.880
			Zhu et al. (2012)	13.532	14.616	11.550	14.306	15.368	12.338	16.815	18.278	14.282	
20	2	2	5×5	17.833	20.568	13.828	19.464	22.322	15.105	22.044	25.408	17.049	
		4	7×7	17.555	20.262	13.607	19.171	22.006	14.866	21.699	25.030	16.775	
		6	9×9	17.433	20.137	13.504	19.044	21.881	14.757	21.546	24.876	16.645	
			8	11×11	17.384	20.083	13.466	18.991	21.822	14.716	21.486	24.808	16.599
			10	13×13	17.361	20.055	13.449	18.965	21.791	14.697	21.457	24.774	16.578
			12	15×15	17.347	20.039	13.439	18.950	21.774	14.686	21.441	24.755	16.566
			14	17×17	17.339	20.030	13.434	18.941	21.763	14.679	21.431	24.743	16.559
			16	19×19	17.334	20.023	13.430	18.935	21.755	14.675	21.424	24.735	16.554
		3	3	7×7	17.350	20.044	13.441	18.953	21.779	14.687	21.444	24.761	16.567
			5	9×9	17.314	20.001	13.416	18.913	21.73	14.659	21.400	24.707	16.536
			7	11×11	17.312	19.998	13.414	18.910	21.727	14.657	21.398	24.704	16.535
			9	13×13	17.312	19.998	13.414	18.910	21.726	14.657	21.397	24.704	16.535
			11	15×15	17.312	19.998	13.414	18.910	21.726	14.657	21.397	24.703	16.534
			13	17×17	17.312	19.998	13.414	18.910	21.726	14.657	21.397	24.703	16.534
			15	19×19	17.312	19.998	13.414	18.91	21.726	14.657	21.397	24.703	16.534
			Zhu et al. (2012)	17.355	19.939	13.523	18.921	21.642	14.784	21.456	24.764	16.628	

Since no studies are available on the vibration behaviour of sandwich plates with auxetic cores, validation studies are presented for single-layered FGCNTRC plates. In all the validation studies, FGCNTRC is made up of CNTs and the matrix PmPV (Han & Elliott, 2007) and its properties are given by : $v_m = 0.34$, $\rho_m = 1.15 \text{ g/cm}^3$, and $E_m = 2.1 \text{ GPa}$ at room temperature (300 K). For this specific case, the considered volume fractions and related efficiency parameters are: $V_{CNT}^* = 0.11$ with $\eta_1 = 0.149$ and $\eta_2 = 0.934$; $V_{CNT}^* = 0.14$ with $\eta_1 = 0.150$

and $\eta_2 = 0.941$; and $V_{CNT}^* = 0.17$ with $\eta_1 = 0.149$ and $\eta_2 = 1.381$. Besides, the assumptions $\eta_2 = \eta_3$ and $G_{12} = G_{13} = G_{23}$ are also made.

Non-dimensional natural frequency parameter $\bar{\omega} = \omega(a^2/h)\sqrt{\rho_m/E_m}$ for simply supported FGCNTRC square plates subjected to the thermal load are tabulated in [Table 7.2](#) for different CNT volume fractions and CNT distributions through thickness. The results are compared to those given by [Zhu et al. \(2012\)](#), and they agree well. The study is conducted for two distinct orders of the B-spline curve, $p=2$ and $p=3$, where p is the order of the curve, and it is noticed that the results converge faster and require a lesser number of knot insertions as the order of the curve increases. Hence, order, $p=3$, is employed in all the following investigations. The results exhibit convergence when 13-knot insertions are made for a third-order approximation. Therefore, the same number of knot insertions is employed for all the subsequent investigations.

Table 7.3: First six non-dimensional natural frequency parameter $\bar{\omega} = \omega(a^2/h)\sqrt{\rho_m/E_m}$ of simply supported functionally graded reinforced composite plates with CNT volume fraction, ($V_{CN}^* = 0.11, a/h = 50, S^1S^1S^1S^1$).

Results	CNT	$\bar{\omega}$					
		$\bar{\omega}_1$	$\bar{\omega}_2$	$\bar{\omega}_3$	$\bar{\omega}_4$	$\bar{\omega}_5$	$\bar{\omega}_6$
Present	UD	19.152	23.266	34.032	51.903	70.007	72.110
Zhu et al. (2012)(ANSYS)		19.184	23.310	34.272	52.770	70.363	72.395
Zhu et al. (2012)		19.223	23.408	34.669	54.043	70.811	72.900
Phung-Van et al. (2015)		19.093	22.968	34.017	53.664	70.808	72.569
Fazzolari (2018)		19.154	23.273	34.056	51.9641	70.019	72.128
Present	FGX	22.832	26.554	36.855	54.653	79.237	82.467
Zhu et al. (2012)(ANSYS)		22.910	26.660	37.016	54.912	79.630	82.297
Zhu et al. (2012)		22.984	26.784	37.59	56.964	83.150	84.896
Phung-Van et al. (2015)		22.880	26.183	36.238	55.066	83.604	83.703
Fazzolari (2018)		22.899	26.621	36.939	54.783	79.413	82.321
Present	FGO	14.383	19.355	31.059	49.312	52.421	55.207
Zhu et al. (2012)		14.290	19.274	31.013	49.326	52.569	55.362
Zhu et al. (2012) (ANSYS)		14.302	19.373	31.615	51.370	53.035	55.823
Phung-Van et al. (2015)		14.153	19.154	31.710	52.422	52.616	55.123
Fazzolari (2018)		14.244	19.273	31.066	49.422	52.132	54.961

According to [Table 7.2](#), the UD and FGO CNTRC plates have a smaller natural frequency than the FGX CNTRC plates despite all three having the same volume fraction of CNT. This is due to the distribution of reinforcements affecting the stiffness of the plates. The desired stiffness can be achieved by adjusting the distribution of CNTs along the thickness direction of the

plates. It can be inferred that placing reinforcements closer to the top and bottom is more effective at increasing plate stiffness than placing them near the mid-plane.

Table 7.4: First six dimensionless natural frequency parameters, $\bar{\omega} = \omega(a^2/h)\sqrt{\rho_m/E_m}$ of simply supported functionally graded reinforced composite plates with CNT volume fraction ($V_{CN}^* = 0.14$ $a/h = 50$, $S^1S^1S^1S^1$).

Results	CNT	$\bar{\omega}$					
		$\bar{\omega}_1$	$\bar{\omega}_2$	$\bar{\omega}_3$	$\bar{\omega}_4$	$\bar{\omega}_5$	$\bar{\omega}_6$
Present	UD	21.314	25.183	35.660	53.482	77.383	77.923
Zhu et al. (2012) (ANSYS)		21.311	25.192	35.866	54.320	77.629	79.482
Zhu et al. (2012)		21.354	25.295	36.267	55.608	78.110	80.015
Phung-Van et al. (2015)		21.290	24.933	35.678	55.280	78.110	80.087
Fazzolari (2018)		21.316	25.190	35.685	53.543	77.389	79.324
Present	FGX	25.427	28.979	39.104	57.010	82.032	90.68
Zhu et al. (2012) (ANSYS)		25.474	29.065	39.257	57.272	82.437	90.389
Zhu et al. (2012)		25.555	29.192	39.833	59.333	87.814	91.299
Phung-Van et al. (2015)		25.528	28.616	38.313	56.98	85.793	92.220
Fazzolari (2018)		25.494	29.049	39.196	57.155	82.231	90.413
Present	FGO	15.917	20.59	32.011	50.191	58.079	60.621
Zhu et al. (2012) (ANSYS)		15.788	20.469	31.918	50.145	58.237	60.782
Zhu et al. (2012)		15.80	20.563	32.509	52.184	58.748	61.277
Phung-Van et al. (2015)		15.70	20.455	32.840	53.668	58.490	60.805
Fazzolari (2018)		15.762	20.487	31.992	50.268	57.840	60.420

Tables 7.3-7.5 present the initial six dimensionless frequency parameters of simply supported FGCNTRC plates. The outcomes of the present model have been compared with those of Zhu et al. (2012) obtained by finite element (FE) analysis, the commercial software ANSYS, the Ritz method and IGA formulations found in the literature. The present results have been observed to match well with those reported in the existing literature.

Table 7.5: First six dimensionless natural frequency parameters $\bar{\omega} = \omega(a^2/h)\sqrt{\rho_m/E_m}$ of simply supported functionally graded reinforced composite plates with CNT volume fraction, ($V_{CN}^* = 0.17 a/h = 50, S^1S^1S^1S^1$).

Results	CNT	$\bar{\omega}$					
		$\bar{\omega}_1$	$\bar{\omega}_2$	$\bar{\omega}_3$	$\bar{\omega}_4$	$\bar{\omega}_5$	$\bar{\omega}_6$
Present		23.604	28.805	42.360	64.785	86.370	89.031
Zhu et al. (2012) (ANSYS)	UD	23.649	28.865	42.667	65.880	86.830	89.403
Zhu et al. (2012)		23.697	28.987	43.165	67.475	87.385	90.031
Phung-Van et al. (2015)		23.528	28.440	42.362	67.018	87.328	89.569
Fazzolari (2018)		23.607	28.813	42.390	64.861	86.385	89.054
Present		28.176	33.077	46.512	69.506	101.097	101.681
Zhu et al. (2012) (ANSYS)	FGX	28.322	33.274	46.797	69.940	101.739	101.877
Zhu et al. (2012)		28.413	33.434	47.547	72.570	102.939	105.334
Phung-Van et al. (2015)		28.228	32.412	45.090	68.729	103.300	104.608
Fazzolari (2018)		28.267	33.170	46.636	69.703	101.370	101.534
Present		17.662	23.802	38.239	60.746	64.506	67.951
Zhu et al. (2012) (ANSYS)	FGO	17.529	23.659	38.109	60.652	64.580	68.01
Zhu et al. (2012)		17.544	23.783	38.855	63.179	65.154	68.579
Phung-Van et al. (2015)		17.398	23.754	39.579	64.620	65.570	67.836
Fazzolari (2018)		17.488	23.713	38.2919	60.968	64.147	67.652

Table 7.6: Non-dimensional natural frequency parameter $\bar{\omega} = \omega(a^2/h)\sqrt{\rho_m/E_m}$ for simply supported various types of FGCNTRC plates in different temperature environments ($V_{CN}^* = 0.12 a/h = 10, S^1S^1S^1S^1$).

Temperature	Mode	UD		FGX		FGO	
		Present	Lei et al. (2013)	Present	Lei et al. (2013)	Present	Lei et al. (2013)
300	1	12.3390	12.1261	13.4646	13.1289	10.2291	10.4535
	2	16.9248	16.5545	17.1629	17.1045	15.4485	15.3530
	3	17.0808	16.9835	17.1629	17.1045	17.0779	17.0365
500	1	11.1388	10.9644	12.0524	11.6675	9.2702	9.5378
	2	14.5740	14.4941	14.6441	14.5948	13.4858	13.4627
	3	14.5740	14.5494	14.6441	15.1371	14.5715	14.5394
700	1	9.5195	9.2518	10.1635	9.6982	7.9792	8.2728
	2	11.5345	11.5159	11.590	11.5519	11.0576	11.1033
	3	11.5345	11.8279	11.590	12.2867	11.5325	11.5090

Table 7.6 compares various types of FGCNTRC plates under different temperature conditions for simply supported FGCNTRC plates. The results obtained from this study show good agreement with the solutions provided by Lei et al. (2013)

Table 7.7: Comparison of the non-dimensional natural frequency parameter $\bar{\omega} = \omega a^2/h\sqrt{\rho_H/E_H}$ for sandwich plates with CNT-reinforced face sheets in a thermal environment with $a/b = 1$ and $a/h = 20$, $S^1S^1S^1S^1$ for various core-to-face sheet thicknesses and CNT volume fraction V_{CN}^* . The CNTs are assumed to be functionally graded, i.e., FGX.

h_c/h_f	Temperature	V_{CN}^*	$\bar{\omega}$	
			Present	Natarajan et al. (2014)
4	300	0.12	4.6229	4.6518
		0.17	4.9921	5.0381
		0.28	5.5927	5.6422
	500	0.12	4.4231	4.4425
		0.17	4.7899	4.8244
		0.28	5.3979	5.4238
6	300	0.12	4.8848	4.8992
		0.17	5.1527	5.1753
		0.28	5.6014	5.6278
	500	0.12	4.6557	4.6662
		0.17	4.9230	4.9408
		0.28	5.3796	5.3956

The study presented in Table 7.7 examines the natural frequency of sandwich plates with CNT-reinforced face sheets and homogeneous core (Ti-6Al-4V Titanium alloy). The properties of cores are: $\alpha_H = 7.5788(1 + 6.638 \times 10^{-4}T - 3.147 \times 10^{-6} T^2) \times 10^{-6} K^{-1}$, Young's modulus, $E_H = 122.56(1 - 4.586 \times 10^{-4} T)GPa$, Poisson's ratio $\nu_H = 0.29$, and mass density $\rho_H = 4429Kg/m^3$ in a thermal environment. The results obtained through this formulation are consistent with previous literature (Natarajan et al., 2014).

The study also shows the influence of varying factors, such as CNT volume fraction and core-to-face sheet thickness ratio, on the non-dimensional frequency parameters. As anticipated, the frequency decreases with increasing temperature while increasing volume fraction and core-to-face sheet thickness. This is due to the compressive forces generated by the temperature increase, significantly reducing the plate's overall stiffness. The plate's stiffness also reduces with temperature due to its temperature-dependent material properties.

Table 7.8: Influence of type of CNT distribution in face sheets on non-dimensional natural frequency parameter, $\bar{\omega} = \omega (a^2/h) \sqrt{\rho_c/E_c}$ for the sandwich plate at room temperature ($l_2/l_1 = 2$, $t/l_1 = 0.1$, $\theta_{hc} = 30$, $h_c/h_f = 2$ and $a/h = 50$, $S^1S^1S^1S^1$)

V_{CN}^*	Skew angle (ψ)	$S^1S^1S^1S^1$			CCCC		
		UD	FGX	FGO	UD	FGX	FGO
0.12	0°	5.9543	6.1232	5.7246	12.9903	13.4865	11.9628
	15°	6.0212	6.1894	5.7931	13.0758	13.5707	12.0508
	30°	6.3011	6.4666	6.0779	13.4381	13.9286	12.4225
	45°	7.1895	7.3521	6.9715	14.6402	15.1229	13.6388
0.17	0°	7.1993	7.4046	6.9235	15.6640	16.2639	14.4259
	15°	7.2896	7.4947	7.0158	15.7803	16.3796	14.5453
	30°	7.6635	7.8684	7.3961	16.2691	16.8671	15.0453
	45°	8.8283	9.0388	8.5669	17.8633	18.4655	16.6534
0.28	0°	8.9644	9.2342	8.6086	19.6018	20.3782	17.9676
	15°	9.0455	9.3180	8.6927	19.7047	20.4845	18.0752
	30°	9.3873	9.6715	9.0457	20.1433	20.9375	18.5326
	45°	10.4974	10.8209	10.1779	21.6238	22.4694	20.0572

Table 7.8 shows how the type of CNT distribution in face sheets affects the thermal buckling load of a sandwich plate with the auxetic core. The non-dimensional natural frequency parameter (ω) is shown for various CNT distributions, concentrations, and boundary conditions. The results indicate that increasing the CNT concentration in the face sheets improves non-dimensional natural frequency parameters, $\bar{\omega} = \omega (a^2/h) \sqrt{\rho_c/E_c}$ for a specific type of CNT distribution pattern. This is due to an increase in the effective elasticity modulus and overall stiffness of the plate. Non-dimensional natural frequencies are determined to be highest for the FGX type of distribution, followed by UD, and lowest for the FGO distribution for a given boundary condition, skew angle, and CNT volume fraction.

Table 7.9 shows the effect of the auxetic core, and it is observed from the results that the impact of cell angle is very minimal on the natural frequency of the sandwich plate. It is also observed from **Table 7.9** that as the cell wall thickness to the cell wall length ratio increases, the non-dimensional natural frequency parameter decreases. This is because the elastic modulus and stiffness of the auxetic honeycomb core will reduce with the rise of the cell wall angle.

Table 7.9: Influence of cell angle and skew angle on non-dimensional natural frequency parameter $\bar{\omega} = \omega (a^2/h)\sqrt{\rho_c/E_c}$ for a sandwich plate($t/l_1 = 0.1$, $h_c/h_f=2$, $a/h = 20$, $S^1S^1S^1S^1$) at room temperature .

Skew Angle (ψ)	θ_{hc}	t/L_1		
		0.05	0.1	0.2
0°	-30°	7.3963	7.3406	6.9467
	-15°	7.3021	7.2834	6.9140
	15°	7.2157	7.1009	6.6087
	30°	7.2194	6.9598	6.3240
15°	-30°	7.4927	7.4347	7.0375
	-15°	7.4011	7.3803	7.0085
	15°	7.3138	7.1952	6.6985
	30°	7.3136	7.0487	6.4056
30°	-30°	7.8860	7.8200	7.4086
	-15°	7.8047	7.7769	7.3957
	15°	7.7152	7.5834	7.0702
	30°	7.7000	7.4152	6.7444
45°	-30°	9.0713	8.9921	8.5389
	-15°	9.0174	8.9814	8.5742
	15°	8.9265	8.7718	8.2171
	30°	8.8751	8.5443	7.7973

Table 7.10 shows the effect of core thickness, skew angle, and auxetic core cell angle on the non-dimensional frequency parameter. The results indicate that the non-dimensional frequency parameter of the plate rises alongside the core thickness up to a certain point, and then its effect is minimal. Additionally, increased skew angles result in a higher natural frequency due to increased stiffness.

Table 7.10: Influence of thickness of core to face sheets thickness on non-dimensional natural frequency parameter $\bar{\omega} = \omega a^2 / h \sqrt{\rho_c / E_c}$ for sandwich plate ($t/l_1 = 0.1$, $a/h = 20$, $l_2/l_1 = 2$, $V_{CN}^* = 0.17, UD, S^1S^1S^1S^1$)

Skew Angle (ψ)	θ_{hc}	S ¹ S ¹ S ¹ S ¹			CCCC		
		$h_c/h_f=2$	$h_c/h_f=4$	$h_c/h_f=8$	$h_c/h_f=2$	$h_c/h_f=4$	$h_c/h_f=8$
0°	-30°	7.3406	7.5922	7.3744	14.3111	15.2453	15.2092
	-15°	7.2834	7.5394	7.3157	13.9490	14.9329	14.9786
	15°	7.1009	7.1907	6.7543	13.6854	14.3812	14.0697
	30°	6.9598	6.8920	6.3029	13.7701	14.0915	13.3493
15°	-30°	7.4347	7.6942	7.4847	14.4318	15.3755	15.3513
	-15°	7.3803	7.6475	7.4391	14.0741	15.0716	15.1370
	15°	7.1952	7.2928	6.8655	13.8077	14.5123	14.2102
	30°	7.0487	6.9826	6.3922	13.8845	14.2070	13.4610
30°	-30°	7.8200	8.1097	7.9292	14.9334	15.9151	15.9340
	-15°	7.7769	8.0890	7.9383	14.5959	15.6486	15.7911
	15°	7.5834	7.7155	7.3303	14.3209	15.0656	14.8093
	30°	7.4152	7.3594	6.7701	14.3650	14.6963	13.9429
45°	-30°	8.9921	9.3647	9.2469	16.5198	17.6148	17.7413
	-15°	8.9814	9.4205	9.4148	16.2481	17.4694	17.8256
	15°	8.7718	9.0162	8.7603	15.9602	16.8466	16.7533
	30°	8.5443	8.5325	7.9635	15.908	16.2886	15.5460

7.3 Non-Linear Vibration Analysis

This section deals with the plate's non-linear vibration analysis, including isotropic, laminated, FGCNTRC and sandwich plate.

7.3.1 Non-Linear Vibration Analysis of Isotropic Plate

The current formulation was first tested to ensure accuracy by examining the non-linear free vibration frequencies of simply supported isotropic plates. Numerous numerical results for this plate type were already available in the literature. The study focused on thin square plates with $a/h=1000$ and evaluated the non-linear frequency variation with non-dimensional maximum

amplitude (w_{max}/h). Figure 7.3 shows the results, which are compared to published findings. The results indicate a close agreement between the present and available solutions. Singha & Daripa (2009) and Shi et al. (1997)

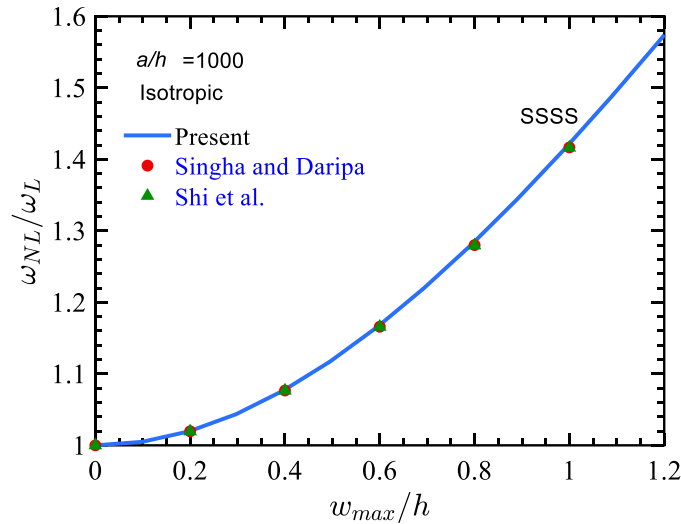


Figure 7.3: A comparison of non-linear to linear frequency ratio of isotropic plate

7.3.2 Non-Linear Vibration Analysis of Laminated Composite Plate

This section also includes a comparison study examining cross-ply and angle-ply lamination schemes. Singha and Daripa's (2009) material properties ($E_L/E_T = 40.0$, $G_{LT}/E_T = 0.6$, $G_{TT}/E_T = 0.5$, $\nu_{LT} = 0.25$; $E_T = 100000.0$ and $\rho = 1.0$), which consider a square plate with a side-to-thickness ratio ($a/h=100$), are used in this analysis. The lamination schemes used are $[0^\circ/90^\circ/0^\circ/90^\circ/0^\circ]$ and $[45^\circ/-45^\circ/45^\circ/-45^\circ/45^\circ]$. The results are presented in Figures 7.4 and 7.5, and the present study shows close agreement with those of Singha and Daripa (2009) for both CCCC and SSSS boundary conditions. This confirms the accuracy and validity of the present formulation.

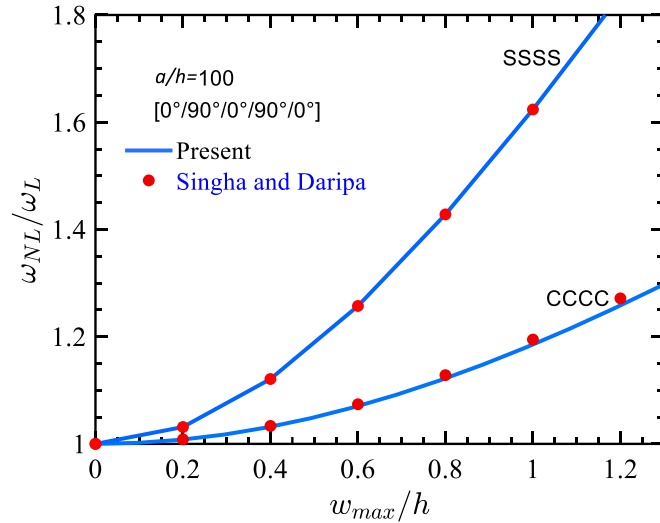


Figure 7.4: A validation study on composite laminated plates'(angle ply) non-linear to linear frequency ratio results in two boundary conditions.

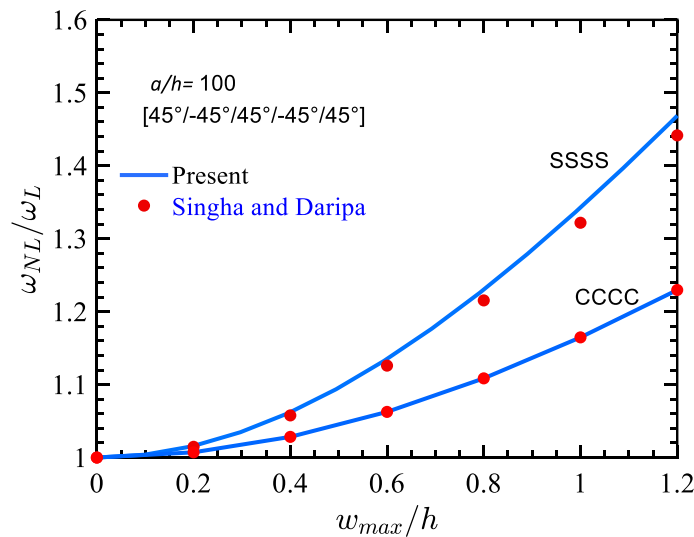


Figure 7.5: A validation study on composite laminated plates'(cross-ply) non-linear to linear frequency ratio results in two boundary conditions.

7.3.3 Non-Linear Vibration Analysis of FGCNTRC Plate

Once the proposed formulation is validated, parametric studies are conducted to investigate the effects of different parameters on the non-linear frequencies of the FGCNTRC plate. Specifically, the non-dimensional non-linear frequency of an SSSS plate with a skewness of 45° is selected for the parametric study. The results include three types of CNTs distribution patterns and three types of CNT volume fractions.

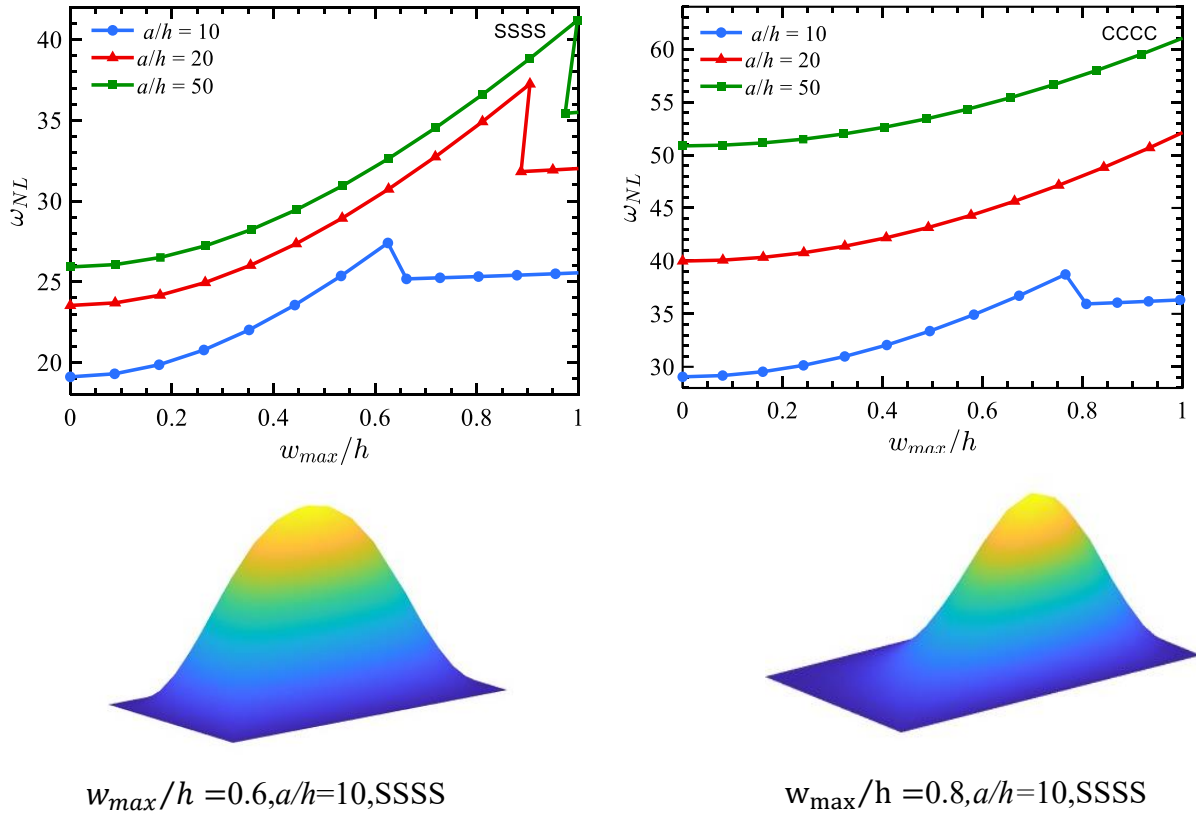


Figure 7.6: Influence of side-to-thickness ratio on the non-linear frequency parameter ($\omega_{NL} = \omega_{nl}(a^2/h)\sqrt{\rho_m/E_m}$) of a FGCNTRC plate ($\psi = 45^\circ, V_{CNT}^* = 0.17, UD$)

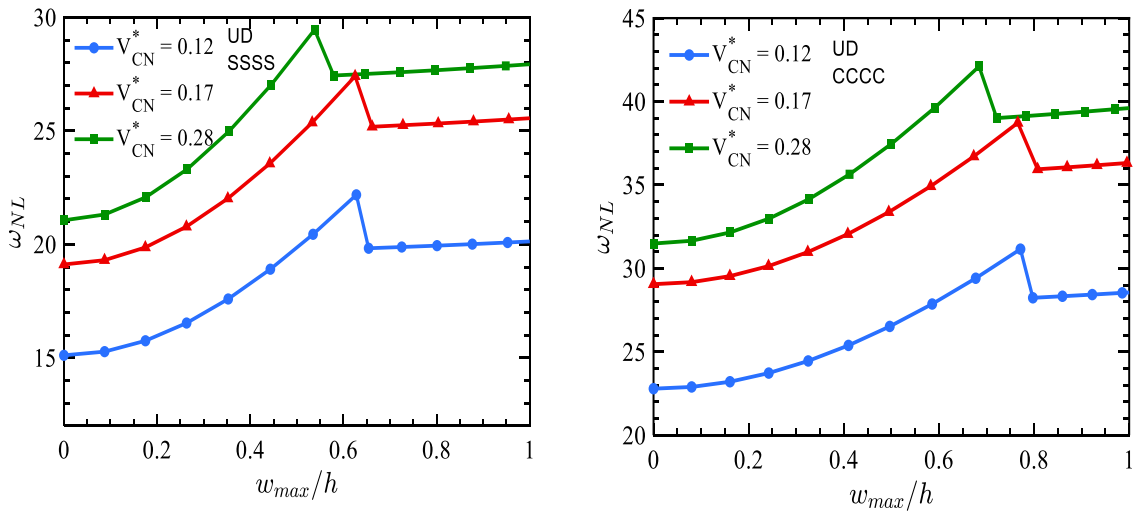


Figure 7.7: Influence of non-linear frequency parameters ($\omega_{NL} = \omega_{nl}(a^2/h)\sqrt{\rho_m/E_m}$) on FGCNTRC plates with UD patterns, different CNTs volume fractions and different boundary conditions ($\psi = 45^\circ, a/h = 10$)

Figure 7.6 indicates the influence of the plate's side thickness ratio on the FGCNTRC plate's non-linear frequency parameter (ω_{NL}). The thickness ratio (a/h) under two distinct boundary conditions, as observed in shear deformable plate theories, affects the non-linear frequency parameter (ω_{NL}). This property is not present in classical plate theory, where the non-linear frequency parameter (ω_{NL}) remains independent of the thickness ratio by ignoring shear strains.

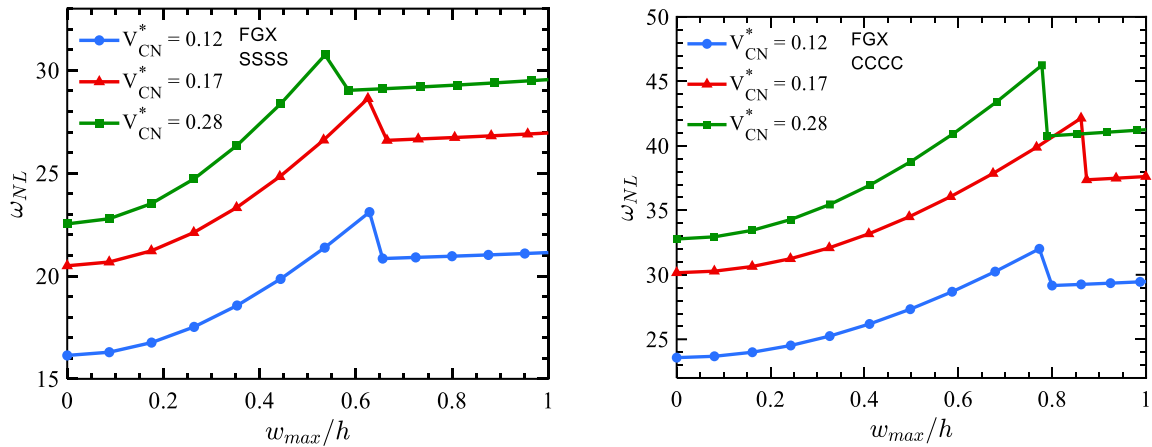


Figure 7.8: Non-linear frequency parameter ($\omega_{NL} = \omega_{nl}(a^2/h)\sqrt{\rho_m/E_m}$) in FGCNTRC plates with FGX patterns, different CNT volume fractions and different boundary conditions ($\psi = 45^\circ, a/h = 10$)

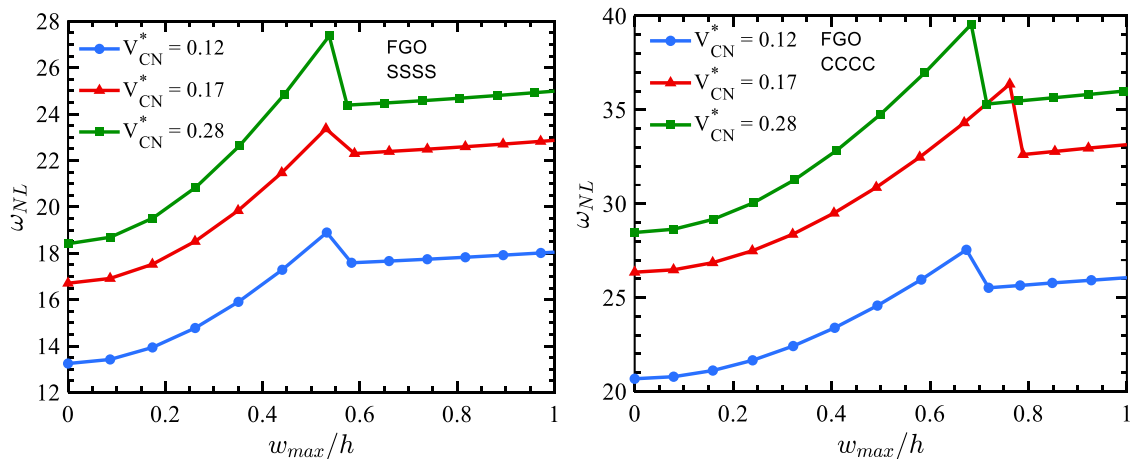


Figure 7.9: Non-linear frequency parameter ($\omega_{NL} = \omega_{nl}(a^2/h)\sqrt{\rho_m/E_m}$) in FGCNTRC plates with FGO patterns, different CNT volume fractions and different boundary conditions ($\psi = 45^\circ, a/h = 10$)

According to the findings in [Figure 7.7](#), the non-linear frequency parameter (ω_{NL}) of the plate increases as the volume fraction of CNTs increases. This is a reasonable conclusion, as an increase in the volume fraction of CNTs leads to a higher flexural stiffness in the plate, resulting in higher stiffness levels. As the amplitude of vibration increases, there is a sudden decrease in the previously increasing frequency trend, followed by a gradual increase. This phenomenon can be attributed to a change in stiffness values, resulting in a redistribution of mode shapes at specific vibration amplitudes. As a result, symmetry is lost, and the maximum displacement is shifted towards one side of the plate, indicating hardening behaviour. [Figures 7.7, 7.8, and 7.9](#) explain that the non-linear frequency parameter (ω_{NL}) increases as a matrix is enhanced with more CNT. FGX CNTRC plates show higher non-linear frequency parameters (ω_{NL}) than UD and FGO CNTRC plates. When comparing the above [Figures](#), it is evident that CCCC plates have higher non-linear frequencies than SSSS plates when all physical and geometrical properties are equal. This is due to the fact that clamping results in more flexural rigidity than a simply supported condition. Similarly, for SSSS plates, a mode redistribution phenomenon occurs at low amplitudes compared to the CCCC plates, resulting in a sudden drop in frequency amplitude curves. When comparing [Figures 7.7,7.8 and 7.9](#), the mode redistribution phenomenon is less pronounced for SSSS plates than CCCC plates.

7.3.4 Non-Linear Vibration Analysis of Skew Sandwich Plate

An investigation was conducted on the influence of skew angle on the non-linear vibration behaviour of simply supported skewed sandwich plates, and the findings are illustrated in [Figure 7.10](#) for two distinct boundary conditions. It has been noted that an increase in skew angle results in a decrease in the non-linear to linear frequency ratios (ω_{NL}/ω_L). This is due to the fact that an increase in skew angle leads to an increase in plate stiffness and linear frequency. However, as the skew angle increases, the linear frequency increase rate is higher than that of non-linear frequency. It has also been found that an increase in the skew angle leads to a drop in frequency ratio at a relatively low amplitude due to mode redistribution. [Figure 7.11](#) examines the effect of the plate's side-to-thickness ratio on the linear to non-linear frequency ratios (ω_{NL}/ω_L). Regardless of the boundary conditions, the non-linear to linear frequency ratio decreases as the plates become thinner due to the stiffness of the plate. It's worth noting that all plates are maintained at room temperature (300 K). The influence of varying core-to-face sheet thickness ratios ($h_c/h_f = 2,4,8$) on the non-linear to linear frequency ratio (ω_{NL}/ω_L) of sandwich plates is illustrated in [Figure 7.12](#).

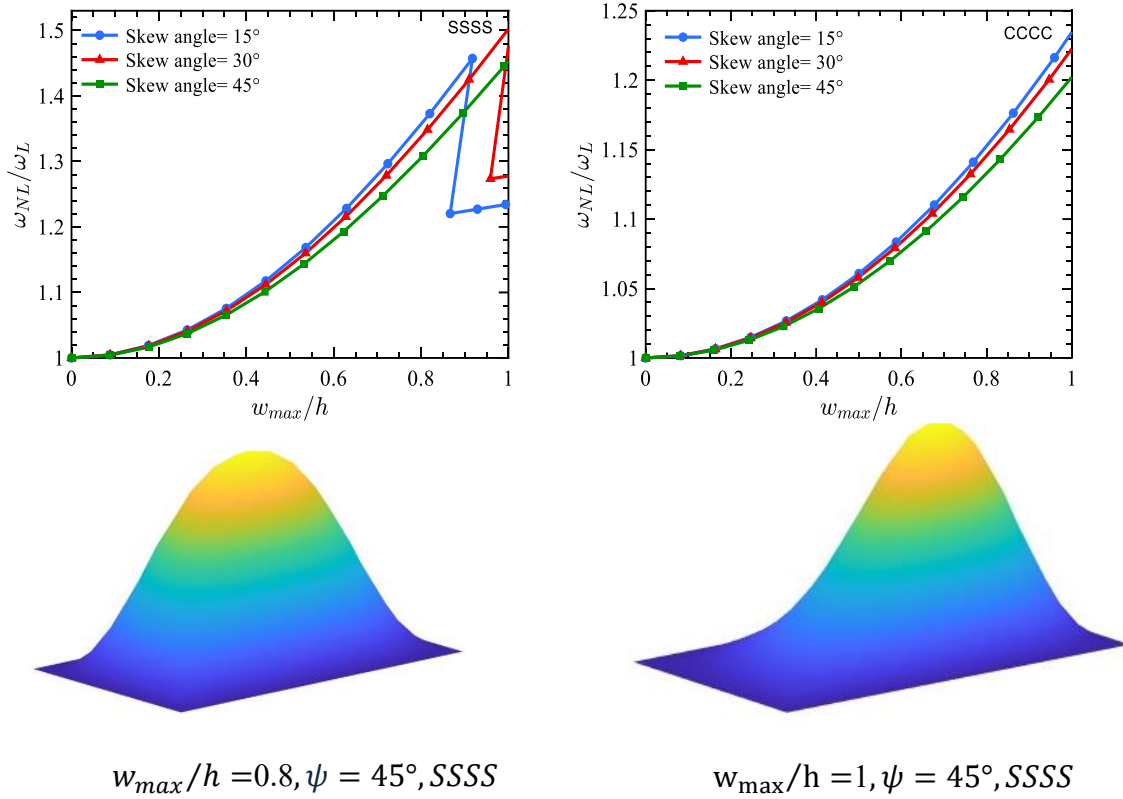


Figure 7.10: Influence of skew angle on the non-linear to linear frequency ratio (ω_{NL}/ω_L) of a sandwich plate at room temperature ($a/h = 10, h_c/h_f = 2, t/l_1 = 0.1, l_2/l_1 = 2, V_{CNT}^* = 0.17, \theta_{hc} = 30^\circ, UD$)

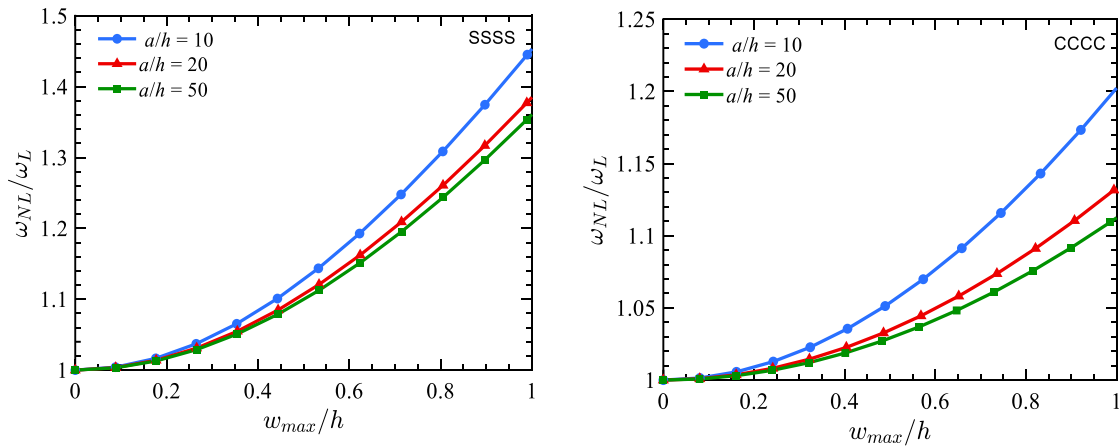


Figure 7.11: Influence of side-to-thickness ratio on the non-linear to linear frequency ratio (ω_{NL}/ω_L) of a skew sandwich plate at room temperature ($\psi = 45^\circ, h_c/h_f = 2, t/l_1 = 0.1, l_2/l_1 = 2, V_{CNT}^* = 0.17, \theta_{hc} = 30^\circ, UD$)

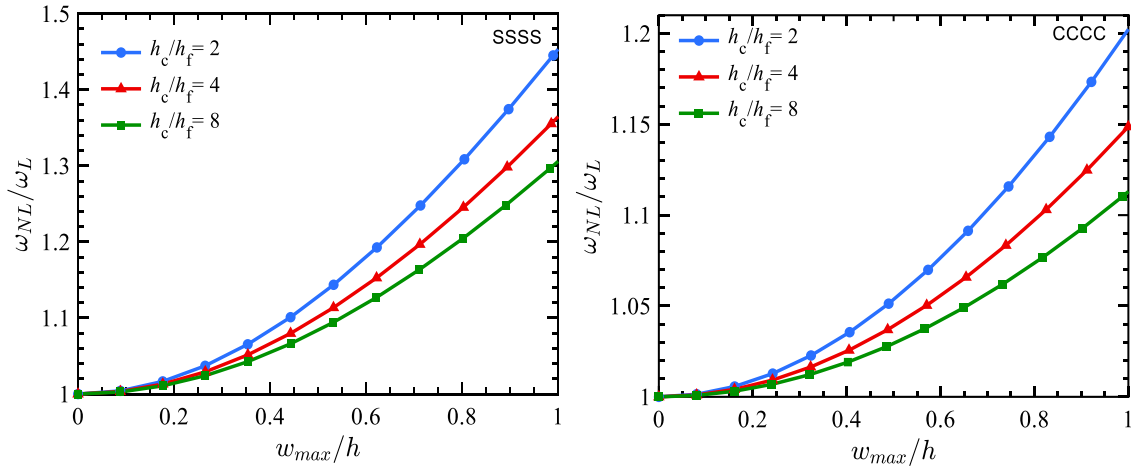


Figure 7.12: Influence of side-to-thickness ratio on the non-linear to linear frequency ratio (ω_{NL}/ω_L) of a skew sandwich plate at room temperature ($\psi = 45^\circ, a/h = 10, t/l_1 = 0.1, l_2/l_1 = 2, V_{CNT}^* = 0.17, \theta_{hc} = 30^\circ, UD$)

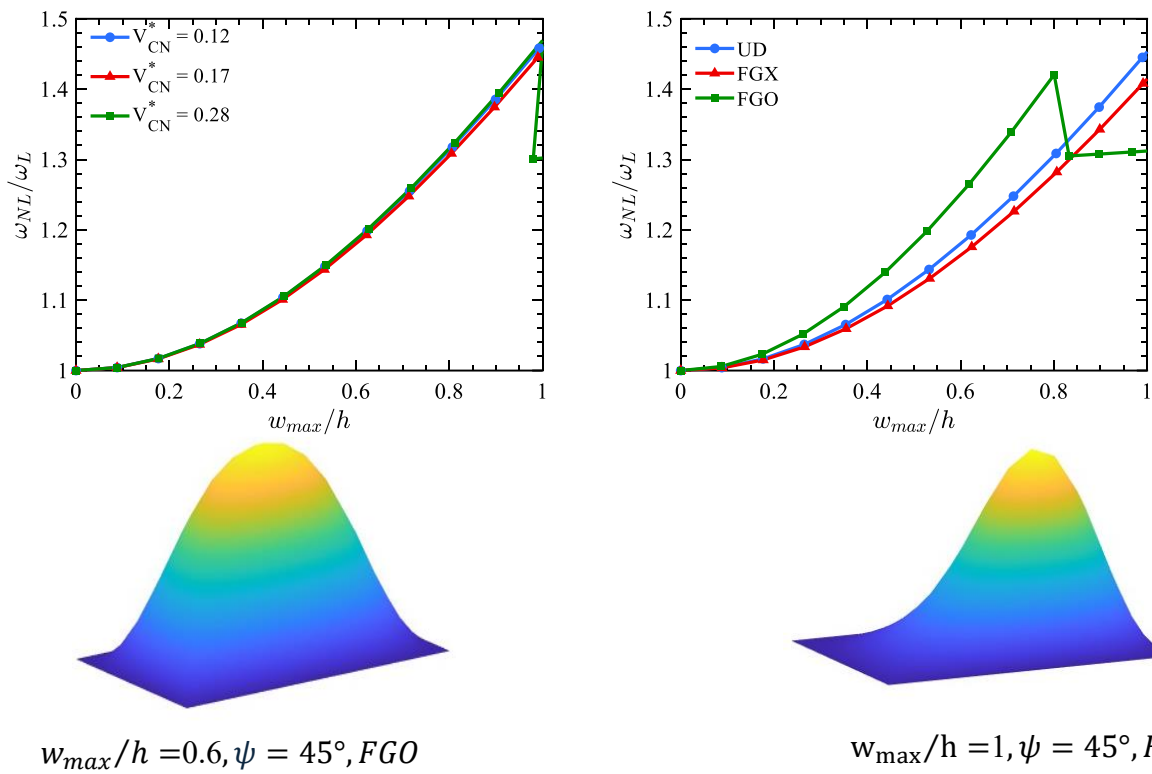


Figure 7.13: The effect of CNT distribution in the face sheets of a skew sandwich plate on non-linear to linear frequency ratio (ω_{NL}/ω_L) at room temperature ($a/h = 10, h_c/h_f = 0.5, t/l_1 = 0.1, l_2/l_1 = 2, \theta_{hc} = 30^\circ, \psi = 45^\circ$)

The results indicate that the non-linear to linear frequency ratio (ω_{NL}/ω_L) decreases with increasing h_c/h_f ratio. As the core's thickness increases, the plate's overall stiffness decreases. The non-linear to linear frequency ratios (ω_{NL}/ω_L) of skew sandwich plates are shown in

Figure 7.13 for three types of functionally graded patterns of CNTs. The results indicate that the FGX pattern results in the highest natural frequency, while the FGO pattern results in the lowest natural frequency. This is because the elasticity modulus of CNTs is significantly greater than the PMMA matrix's. As a result, when the regions near the top and bottom surfaces of the plate contain more CNT, the flexural rigidity of the plate increases, leading to an increase in its natural frequency.

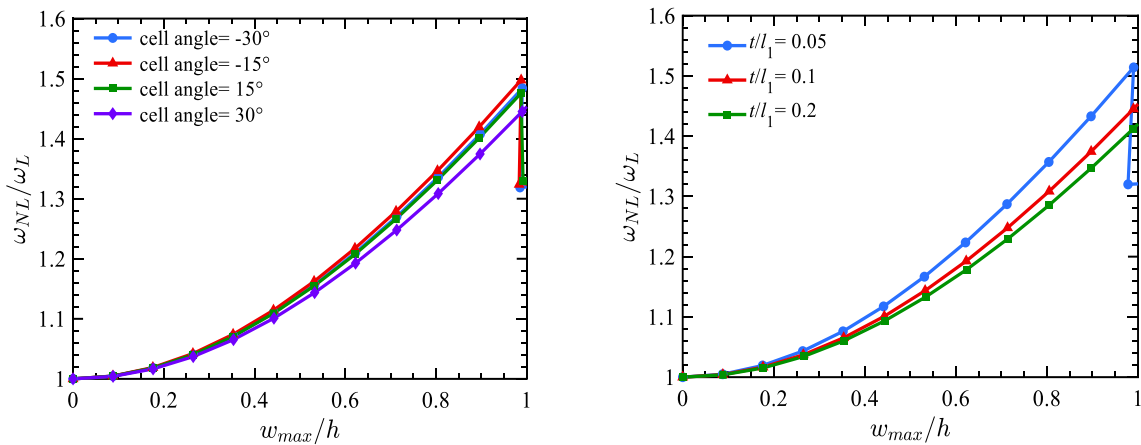


Figure 7.14: Influence of core auxeticity on a skew sandwich plate on non-linear to linear frequency ratio (ω_{NL}/ω_L) at room temperature ($a/h = 10, h_c/h_f = 0.5, t/l_1 = 0.1, l_2/l_1 = 2, V_{CNT}^* = 0.17, \psi = 45^\circ, UD, SSSS$)

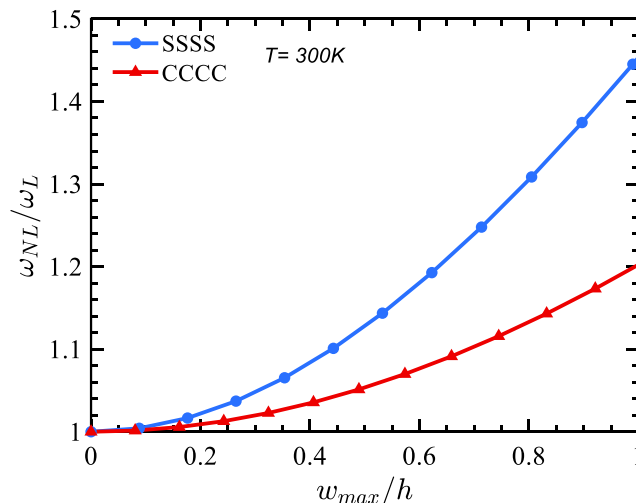


Figure 7.15: Influence of boundary conditions of the skew sandwich plate on non-linear to linear frequency ratio (ω_{NL}/ω_L) subjected to uniform temperature rise ($a/h = 10, h_c/h_f = 2, t/l_1 = 0.1, l_2/l_1 = 2, V_{CNT}^* = 0.17, \theta_{hc} = 30^\circ, \psi = 45^\circ, UD$)

It has been observed that when all the properties are the same, the CCCC plate has the highest frequency, and the SSSS plate has the lowest. This is because clamping causes a local flexural

rigidity in the plate, increasing its overall stiffness. Upon further analysis of the numerical results, it is apparent that the FGX pattern has the lowest non-linear to linear frequency ratio, while the FGO pattern results in the highest non-linear to linear frequency ratio (ω_{NL}/ω_L). The variation of volume fraction on the non-linear to linear frequency ratio (ω_{NL}/ω_L) is minor in a skew sandwich plate. Importantly, it should be noted that the non-linear to linear frequency ratio (ω_{NL}/ω_L) of the FGX sandwich plate is consistently lower across all scenarios than that of the equivalent UD sandwich plate. Figure 7.14 shows the influence of auxetic cores with four different cell angles on the non-linear to linear frequency ratio (ω_{NL}/ω_L). It is apparent from the results that the cell angle in the core geometry does not contribute towards the non-linear to linear frequency ratio (ω_{NL}/ω_L). Furthermore, increasing core cell wall thickness to cell wall length increases the non-linear to linear frequency ratio (ω_{NL}/ω_L). Figure 7.15 illustrates that the SSSS plate has the maximum non-linear to linear frequency ratio, while the minimum ratio (ω_{NL}/ω_L) belongs to CCCC plates. It is expected since clamping results in higher flexural rigidity compared to a simply supported edge. Hence, the rate of increase of linear frequency in CCCC is more than that of increase of the non-linear frequency at a particular amplitude.

7.4 Summary

This research investigates the non-linear vibration behaviour of sandwich plates made of FGCNTRC face sheets and re-entrant auxetic core. The formulation is based on a non-polynomial higher-order theory that considers the von Kármán type of strain-displacement relations. The CNTs are uniformly distributed throughout the plate thickness or according to a prescribed functionally graded pattern. The properties of the composite media are evaluated using an extended rule of mixtures that contains efficiency parameters. The governing equations are obtained using the Hamilton principle. A non-linear eigenvalue problem is established and solved using a displacement control strategy. The numerical results are first validated for isotropic and laminated cases, and then new results are presented for the sandwich and FGCNTRC plates with simply supported and clamped boundary conditions. The following key observations have been made after summarising this chapter.

1. For both CCCC and SSSS plates, the mode redistribution phenomenon takes place. In such a case, the maximum amplitude moves from the center to one side of the plate, which is also distinguished by a sudden drop in frequency amplitude curves. This phenomenon occurs in lower amplitudes for SSSS plates than CCCC plates.

2. It was observed that as the skew angle increased, the non-linear to linear(ω_{NL}/ω_L) frequency ratios decreased. This is due to the fact that an increase in skew angle leads to an increase in plate stiffness and linear frequency. However, as the skew angle increases, the linear frequency increase rate is higher than that of non-linear frequency.
3. The carbon nanotube (CNTs) distribution pattern notably influences the non-linear to linear frequency ratio(ω_{NL}/ω_L). The order of non-linear to linear frequency ratio (ω_{NL}/ω_L) observed in FGCNTRC plates is completely opposite to the order of stiffness. Specifically, FGO exhibits the highest non-linear to linear frequency ratio(ω_{NL}/ω_L) followed by UD and FG-X.
4. It has been observed that the non-linear to linear frequency ratio(ω_{NL}/ω_L) increases with the thickness of the plate due to the stiffness of the plate.
5. The results indicate that the non-linear to linear frequency ratio(ω_{NL}/ω_L) decreases with increasing h_c/h_f ratio. As the core's thickness increases, and the plate's overall stiffness decreases.
6. It is apparent from the results that the cell angle in the core geometry does not contribute towards the non-linear to linear frequency ratio(ω_{NL}/ω_L). Furthermore, increasing core cell wall thickness to cell wall length increases the non-linear to linear frequency ratio(ω_{NL}/ω_L).

Conclusions

8.1 General

In the present study, linear and non-linear analyses of the sandwich plate are carried out using the Isogeometric analysis (IGA) approach with non-polynomial higher-order theory. An in-house computer code is written to analyse the sandwich plates of various geometries subjected to different loading and boundary conditions. The study considered two types of cores: metal foam core and auxetic re-entrant honeycomb core. Section 8.2 details the performance of the method used, while Sections 8.3 and 8.4 outline specific conclusions drawn from the analysis of sandwich plates under mechanical and thermal loads, respectively. Section 8.5 presents findings from investigating sandwich plates' non-linear vibration characteristics. Finally, Section 8.6 discusses potential avenues for future research in this field.

8.2 Performance of the Present Numerical Method

The effects of different parameters on the efficiency of Isogeometric analysis with non-polynomial higher-order theory are investigated, and the observations made are as follows:

1. The use of non-uniform rational B-spline (NURBS) in isogeometric analysis (IGA) improves computational efficiency while maintaining accuracy as compared to finite element method (FEM). This is a significant advantage in computational mechanics, where precise and efficient solutions are of paramount importance. These results highlight the practicality and effectiveness of IGA, making it a preferred choice for applications that require fast and accurate results.
2. The isogeometric approach exhibits monotonic convergence and provides accurate and stable results with mesh refinement. k -refinement procedure provides faster convergence than h and p refinement strategies. It has also been observed that when the order is higher, the results converge faster and require fewer knot insertions.

3. The non-polynomial higher-order theory accounts for the shear deformation effects and satisfies the zero transverse shear stresses on the top and bottom surfaces of the plate; thus, a shear correction factor is not required.
4. The accuracy of the present results is marginally better than that of other numerical methods like finite element analysis.

8.3 Stability Analysis of Plates Under Non-Uniform Mechanical Loadings

The conclusions drawn from the linear and non-linear stability behaviour of sandwich plate with metal foam core subjected to non-uniform mechanical loading are given below:

1. Isogeometric analysis and non-polynomial higher-order theory can produce accurate and effective results for predicting the post-buckling behaviours of sandwich plates.
2. The results for order 3 converged at 19-knot insertions for linear buckling analysis and 15-knot insertions for non-linear post-buckling and post-buckled vibration behaviour. As a result, the same knot insertions are utilised for all subsequent investigations involving non-uniform mechanical loadings.
3. As the skew angle of the sandwich plate increases, the buckling strength increases for both SSSS and CCCC skew sandwich plates due to the higher stiffness of the plate.
4. The buckling load and post-buckling strength are higher for the SPD than UPD because the symmetric porosity distribution reduces the stiffness of the plate by a smaller amount than the uniform porosity distribution.
5. In the pre-buckling region, the frequencies are higher for SPD than UPD and higher for UPD than SPD in the post-buckling regime.
6. The buckling loads increase with h_c/h_f ratio. This indicates that the core layer contributes more to the plate's stiffness than the face sheets, as the elasticity modulus of the core layer is more than the resultant modulus of the facings.
7. The buckling strength is higher when the CNTs are distributed more towards the plate's surfaces than the centre.
8. The critical load is highest for uniform compression and least under concentrated load due to a high concentration of stresses.

8.4 Stability Behaviour of Plates Under Thermal Loadings

The following conclusions are made from the linear buckling and non-linear post-buckling of plates under thermal loadings:

1. The results converged at 15-knot insertions with order 3 in thermal buckling and post-buckling analysis. Therefore, the same number of knot insertions are employed for all further investigations.
2. As the skew angle increases, the critical buckling temperature increases, and the post-buckling deflection is lower for the same magnitude of load because the stiffness of the sandwich skew plates in a thermal environment highly depends on the variation in the skew angle.
3. Increasing the core thickness may also enhance the critical buckling strength of the sandwich plates. As the relative thickness of the core increases, the buckling load parameter also increases because the rate of change of geometric stiffness with a change in core thickness is higher than that of the overall stiffness of the sandwich plate.
4. The critical buckling temperature of the skew sandwich plates with a positive cell angle of auxetic core and negative Poisson's ratio is slightly lower than those with a negative cell inclination angle. This is because the elastic modulus and stiffness of the auxetic honeycomb core will reduce with the rise of the cell wall angle.
5. The FG-X pattern of CNTs in facings results in higher buckling temperature due to higher rigidity and less post-buckling deflection in comparison to other distribution patterns.
6. If the imperfection is relatively large, buckling deformation highly correlates with the shape of the imperfection.
7. The sinusoidal and L2-type initial imperfections have nearly identical effects on the plate due to their similar shapes.
8. The critical buckling temperature of a clamped plate is greater than that of a simply supported one since clamped edges causes higher flexural rigidity when compared to a simply supported edge.

8.5 Non-Linear Vibration Analysis of Sandwich Plate

The following conclusions are made from the non-linear vibration analysis of sandwich plates with auxetic cores in thermal environments.

1. The mode redistribution phenomenon occurs for clamped (CCCC) and simply supported (SSSS) plates. In such a case, the maximum amplitude moves from the center to one side of the plate, which is also distinguished by a sudden drop in frequency amplitude curves. This phenomenon occurs in lower amplitudes for SSSS plates than CCCC plates.
2. It is observed that as the skew angle increases, the linear to non-linear frequency ratios (ω_{NL}/ω_L) decreased. This is because an increase in skew angle leads to an increase in plate stiffness and natural frequencies. However, as the skew angle increases, the linear frequency increase rate is higher than that of non-linear frequency.
3. The carbon nanotube (CNT) distribution pattern notably influences the non-linear to linear frequency ratio (ω_{NL}/ω_L). The order of non-linear to linear frequency ratio (ω_{NL}/ω_L) observed in FGCNTRC plates is completely opposite to the order of stiffness. Specifically, FGO exhibits the highest non-linear to linear frequency ratio (ω_{NL}/ω_L) followed by UD and FG-X.
4. The results indicate that the non-linear to linear frequency ratio (ω_{NL}/ω_L) decreases with increasing h_c/h_f ratio because the core's thickness increases, and the plate's overall stiffness decreases.
5. It has been observed that the non-linear to linear frequency ratio (ω_{NL}/ω_L) increases with the thickness of the plate due to the stiffness of the plate.
6. It is apparent from the results that the cell angle in the core geometry does not contribute towards the non-linear to linear frequency ratio (ω_{NL}/ω_L). Furthermore, increasing core cell wall thickness to cell wall length increases the non-linear to linear frequency ratio (ω_{NL}/ω_L).
7. The non-linear to linear frequency ratio (ω_{NL}/ω_L) of SSSS plates are higher than CCCC plates at a particular amplitude since clamping results in higher flexural rigidity compared to a simply supported edge. Hence, the rate of increase of linear frequency in CCCC is more than that of increase of the non-linear frequency at a particular amplitude.

8.6 Recommendations for Future Work

This study's primary focus was to analyse sandwich plate buckling, post-buckling, post-buckled vibration, and non-linear vibration behaviours. The research assumes that the material used in the study is homogeneous and elastic for all the problems examined. However, this research can be further extended to include structures made of non-homogeneous or inelastic materials. Furthermore, the present formulation can also be used to investigate the dynamic instability behaviour of sandwich plates in thermal environments. Finally, it's worth mentioning that the isogeometric analysis (IGA) technique employed in this study can also be applied to other areas, such as fracture mechanics, optimisation, and contact problems.

APPENDICES

Modified Riks Technique

The non-linear algebraic equilibrium equations and its linearised form is given by:

$$\mathbf{K}\mathbf{U} = \mathbf{F} \quad (\text{A.1})$$

$$\mathbf{K}_T\Delta\mathbf{U} = \Delta\mathbf{F} \quad (\text{A.2})$$

The force vector can be written as $\mathbf{F} = \lambda\bar{\mathbf{F}}$, where λ is an additional dependent variable. The various steps of the algorithm for Modified Riks technique are given by (Reddy, 2014)

A. First iteration of first load step

(i) Take initial load increment $\delta\lambda_1^0$ as one and solution vector $U_0 = [0]$

(ii) Solve for $\delta\hat{\mathbf{U}}_1$ and $\delta\bar{\mathbf{U}}_1^{(1)}$ using the following equations

$$\delta\bar{\mathbf{U}}_n^r = -\mathbf{K}_T^{-1}\mathbf{R}_n^{(r-1)} \quad (\text{A.3})$$

$$\delta\hat{\mathbf{U}}_n = \mathbf{K}_T^{-1}\bar{\mathbf{F}} \quad (\text{A.4})$$

where \mathbf{R}_n^{r-1} is the unbalanced force vector at any iteration $(r-1)^{th}$ iteration of n^{th} load step and is given by:

$$\mathbf{R}_n^{r-1} = \mathbf{K}\mathbf{U}_n^{r-1} - \lambda_n^{r-1}\bar{\mathbf{F}} \quad (\text{A.5})$$

(iii) Now, the solution is updated by calculating the increments as:

$$\delta\mathbf{U}_n^r = \delta\bar{\mathbf{U}}_n^r + \delta\lambda_n^r\delta\hat{\mathbf{U}}_n \quad (\text{A.6})$$

$$= -\mathbf{K}_T^{-1} R_n^{r-1} + \delta \lambda_n^r \mathbf{K}_T^{-1} \bar{\mathbf{F}} \quad (\text{A.7})$$

$$\mathbf{U}_1 = \mathbf{U}_0 + \delta \mathbf{U}_1^1 \quad (\text{A.8})$$

(iv) Load increment is updated in this step:

$$\lambda_n^r = \lambda_n^{r-1} + \delta \lambda_n^{r-1} \quad (\text{A.9})$$

(v) Compute the arc length

$$\Delta s = \delta \lambda_1^0 \sqrt{\delta \hat{\mathbf{U}}_1^T \cdot \delta \hat{\mathbf{U}}_1}, \quad \delta \hat{\mathbf{U}}_1^T = \mathbf{K}_T^{-1} F, \quad \mathbf{K}_T = \mathbf{K}_T(U_0) \quad (\text{A.10})$$

B. First iteration of any load vector except the first load step

(i) Compute the initial increment load parameter $\delta \lambda_n^0$ by using the following equation:

$$\delta \lambda_n^0 = \pm (\Delta s_n) \cdot (\delta \hat{\mathbf{U}}_n^T \cdot \hat{\mathbf{U}}_n)^{-1/2} \quad (\text{A.11})$$

(ii) Compute the incremental solution

$$\delta \bar{\mathbf{U}}_n^r = -\mathbf{K}_T^{-1} R_n^{r-1} \quad (\text{A.12})$$

(iii) Update the total solution vector and load parameter

$$\delta \mathbf{U}_n^1 = \delta \bar{\mathbf{U}}_n^1 + \delta \lambda_n^0 \delta \hat{\mathbf{U}}_n^1 \quad (\text{A.13})$$

$$\mathbf{U}_n = \mathbf{U}_{n-1} + \delta \mathbf{U}_n^1 \quad (\text{A.14})$$

$$\lambda_n^1 = \lambda_n^0 + \delta \lambda_n^0, \quad \Delta \mathbf{U}_n^1 = \delta \mathbf{U}_n^1 \quad (\text{A.15})$$

(iv) Check for convergence

C. The r^{th} iteration for any load step ($r = 2, 3 \dots$)

(i) Update the external load vector.

$$\mathbf{F}^{r-1} = \lambda_n^{r-1} \bar{\mathbf{F}} \quad (\text{A.16})$$

(ii) Solve for $\delta \hat{\mathbf{U}}_1$ and $\delta \bar{\mathbf{U}}_1^{(1)}$ using the following equations

$$\delta \bar{\mathbf{U}}_n^r = -\mathbf{K}_T^{-1} \mathbf{R}_n^{(r-1)} \quad (\text{A.17})$$

$$\delta \hat{\mathbf{U}}_n = \mathbf{K}_T^{-1} \bar{\mathbf{F}} \quad (\text{A.18})$$

(iii) Calculate the incremental load parameter $\delta \lambda_n^r$ From the following quadratic equation:

$$\begin{aligned} a_1 \delta \lambda^2 + 2a_2 \delta \lambda + a_3 &= 0 \\ a_1 &= \delta \hat{\mathbf{U}}_n^T \cdot \delta \hat{\mathbf{U}}_n \\ a_2 &= (\delta \bar{\mathbf{U}}_n^r + \Delta \mathbf{U}_n^{r-1})^T \cdot \delta \hat{\mathbf{U}}_n \\ a_3 &= (\delta \bar{\mathbf{U}}_n^r + \Delta \mathbf{U}_n^{r-1})^T \cdot (\delta \bar{\mathbf{U}}_n^r + \Delta \mathbf{U}_n^{r-1}) - (\Delta s)_n^2 \end{aligned} \quad (\text{A.19})$$

equations. The $\delta \lambda$ that gives the positive value of the product $\Delta \mathbf{U}_n^{r-1} \cdot \Delta \mathbf{U}_n^r$ is selected. If both the roots give the positive value of the product, we use the one giving the smallest value of $(-a_3/a_2)$

(iv) Compute the correction to the solution vector and update the incremental solution vector, total solution vector and the load parameter.

$$\begin{aligned} \delta \mathbf{U}_n^r &= \delta \bar{\mathbf{U}}_n^r + \delta \lambda \cdot \delta \hat{\mathbf{U}}_n \\ \Delta \mathbf{U}_n^r &= \Delta \mathbf{U}_n^{r-1} + \delta \mathbf{U}_n^r \\ \mathbf{U}_n &= \mathbf{U}_{n-1} + \Delta \mathbf{U}_n^r \\ \lambda_n^r &= \lambda_n^{r-1} + \delta \lambda_n^r \end{aligned} \quad (\text{A.20})$$

(v) Repeat the above steps until the following convergence criterion is satisfied:

$$\left[\frac{(\mathbf{U}_n^r - \mathbf{U}_n^{r-1})^T \cdot (\mathbf{U}_n^r - \mathbf{U}_n^{r-1})}{(\mathbf{U}_n^r)^T \mathbf{U}_n^r} \right]^{1/2} < \epsilon \quad (\text{A.21})$$

(vi) Adjust the arc length for the subsequent load steps by $\Delta S = \Delta s_{n-1} I_d / I_o$ δs_{n-1} is the arc length used in the last iteration of the $(n - 1)^{st}$ Load step. I_d is the number of desired iterations (usually < 5) and I_o is the number of iterations required for convergence in the previous step.

References

- Adim, B., Daouadji, T.H. and Abbes, B., 2016. Buckling analysis of anti-symmetric cross-ply laminated composite plates under different boundary conditions. *International Applied Mechanics*, 52, pp.661-676.
- Akkerman, I., Bazilevs, Y., Kees, C.E. and Farthing, M.W., 2011. Isogeometric analysis of free-surface flow. *Journal of Computational Physics*, 230(11), pp.4137-4152.
- Alijani, F. and Amabili, M., 2013. Non-linear dynamic instability of functionally graded plates in thermal environments. *International Journal of Non-Linear Mechanics*, 50, pp.109-126.
- Arani, A.G., Maghamikia, S., Mohammadimehr, M. and Arefmanesh, A., 2011. Buckling analysis of laminated composite rectangular plates reinforced by SWCNTs using analytical and finite element methods. *Journal of mechanical science and technology*, 25, pp.809-820.
- Aydogdu, M., 2006. Comparison of various shear deformation theories for bending, buckling, and vibration of rectangular symmetric cross-ply plate with simply supported edges. *Journal of Composite materials*, 40(23), pp.2143-2155.
- Babu, C.S. and Kant, T.A.R.U.N., 1999. Two shear deformable finite element models for buckling analysis of skew fibre-reinforced composite and sandwich panels. *Composite Structures*, 46(2), pp.115-124.
- Batoz, J.L. and Dhatt, G., 1979. Incremental displacement algorithms for nonlinear problems. *International Journal for Numerical Methods in Engineering*, 14(8), pp.1262-1267.
- Bazilevs, Y., Hsu, M.C. and Scott, M., 2012. Isogeometric fluid–structure interaction analysis with emphasis on non-matching discretizations, and with application to wind turbines. *Computer Methods in Applied Mechanics and Engineering*, 249, pp.28-41.
- Bazilevs, Y., Takizawa, K., Tezduyar, T.E., Korobenko, A., Kuraishi, T. and Otoguro, Y., 2023. Computational aerodynamics with isogeometric analysis. *Journal of Mechanics*, 39, pp.24-39.
- Belalia, S.A. and Houmat, A., 2012. Nonlinear free vibration of functionally graded shear deformable sector plates by a curved triangular p-element. *European Journal of Mechanics-A/Solids*, 35, pp.1-9.

- Bergan, P.G., Horrigmoe, G., Bråkeland, B. and Søreide, T.H., 1978. Solution techniques for non-linear finite element problems. *International Journal for Numerical Methods in Engineering*, 12(11), pp.1677-1696.
- Betts, C., 2012. Benefits of metal foams and developments in modelling techniques to assess their materials behaviour: a review. *Materials Science and Technology*, 28(2), pp.129-143.
- Bourada, F., Amara, K. and Tounsi, A., 2016. Buckling analysis of isotropic and orthotropic plates using a novel four variable refined plate theory.
- Brunelle, E.J., 1971. Buckling of transversely isotropic Mindlin plates. *AIAA Journal*, 9(6), pp.1018-1022.
- Camacho Gutiérrez, S.V., Jáuregui Correa, J.C., Dominguez-Gonzalez, A. and Gómez-Loenzo, R.A., 2020. An application of isogeometric analysis and boundary integral element method for solving nonlinear contact problems. *Applied Sciences*, 10(7), p.2345.
- Cetkovic, M., 2022. Influence of initial geometrical imperfections on thermal stability of laminated composite plates using layerwise finite element. *Composite Structures*, 291, p.115547.
- Chen, C.S., Fung, C.P. and Chien, R.D., 2006. A further study on nonlinear vibration of initially stressed plates. *Applied mathematics and computation*, 172(1), pp.349-367.
- Chen, C.S., Liu, F.H. and Chen, W.R., 2017. Dynamic characteristics of functionally graded material sandwich plates in thermal environments. *Mechanics of Advanced Materials and Structures*, 24(2), pp.157-167.
- Chen, W.J., Lin, P.D. and Chen, L.W., 1991. Thermal buckling behavior of thick composite laminated plates under nonuniform temperature distribution. *Computers & structures*, 41(4), pp.637-645.
- Ćojbašić, Ž., Ivačko, N., Marinković, D., Milić, P., Petrović, G., Milošević, M. and Marković, N., 2023. Isogeometric finite element analysis with machine learning integration for piezoelectric laminated shells. *J. Eng. Manag. Syst. Eng*, 2(4), pp.196-203.
- Cong, P.H. and Duc, N.D., 2021. length Nonlinear dynamic analysis of porous eccentrically stiffened double curved shallow auxetic shells in thermal environments. *THIN-WALLED STRUCTURES*, 163.

- Cottrell, J.A., Reali, A., Bazilevs, Y. and Hughes, T.J., 2006. Isogeometric analysis of structural vibrations. *Computer methods in applied mechanics and engineering*, 195(41-43), pp.5257-5296.
- Cox, M.G., 1972. The numerical evaluation of B-splines. *IMA Journal of Applied mathematics*, 10(2), pp.134-149.
- Dash, P. and Singh, B.N., 2012. Buckling and post-buckling of laminated composite plates. *Mechanics Research Communications*, 46, pp.1-7.
- De Boor, C., 1972. On calculating with B-splines. *Journal of Approximation theory*, 6(1), pp.50-62.
- Dedè, L., Borden, M.J. and Hughes, T.J., 2012. Isogeometric analysis for topology optimization with a phase field model. *Archives of Computational Methods in Engineering*, 19, pp.427-465.
- Del Prado, Z.J.G.N., Gonçalves, P.B. and Païdoussis, M.P., 2009. Nonlinear vibrations and imperfection sensitivity of a cylindrical shell containing axial fluid flow. *Journal of Sound and Vibration*, 327(1-2), pp.211-230.
- Duc, N.D. and Van Tung, H., 2011. Mechanical and thermal postbuckling of higher order shear deformable functionally graded plates on elastic foundations. *Composite Structures*, 93(11), pp.2874-2881.
- Durvasula, S., 1970. Buckling of clamped skew plates. *AIAA Journal*, 8(1), pp.178-181.
- Eisenberger, M. and Alexandrov, A., 2003. Buckling loads of variable thickness thin isotropic plates. *Thin-Walled Structures*, 41(9), pp.871-889.
- Eslami, M.R., Eslami, J. and Jacobs, M., 2018. *Buckling and postbuckling of beams, plates, and shells*. Switzerland: Springer International Publishing.
- Fang, W., Zhang, J., Yu, T. and Bui, T.Q., 2021. Analysis of thermal effect on buckling of imperfect FG composite plates by adaptive XIGA. *Composite Structures*, 275, p.114450.
- Farzam, A. and Hassani, B., 2018. Thermal and mechanical buckling analysis of FG carbon nanotube reinforced composite plates using modified couple stress theory and isogeometric approach. *Composite Structures*, 206, pp.774-790.
- Fazzolari, F.A., 2018. Thermoelastic vibration and stability of temperature-dependent carbon nanotube-reinforced composite plates. *Composite structures*, 196, pp.199-214.

- Ferreira, A.J.M., Roque, C.M.C., Neves, A.M.A., Jorge, R.M.N., Soares, C.M. and Reddy, J.N., 2011. Buckling analysis of isotropic and laminated plates by radial basis functions according to a higher-order shear deformation theory. *Thin-Walled Structures*, 49(7), pp.804-811.
- Fu, T., Wu, X., Xiao, Z. and Chen, Z., 2021. Dynamic instability analysis of porous FGM conical shells subjected to parametric excitation in thermal environment within FSDT. *Thin-Walled Structures*, 158, p.107202.
- Fu, Y., Zhong, J., Shao, X. and Tao, C., 2016. Analysis of nonlinear dynamic stability for carbon nanotube-reinforced composite plates resting on elastic foundations. *Mechanics of Advanced Materials and Structures*, 23(11), pp.1284-1289.
- Geng, X., Zhao, L. and Zhou, W., 2021. Finite-element buckling analysis of functionally graded GPL-reinforced composite plates with a circular hole. *Mechanics Based Design of Structures and Machines*, 49(7), pp.1028-1044.
- Gómez, H., Calo, V.M., Bazilevs, Y. and Hughes, T.J., 2008. Isogeometric analysis of the Cahn–Hilliard phase-field model. *Computer methods in applied mechanics and engineering*, 197(49-50), pp.4333-4352.
- Gu, X.J., Hao, Y.X., Zhang, W. and Chen, J., 2019. Dynamic stability of rotating cantilever composite thin-walled twisted plate with initial geometric imperfection under in-plane load. *Thin-Walled Structures*, 144, p.106267.
- Gunda, J.B., 2013. Thermal post-buckling analysis of square plates resting on elastic foundation: A simple closed-form solutions. *Applied Mathematical Modelling*, 37(7), pp.5536-5548.
- Gupta, A. and Pradyumna, S., 2022. Nonlinear dynamic analysis of sandwich shell panels with auxetic honeycomb core and curvilinear fibre reinforced face sheets. *European Journal of Mechanics-A/Solids*, 95, p.104640.
- Gupta, A., Talha, M. and Singh, B.N., 2016. Vibration characteristics of functionally graded material plate with various boundary constraints using higher order shear deformation theory. *Composites Part B: Engineering*, 94, pp.64-74.
- Han, Y. and Elliott, J., 2007. Molecular dynamics simulations of the elastic properties of polymer/carbon nanotube composites. *Computational materials science*, 39(2), pp.315-323.

- Hassani, B., Tavakkoli, S.M. and Moghadam, N.Z., 2011. Application of isogeometric analysis in structural shape optimization. *Scientia Iranica*, 18(4), pp.846-852.
- Hughes, T.J., Cottrell, J.A. and Bazilevs, Y., 2005. Isogeometric analysis: CAD, finite elements, NURBS, exact geometry and mesh refinement. *Computer methods in applied mechanics and engineering*, 194(39-41), pp.4135-4195.
- Imran, M., Khan, R. and Badshah, S., 2018. A review on the effect of delamination on the performance of composite plate. *Pakistan Journal of Scientific & Industrial Research Series A: Physical Sciences*, 61(3), pp.173-182.
- Jagtap, K.R., Lal, A. and Singh, B.N., 2011. Stochastic nonlinear free vibration analysis of elastically supported functionally graded materials plate with system randomness in thermal environment. *Composite structures*, 93(12), pp.3185-3199.
- Jahanpour, A., 2023. Buckling analysis of functionally graded plates subjected to combined in-plane loads. *Journal of Engineering Mathematics*, 138(1), p.2.
- Jam, J. E., and Y. Kiani. "Buckling of pressurized functionally graded carbon nanotube reinforced conical shells." *Composite Structures* 125 (2015): 586-595.
- Jiang, Q., Tallury, S.S., Qiu, Y. and Pasquinelli, M.A., 2014. Molecular dynamics simulations of the effect of the volume fraction on unidirectional polyimide-carbon nanotube nanocomposites. *Carbon*, 67, pp.440-448.
- Kamarian, S. and Song, J.I., 2023. Thermal buckling of advanced hybrid composite plates in the co-presence of CNTs and SMAs. *Mechanics of Advanced Materials and Structures*, 30(4), pp.782-793.
- Kant, Tarun and Babu, C.S., 2000. Thermal buckling analysis of skew fibre-reinforced composite and sandwich plates using shear deformable finite element models. *Composite Structures*, 49(1), pp.77-85.
- Kiani, Y., 2017. Buckling of FG-CNT-reinforced composite plates subjected to parabolic loading. *Acta Mechanica*, 228(4), pp.1303-1319.
- Kiani, Y., 2017. Thermal buckling of temperature-dependent FG-CNT-reinforced composite skew plates. *Journal of Thermal Stresses*, 40(11), pp.1442-1460.

- Kiani, Y., 2018. NURBS-based isogeometric thermal postbuckling analysis of temperature dependent graphene reinforced composite laminated plates. *Thin-Walled Structures*, 125, pp.211-219.
- Kiani, Y., 2018. Thermal post-buckling of temperature dependent sandwich plates with FG-CNTRC face sheets. *Journal of Thermal Stresses*, 41(7), pp.866-882.
- Kiani, Y., 2020. NURBS-based thermal buckling analysis of graphene platelet reinforced composite laminated skew plates. *Journal of Thermal Stresses*, 43(1), pp.90-108.
- Kim, N.H., 2014. Introduction to nonlinear finite element analysis. Springer Science & Business Media.
- Kim, S.E., Duc, N.D., Nam, V.H. and Van Sy, N., 2019. Nonlinear vibration and dynamic buckling of eccentrically oblique stiffened FGM plates resting on elastic foundations in thermal environment. *Thin-Walled Structures*, 142, pp.287-296.
- Kitipornchai, S., Yang, J. and Liew, K.M., 2004. Semi-analytical solution for nonlinear vibration of laminated FGM plates with geometric imperfections. *International Journal of Solids and Structures*, 41(9-10), pp.2235-2257.
- Komur, M.A., Sen, F., Ataş, A. and Arslan, N., 2010. Buckling analysis of laminated composite plates with an elliptical/circular cutout using FEM. *advances in Engineering software*, 41(2), pp.161-164.
- Kreja, I., 2011. A literature review on computational models for laminated composite and sandwich panels. *Open Engineering*, 1(1), pp.59-80.
- Kumar, C.N. and Singh, B.N., 2009. Thermal buckling and post-buckling of laminated composite plates with SMA fibers using layerwise theory. *International Journal for Computational Methods in Engineering Science and Mechanics*, 10(6), pp.423-429.
- Kumar, R., Mondal, S., Guchhait, S. and Jamatia, R., 2017. Analytical approach for dynamic instability analysis of functionally graded skew plate under periodic axial compression. *International Journal of Mechanical Sciences*, 130, pp.41-51.
- Lavroff, J., Davis, M.R., Holloway, D.S. and Thomas, G., 2013. Wave slamming loads on wave-piercer catamarans operating at high-speed determined by hydro-elastic segmented model experiments. *Marine structures*, 33, pp.120-142.

- Lei, Z.X., Liew, K.M. and Yu, J.L., 2013. Buckling analysis of functionally graded carbon nanotube-reinforced composite plates using the element-free kp-Ritz method. *Composite Structures*, 98, pp.160-168.
- Lei, Z.X., Liew, K.M. and Yu, J.L., 2013. Free vibration analysis of functionally graded carbon nanotube-reinforced composite plates using the element-free kp-Ritz method in thermal environment. *Composite Structures*, 106, pp.128-138.
- Lei, Z.X., Zhang, L.W., Liew, K.M. and Yu, J.L., 2014. Dynamic stability analysis of carbon nanotube-reinforced functionally graded cylindrical panels using the element-free kp-Ritz method. *Composite Structures*, 113, pp.328-338.
- Le-Manh, T. and Lee, J., 2014. Postbuckling of laminated composite plates using NURBS-based isogeometric analysis. *Composite Structures*, 109, pp.286-293.
- Li, Q., Tian, W., Wu, D. and Gao, W., 2023. Nonlinear dynamic stability analysis of imperfect architected cellular sandwich plate under impact loading. *Acta Mechanica Sinica*, 39(4), p.722333.
- Liu, D. and Li, X., 1996. An overall view of laminate theories based on displacement hypothesis. *Journal of composite materials*, 30(14), pp.1539-1561.
- Love, A.E.H., 1888. XVI. The small free vibrations and deformation of a thin elastic shell. *Philosophical Transactions of the Royal Society of London. (A.)*, (179), pp.491-546.
- Magnucka-Blandzi, E. and Magnucki, K., 2007. Effective design of a sandwich beam with a metal foam core. *Thin-Walled Structures*, 45(4), pp.432-438.
- Malekzadeh, P. and Shojaee, M., 2013. Buckling analysis of quadrilateral laminated plates with carbon nanotubes reinforced composite layers. *Thin-Walled Structures*, 71, pp.108-118.
- Matsunaga, H., 2005. Thermal buckling of cross-ply laminated composite and sandwich plates according to a global higher-order deformation theory. *Composite Structures*, 68(4), pp.439-454.
- Mirzaei, M. and Kiani, Y., 2017. Nonlinear free vibration of FG-CNT reinforced composite plates. *Struct. Eng. Mech*, 64(3), pp.381-390.

- MNA, G.T., Chakrabarti, A. and Prakash, V., 2014. Vibration characteristics of functionally graded material skew plate in thermal environment. *International Journal of Mechanical and Mechatronics Engineering*, 8(1), pp.142-153.
- Mohammadi, H., Weeger, O. and Shojaee, M., 2022. Isogeometric technique for dynamic instability analysis of nanocomposite folded plates based on higher-order shear deformation theory. *Thin-Walled Structures*, 177, p.109467.
- Moslemi, A., Neya, B.N. and Amiri, J.V., 2017. Benchmark solution for buckling of thick rectangular transversely isotropic plates under biaxial load. *International Journal of Mechanical Sciences*, 131, pp.356-367.
- Naderi, A. and Saidi, A.R., 2013. An accurate approach for finding the critical buckling stress of thick orthotropic plates. *Composite Structures*, 96, pp.411-418.
- Natarajan, S., Haboussi, M. and Manickam, G., 2014. Application of higher-order structural theory to bending and free vibration analysis of sandwich plates with CNT reinforced composite facesheets. *Composite Structures*, 113, pp.197-207.
- Nguyen, H. and Ostiguy, G.L., 1989. Effect of boundary conditions on the dynamic instability and non-linear response of rectangular plates, Part I: Theory. *Journal of sound and vibration*, 133(3), pp.381-400.
- Nguyen, H., Ostiguy, G.L. and Samson, L.P., 1989. Effect of boundary conditions on the dynamic instability and non-linear response of rectangular plates, Part II: Experiment. *Journal of sound and vibration*, 133(3), pp.401-422.
- Nguyen, Q.H., Nguyen, L.B., Nguyen, H.B. and Nguyen-Xuan, H., 2020. A three-variable high order shear deformation theory for isogeometric free vibration, buckling and instability analysis of FG porous plates reinforced by graphene platelets. *Composite Structures*, 245, p.112321.
- Nguyen-Xuan, H., Tran, L.V., Thai, C.H., Kulasegaram, S. and Bordas, S.P.A., 2014. Isogeometric analysis of functionally graded plates using a refined plate theory. *Composites Part B: Engineering*, 64, pp.222-234.
- Nielsen, P.N., Gersborg, A.R., Gravesen, J. and Pedersen, N.L., 2011. Discretizations in isogeometric analysis of Navier–Stokes flow. *Computer methods in applied mechanics and engineering*, 200(45-46), pp.3242-3253.

- Ovesy, H.R., Taghizadeh, M. and Kharazi, M., 2012. Post-buckling analysis of composite plates containing embedded delaminations with arbitrary shape by using higher order shear deformation theory. *Composite Structures*, 94(3), pp.1243-1249.
- Parida, S. and Mohanty, S.C., 2018. Free vibration analysis of functionally graded skew plate in thermal environment using higher order theory. *International Journal of Applied Mechanics*, 10(01), p.1850007.
- Phung-Van, P., Abdel-Wahab, M., Liew, K.M., Bordas, S.P.A. and Nguyen-Xuan, H., 2015. Isogeometric analysis of functionally graded carbon nanotube-reinforced composite plates using higher-order shear deformation theory. *Composite structures*, 123, pp.137-149.
- Piegl, L. and Tiller, W., 2012. *The NURBS book*. Springer Science & Business Media.
- Praciano, J.S.C., Barros, P.S.B., Barroso, E.S., Junior, E.P., de Holanda, Á.S. and Junior, J.B.M.S., 2019. An isogeometric formulation for stability analysis of laminated plates and shallow shells. *Thin-Walled Structures*, 143, p.106224.
- Prakash, T., Singha, M.K. and Ganapathi, M., 2008. Thermal postbuckling analysis of FGM skew plates. *Engineering Structures*, 30(1), pp.22-32.
- Rafiee, M., He, X.Q. and Liew, K.M., 2014. Non-linear dynamic stability of piezoelectric functionally graded carbon nanotube-reinforced composite plates with initial geometric imperfection. *International Journal of Non-Linear Mechanics*, 59, pp.37-51.
- Ramm, E., 1981. Strategies for tracing the nonlinear response near limit points. In *Nonlinear Finite Element Analysis in Structural Mechanics: Proceedings of the Europe-US Workshop Ruhr-Universität Bochum, Germany, July 28–31, 1980* (pp. 63-89). Springer Berlin Heidelberg.
- Reddy, J.N. and Arciniega, R.A., 2004. Shear deformation plate and shell theories: from Stavsky to present. *Mechanics of Advanced Materials and Structures*, 11(6), pp.535-582.
- Reddy, J.N. and Robbins Jr, D.H., 1994. Theories and computational models for composite laminates.
- Reddy, J.N., 1984. A simple higher-order theory for laminated composite plates.
- Reddy, J.N., 1987. A generalization of two-dimensional theories of laminated composite plates. *Communications in applied numerical methods*, 3(3), pp.173-180.

- Reisenfeld, R. (1975). Xerox University Microfilms. *Child Psychiatry Quarterly*, 1–70.
- Riks, E., 1979. An incremental approach to the solution of snapping and buckling problems. *International journal of solids and structures*, 15(7), pp.529-551.
- Rouhi, S. and Ansari, R., 2012. Atomistic finite element model for axial buckling and vibration analysis of single-layered graphene sheets. *Physica E: Low-dimensional Systems and Nanostructures*, 44(4), pp.764-772.
- Sabir, A.B. and Lock, A., 1972. A curved, cylindrical shell, finite element. *International Journal of Mechanical Sciences*, 14(2), pp.125-135.
- Sahoo, R. and Singh, B.N., 2018. Assessment of dynamic instability of laminated composite-sandwich plates. *Aerospace Science and Technology*, 81, pp.41-52.
- Sankar, A., Natarajan, S. and Ganapathi, M., 2016. Dynamic instability analysis of sandwich plates with CNT reinforced facesheets. *Composite Structures*, 146, pp.187-200.
- Shafei, E., Faroughi, S. and Rabczuk, T., 2019. Isogeometric HSDT approach for dynamic stability analysis of general anisotropic composite plates. *Composite Structures*, 220, pp.926-939.
- Shariyat, M., 2007. Thermal buckling analysis of rectangular composite plates with temperature-dependent properties based on a layerwise theory. *Thin-Walled Structures*, 45(4), pp.439-452.
- Shen, H.S. and Zhang, C.L., 2010. Thermal buckling and postbuckling behavior of functionally graded carbon nanotube-reinforced composite plates. *Materials & Design*, 31(7), pp.3403-3411.
- Shen, H.S., 2011. Postbuckling of nanotube-reinforced composite cylindrical shells in thermal environments, Part I: Axially loaded shells. *Composite Structures*, 93(8), pp.2096-2108.
- Sherbourne, A.N. and Pandey, M.D., 1991. Differential quadrature method in the buckling analysis of beams and composite plates. *Computers & Structures*, 40(4), pp.903-913.
- Shi, Y., Lee, R.Y. and Mei, C., 1997. Finite element method for nonlinear free vibrations of composite plates. *AIAA journal*, 35(1), pp.159-166.

- Shukla, K.K. and Nath, Y., 2001. Analytical solution for buckling and post-buckling of angle-ply laminated plates under thermomechanical loading. *International journal of non-linear mechanics*, 36(7), pp.1097-1108.
- Singh, D.B. and Singh, B.N., 2016. Buckling analysis of three dimensional braided composite plates under uniaxial loading using Inverse Hyperbolic Shear Deformation Theory. *Composite Structures*, 157, pp.360-365.
- Singh, V., Kumar, R. and Patel, S.N., 2021. Non-linear vibration and instability of multi-phase composite plate subjected to non-uniform in-plane parametric excitation: Semi-analytical investigation. *Thin-Walled Structures*, 162, p.107556.
- Singha, M.K. and Daripa, R., 2009. Nonlinear vibration and dynamic stability analysis of composite plates. *Journal of Sound and Vibration*, 328(4-5), pp.541-554.
- Sreehari, V.M. and Maiti, D.K., 2016, May. Buckling and post buckling characteristics of laminated composite plates with damage under thermo-mechanical loading. In *Structures* (Vol. 6, pp. 9-19). Elsevier.
- Styles, M., Compston, P. and Kalyanasundaram, S., 2007. The effect of core thickness on the flexural behaviour of aluminium foam sandwich structures. *Composite Structures*, 80(4), pp.532-538.
- Thang, P.T., Nguyen, T.T. and Lee, J., 2017. A new approach for nonlinear buckling analysis of imperfect functionally graded carbon nanotube-reinforced composite plates. *Composites Part B: Engineering*, 127, pp.166-174.
- Thang, P.T., Nguyen-Thoi, T., Lee, D., Kang, J. and Lee, J., 2018. Elastic buckling and free vibration analyses of porous-cellular plates with uniform and non-uniform porosity distributions. *Aerospace Science and Technology*, 79, pp.278-287.
- Thanh, N.V., Khoa, N.D., Tuan, N.D., Tran, P. and Duc, N.D., 2017. Nonlinear dynamic response and vibration of functionally graded carbon nanotube-reinforced composite (FG-CNTRC) shear deformable plates with temperature-dependent material properties and surrounded on elastic foundations. *Journal of Thermal Stresses*, 40(10), pp.1254-1274.
- Thankam, V.S., Singh, G., Rao, G.V. and Rath, A.K., 2003. Thermal post-buckling behaviour of laminated plates using a shear-flexible element based on coupled-displacement field. *Composite Structures*, 59(3), pp.351-359.

- Thuy Anh, V.T., Quang, V.D., Duc, N.D. and Thinh, P.N., 2022. Impact of blast and mechanical loads on the shear deformable stiffened sandwich plate with an auxetic core layer in thermal environment. *Journal of Sandwich Structures & Materials*, 24(1), pp.663-695.
- Tran, L.V., Phung-Van, P., Lee, J., Wahab, M.A. and Nguyen-Xuan, H.J.C.S., 2016. Isogeometric analysis for nonlinear thermomechanical stability of functionally graded plates. *Composite Structures*, 140, pp.655-667.
- Ullah, S., Zhong, Y. and Zhang, J., 2019. Analytical buckling solutions of rectangular thin plates by straightforward generalized integral transform method. *International Journal of Mechanical Sciences*, 152, pp.535-544.
- Ungbhakorn, V. and Singhatanadgid, P., 2006. Buckling analysis of symmetrically laminated composite plates by the extended Kantorovich method. *Composite structures*, 73(1), pp.120-128.
- Upadhyay, A.K. and Shukla, K.K., 2013. Post-buckling behavior of composite and sandwich skew plates. *International Journal of Non-Linear Mechanics*, 55, pp.120-127.
- Van Do, V.N. and Lee, C.H., 2019. Quasi-3D isogeometric buckling analysis method for advanced composite plates in thermal environments. *Aerospace Science and Technology*, 92, pp.34-54.
- Van Do, V.N. and Lee, C.H., 2021. Isogeometric analysis for buckling and postbuckling of graphene platelet reinforced composite plates in thermal environments. *Engineering Structures*, 244, p.112746.
- Wall, W.A., Frenzel, M.A. and Cyron, C., 2008. Isogeometric structural shape optimization. *Computer methods in applied mechanics and engineering*, 197(33-40), pp.2976-2988.
- Wang, C., Wu, M.C., Xu, F., Hsu, M.C. and Bazilevs, Y., 2017. Modeling of a hydraulic arresting gear using fluid–structure interaction and isogeometric analysis. *Computers & Fluids*, 142, pp.3-14.
- Wang, C.M., Reddy, J.N. and Lee, K.H., 2000. Relationships with Classical Solutions.
- Wang, X. and Yuan, Z., 2018. Buckling analysis of isotropic skew plates under general in-plane loads by the modified differential quadrature method. *Applied Mathematical Modelling*, 56, pp.83-95.

- Wang, X., Tan, M. and Zhou, Y., 2003. Buckling analyses of anisotropic plates and isotropic skew plates by the new version differential quadrature method. *Thin-Walled Structures*, 41(1), pp.15-29.
- Wang, Z.X. and Shen, H.S., 2012. Nonlinear vibration and bending of sandwich plates with nanotube-reinforced composite face sheets. *Composites Part B: Engineering*, 43(2), pp.411-421.
- Watts, G., Singh, S. and Pathan, F., 2020. Meshfree analysis of non-rectangular sandwich plates based on refined C0 higher order shear deformation theories. *Engineering Analysis with Boundary Elements*, 120, pp.180-194.
- Wu, H., Yang, J. and Kitipornchai, S., 2017. Dynamic instability of functionally graded multilayer graphene nanocomposite beams in thermal environment. *Composite Structures*, 162, pp.244-254.
- Wu, T.L., Shukla, K.K. and Huang, J.H., 2007. Post-buckling analysis of functionally graded rectangular plates. *Composite structures*, 81(1), pp.1-10.
- Wu, W.X., Shu, C., Wang, C.M. and Xiang, Y., 2010. Free vibration and buckling analysis of highly skewed plates by least squares-based finite difference method. *International Journal of Structural Stability and Dynamics*, 10(02), pp.225-252.
- Yang, H.S., Dong, C.Y. and Wu, Y.H., 2020. Postbuckling analysis of multi-directional perforated FGM plates using NURBS-based IGA and FCM. *Applied Mathematical Modelling*, 84, pp.466-500.
- Yang, J., Huang, X.H. and Shen, H.S., 2020. Nonlinear vibration of temperature-dependent FG-CNTRC laminated plates with negative Poisson's ratio. *Thin-Walled Structures*, 148, p.106514.
- Yu, T., Yin, S., Bui, T.Q., Xia, S., Tanaka, S. and Hirose, S., 2016. NURBS-based isogeometric analysis of buckling and free vibration problems for laminated composites plates with complicated cutouts using a new simple FSDT theory and level set method. *Thin-Walled Structures*, 101, pp.141-156.
- Zghal, S., Frikha, A. and Dammak, F., 2018. Mechanical buckling analysis of functionally graded power-based and carbon nanotubes-reinforced composite plates and curved panels. *Composites Part B: Engineering*, 150, pp.165-183.

Zhang, L.W., Ardestani, M.M. and Liew, K.M., 2017. Isogeometric approach for buckling analysis of CNT-reinforced composite skew plates under optimal CNT-orientation. *Composite Structures*, 163, pp.365-384.

Zhang, Y.X. and Yang, C.H., 2009. Recent developments in finite element analysis for laminated composite plates. *Composite structures*, 88(1), pp.147-157.

Zhu, P., Lei, Z.X. and Liew, K.M., 2012. Static and free vibration analyses of carbon nanotube-reinforced composite plates using finite element method with first order shear deformation plate theory. *Composite Structures*, 94(4), pp.1450-1460.

Publications from Present Work

Journal Publications

1. Sengar, V., Nynaru, M., Watts, G., Kumar, R. and Singh, S., 2023. Postbuckled vibration behaviour of skew sandwich plates with metal foam core under arbitrary edge compressive loads using isogeometric approach. *Thin-Walled Structures*, 184, p.110524.
2. Sengar, V., Watts, G., Kumar, R., Patel, S.N. and Kumar, A., 2024. Tunable thermal postbuckling response of imperfect skew sandwich plates with auxetic core and FGCNTRC facings using isogeometric approach. *Engineering Structures*, 305, p.117706.
3. Watts, G., Kumar, R., Singh, S., Sengar, V., Reddy, G.R. and Patel, S.N., 2022. Postbuckling and postbuckled vibration behaviour of imperfect trapezoidal sandwich plates with FG-CNTRC face sheets under nonuniform loadings. *Aerospace Science and Technology*, 127, p.107716.
4. Sengar, V., Watts, G., Kumar, R., & Patel, S. N. Non-linear Vibration behaviour of skew sandwich plates with auxetic core and FGCNTRC facings using isogeometric approach. *(Under Preparation)*

Conference Proceedings

1. Sengar, V., Watts, G. (2022). Isogeometric analysis of functionally graded carbon nanotube-reinforced imperfect trapezoidal sandwich plates under non-uniform edge compression. International Conference on Advances in Mechanics, Modelling, Computing and Statistics (ICAMMCS), BITS Pilani, Pilani Campus, 19-21 March, 2022.
2. Watts, G., Kumar R., Sengar, V. (2022). Post buckling and post buckled vibration behaviour of imperfect trapezoidal sandwich plates under non-uniform edge compression. 11th European Solid Mechanics Conference (ESMC), NUI Galway, Ireland, 4-8 July 2022.
3. Sengar, V., Watts, G. (2022). Isogeometric HSDT approach for vibration behaviour of laminated composite plates in thermal environment. 8th International Congress on Computational Mechanics and Simulation (ICCMS), IIT Indore, 9 -11 December 2022.

4. Sengar, V., Watts, G. (2022). Isogeometric thermal buckling analysis of laminated skew plates. 8th Asian Conference on Mechanics of Functional Materials and Structures (ACMFMS), IIT Guwahati, 11 -14 December 2022.
5. Sengar, V., Watts, G. (2023). Non-linear stability behaviour of initially imperfect sandwich plates with auxetic core in thermal environment using Isogeometric approach.3rd International Conference on Recent Advances in Materials & Manufacturing Technologies (IMMT) BITS Pilani, Dubai Campus,20-23 November 2023.
6. Sengar, V., Watts, G.& Utham V A (2023). Thermal vibration characteristics of functionally graded carbon nanotube reinforced sandwich plate with auxetic core using isogeometric analysis approach. CDPMHM 2024, IIT Mandi , 20 -21 June 2024.
7. Utham V A, Watts, G. Mishra R. R.& Sengar, V. (2023). Blast response of sandwich panel with re-entrant auxetic core. CDPMHM 2024, IIT Mandi , 20 -21 June 2024.



Dr. Gaurav Watts is an experienced professional in the field of computational mechanics, boasting over a decade of expertise. He earned his PhD in Computational Mechanics from the prestigious Indian Institute of Technology Delhi and currently serves as an Assistant Professor in the Mechanical Engineering Department at BITS Pilani, Pilani campus, Rajasthan, India. Dr. Watts is particularly interested in Computational Mechanics, Composite Structures, Meshfree methods, Isogeometric analysis (IGA), Finite Element Methods, and Fluid-Structure Interaction. His team is currently focused on the Isogeometric analysis of sandwich structures and blast response of sandwich structures, among other exciting projects. Dr. Watts has a wealth of publications in renowned international peer-reviewed journals with global publishers such as ASME, ASCE, Elsevier, Springer, and Taylors & Francis. He is actively involved in sponsored research projects from government funding agencies and industries. Dr. Watts is also a passionate educator who embraces new teaching methodologies, inspiring and motivating his students to meet the challenges of the modern era.



Mr Vasudev Sengar is a resident of Jhansi, Uttar Pradesh, India. He completed B.E honours in Mechanical Engineering from the Institute of Information Technology and Management Gwalior, affiliated with RGPV Bhopal, Madhya Pradesh, India 2010. From 2011 to 2012, he worked as an assistant professor at ITM Group Gwalior, and from 2012 to 2013, he was an engineer trainee at KIEL Group Gwalior. In 2015, Mr. Sengar completed his Master of Technology (M.Tech.) in Mechanical Engineering from the National Institute of Technology, Rourkela, Odisha, India. From 2016 to 2017, he served as an assistant professor at GL Bajaj Group Mathura and later at IPSCTM Gwalior until August 2019. In August 2019, Mr. Sengar enrolled for his doctoral studies (Ph.D.) in the Department of Mechanical Engineering, BITS Pilani, Pilani Campus, Rajasthan, India, under the supervision of Dr. Gaurav Watts, Assistant Professor at BITS Pilani.